Title
Microclimates mediate water fluxes from vegetation

Permalink
https://escholarship.org/uc/item/7tb5t12f

Author
Bilir, Teresa Eren

Publication Date
2022

Microclimates mediate water fluxes from vegetation

by

Teresa Eren Bilir

A dissertation submitted in partial satisfaction of the

requirements for the degree of

Doctor of Philosophy

in

Environmental Science, Policy, and Management

in the

Graduate Division

of the

University of California, Berkeley

Committee in charge:

Professor Inez Fung, Chair
Professor Todd Dawson
Professor John Chiang
Dr. Charlie Koven

Summer 2022

Microclimates mediate water fluxes from vegetation

Abstract

Microclimates mediate water fluxes from vegetation

by

Teresa Eren Bilir

Doctor of Philosophy in Environmental Science, Policy, and Management

University of California, Berkeley

Professor Inez Fung, Chair

Earth is the blue planet, unique in our solar system for its ability to sustain a water cycle that spans three phases: solid (ice), liquid (water), and gas (water vapor). The global cycling of water between the earth's land surface, subsurface, cryosphere, oceans, and atmosphere is fundamental to earth's radiative balance and energy transport, and sustaining life in every ecosystem. The global water cycle is also a driver of feedbacks between the land surface and the atmosphere over a range of scales, from minute exchanges through stomata on leaves to eco-climate teleconnections wherein continental-scale changes in vegetation cover could alter climate and ecosystem dynamics in a different hemisphere.

At fine spatial scales, microclimatic variation influences the strength and type of these feedbacks, and plays a role in determining patterns of vegetation vulnerability. Microclimates arise in hilly terrains from the midlatitudes to the poles due to differences in solar gain on opposing slopes. This leads to differences in the daily timing, duration, and intensity of sunlight exposure, and variable associations between sunlight and other climatic variables such as air temperature and humidity. These slope-aspect-induced climate differences are ecologically important, and impact vegetation-mediated water balance between the earth surface and the atmosphere.

This thesis investigates climate–vegetation feedbacks arising from the impact of microclimate variation on water fluxes from forest vegetation. The primary investigation approach was a field study based at the University of California's Angelo Coast Range Reserve in Northern California. There, I installed sensors to collect continuous high-resolution ($\sim$ 5 minutes) data in a study of water flux differences in Pacific madrone (*Arbutus menziesii*) and Douglas fir (*Pseudotsuga menziesii*) across a slope-induced microclimatic gradient from spring 2018 to fall 2020. The field site has a Mediterranean climate with wet winters and dry summers.

Chapters 2, 3, 4, and 5 present our instrumentation and field installation, our data on sap velocity from 14 Pacific madrone and 6 Douglas fir trees spanning adjacent north and south slopes at the Reserve, as well as our analysis of sap velocity variations in the context of high-resolution *in situ* observations of air temperature, relative humidity, soil moisture, and insolation. The environmental observations highlight climatic gradients on small scales, showing neighboring wet and dry zones in the soil, and seasonally evolving sub-canopy gradients in air temperature and humidity (chapter 2). A cross-species comparison of transpiration between Pacific madrone and Douglas fir trees demonstrates the impact of being tall: despite operating with slower peak sap velocities over the dry season, Douglas firs consistently transpired as much or more than their Pacific madrone neighbors, thanks to a longer exposure to sunlight granted by their height (chapter 3). A cross-slope comparison of transpiration in a single species (Pacific madrone) yielded a surprise: integrated summer transpiration is higher on the drier south slope than the north slope, which has abundant rock moisture but less sunlight (chapter 4). Analysis of the Pacific madrone sap flow data from both slopes in an environmental response model emphasizes the difference between tree populations on each slope in their aggregate physiological responses to specific aspects of their environments (chapter 5).

Analysis of my field data suggests that the tree populations on each slope acclimate to their respective microclimates in functionally relevant ways. In particular, we hypothesize that south slope trees use water more sparingly under water-limited conditions, and yet still transpire more water over their longer and sunnier days. We speculate that differing proportions of sun-adapted and shade-adapted leaves, differences in stomatal regulation, and cross-slope root-zone moisture differences could explain some of the observed and modeled differences. Yet, the analysis of chapter 5 does not identify mechanisms of acclimation with the observations available. To explore these and other hypotheses, in the final chapter we turn to the rich parameter space of a model with high process resolution, CLM-FATES, a component of an Earth System Model (6). Though this aspect of the work is ongoing, we demonstrate that, in a model forest of broadleaf evergreen trees, differences in light availability alone are not sufficient to explain the cross-slope transpiration differences observed in the field. We also show that, because different stand structures have different physical properties, substantive plasticity in light- and water-use efficiency can evolve even while holding plant functional traits constant.

This thesis advances our understanding of how water cycling by trees varies with local environment and climate. It contributes to improved representation of the complex Earth system in climate models by adding to current understanding of the processes that affect the cycling of water. The results open new research avenues in representing vegetation function in land surface models, especially in rough, hilly or mountainous terrains which are characterized by a mosaic of highly variable microclimates. This representation will, in turn, be a useful tool to anticipate tree mortality, species shifts, or even extinctions, and to guide climate mitigation strategies involving ecosystems.

I dedicate this thesis to the memory of my mother, Patricia (1949–2015), my first mentor in scientific inquiry and persistence, who would have enjoyed hearing about trees; and to my two new little scientists, exemplars of curiosity.

Contents

Acknowledgments

The challenge of writing acknowledgments is that the list of people to thank is far greater than can ever be put onto a page. “It takes a village to raise a PhD”, they say, or perhaps it would be more apt for a student working out of a research site called Rivendell to adapt the popular meme, “One does not simply … finish a PhD”. Perhaps true for all PhD candidates, it’s especially true for students who, like me, experienced the joy of a growing family along the way. This brief acknowledgement only hints at the tip of what is an extremely large iceberg. Village. Icebergvillage. Unmix my metaphors in your own head, please.

My family saw me through years of remote field work, a global pandemic, and two new children to the finish line. I thank my father, brothers and sisters for being sources of advice about all the basic life skills, for an endless supply of hand-delivered banana bread and every item I could possibly need for the kids, and for always being willing to try my latest food experiment. I thank my in-laws for their generous support and care of our family, up to and including being work-from-home partners when I needed to get out of the house to concentrate. I particularly thank my husband Andrew for being present, listening, and excited about every step of my research. Whether as a patient ear for me to try new explanations on, a partner in hobbies, incredible dad, or an early-morning source of really, truly bad puns, Andrew’s support has taken innumerable forms, each more important and life-giving than I can put into words.

I am inexpressibly grateful to my advisor, Inez Fung, for her creativity, kindness, and optimism, and being an all-around inspiration. I deeply appreciated Inez’s generosity and skill in reframing challenges as opportunities, sharing her own stories, and being an accessible and perceptive source of guidance. I thank Inez for suggesting these research directions, coaching me in how to approach a problem one step at a time, getting me unstuck, and the many other conversations. I also thank Jim Bishop for introducing me to Inez as an undergraduate. Without Jim propelling me into her office and telling me repeatedly that it was okay, I would never have approached Inez for a research position. Thank you both for being so conscious and encouraging of the young

people in your midst, in every way, up to and including letting me practice sap flow installations on your backyard trees.

Others whose spirit for fostering young folks was transformative for me were those at Carnegie Institution's Department of Global Ecology, where I worked before my graduate studies. I'm grateful to that community for preparing me for, and launching me into, graduate school. Katie Mach poured immense energy and kindness into mentoring me while I was with the IPCC's technical support unit, pushing me to acknowledge my contributions. Chris Field constantly thought up new exciting jobs for me, and was invariably a better judge of what I could do than I was myself. Thank you to everyone at DGE for teaching me, building me up and believing in me, and inviting me to play music at your events.

During my time as a graduate student, I've been supported by several incredible research groups, both at Berkeley and beyond. Those who overlapped with me in 301 McCone— Hannah Bourne, Octavia Crompton, Jesse Day, Jiabin Liu (along with Boba), Xiaojuan Liu, Holly Maness, Alex Turner, Michail Vrettas, and Stephanie Wuerth— shaped my research ideas and energized me. Thank you for being classmates, coding coaches, statistics teachers, coffee and lunch buddies, putting up with that mountain of field-work gear that accumulated behind my desk, and once or twice even giving up a day of your time to keep me company in the field. The members of the climate reading group, including members of the Chiang and Boos research groups, taught me about their areas of research, asked the most intriguing questions of our visiting guests, and provided invaluable engagement on my own work. I particularly thank Michael Diaz for joining me on a crack-of-dawn trip to the field, where he cheerfully laughed off being narrowly missed by a falling tree; Michael Herman for loaning me tools from his own collection to experiment with; and Wenwen Kong and Marysa Laguë for their encouraging conversations and proposal advice.

This work and the collaborations therein were made possible through generous funding from multiple sources. I thank the NSF for funding the Eel River Critical Zone Observatory (EAR-1331940), Carol Baird for supporting field research at UC Natural Reserves, the DOE Office of Science for providing grants DE-SC0010857, DE-SC0014080, and an DOE Office of Science Graduate Student Research Fellowship; Berkeley's ESPM department for multiple fellowships; Berkeley's Graduate Division for generous financial aid to support student parents; and both ESPM and EPS for providing the teaching positions that kept me funded in my latter years. I have also been tremendously lucky to have the support of Fung group lab manager David Elvins, who helped me tackle proposals, coding, and tricky funding questions. At the CZO, Sarah Baker provided tireless logistical support to keep me funded and support my trips to the field. In the ESPM department, I am deeply indebted department GSAO Ryann Madden for going far above and beyond in crafting creative solutions for employment and funding while accommodating my needs as a student parent.

I am grateful for the nationwide collaborations that led to the Critical Zone Observatory network, and to the Keck Hydrowatch project for establishing the research site at which I worked. It was a pleasure to study this intersection of earth system processes in a hands-on environment at the Eel River Critical Zone Observatory– to see the soil, rocks, roots, leaves, rivers, and animals with my own eyes– while listening to the research of a broad spectrum of experts. I particularly thank Todd Dawson, Bill Dietrich, Daniella Rempe, and Collin Bode for their help and encouragement along the way, and undergraduate researchers Katelyn Yu, Cecily Tye, and Lian Zhang for being incredible field work helpers. It was an absolute privilege to work as a member of a broader community of Eel River CZO students and postdocs, and together share ideas, long car rides, meals and delicious cake.

Outside of UC Berkeley, I thank LBNL researchers Charlie Koven, Gregory Lemieux, Junyan Ding, and the other members of the international FATES research group for making me feel welcomed in a brand new research space in the midst of a pandemic, for their patience and support in helping me get oriented— and stay oriented despite the birth of two kids— and for helping me develop new research directions. For refinement of my research ideas, I thank Carnegie and Stanford researchers Jen Johnson, Joe Berry, and Hal Mooney. To Jen I am also indebted for many enriching conversations, a wealth of literature recommendations, new research ideas, career advice, and expert instruction in gas exchange and other leaf-level measurements. Thank you for sharing that with me!

I also thank my friends for their multi-faceted support and care during these past 7 years. No matter how long I've had my head under this PhD / pandemic

/ small children-induced rock, you've always made it easy to begin where we left off. I thank Elan Dagenais for her collaboration on sundry music endeavors, advice on completing one's dissertation, the bottomless supply of good humor and parenting anecdotes, and for being a text away at literally. every. minute. of the day. I thank Melisa Lin for making my PhD years brighter and yummier with fresh flowers and home cooked food, more entertaining with her dry wit, and more relaxing by providing safe haven on her peaceful farm where you can overcome any kind of angst by digging up a flower bed.

Finally, I also thank my mother, to whom this dissertation is dedicated, for a lifetime's example of being an engaged member of her community and using one's talents to the fullest extent possible. Though she passed away suddenly just before I began my graduate studies, I know she would have loved to see where, with the help of everyone here and in the broader icebergvillage, I've arrived.

Chapter 1

Introduction

1.1 Overview

The breathing of the terrestrial biosphere governs the exchange of 50% of global carbon fluxes between the earth's surface and the atmosphere [31], and up to 60% of water fluxes between the land and the atmosphere [80]. Many devastating impacts of climate change, including extreme heat, drought, and systemic ecological change or collapse, are thus inextricably connected to the responses of terrestrial vegetation to their changing environments — and in particular, to the sensitivities and responses of forest ecosystems. Anticipating these impacts hinges on understanding processes on the scale that governs the life and death of individual trees.

Using observations of water use in individual trees in a detailed ecological context, this thesis explores the sensitivity of tree water use to variable climatic conditions. The major finding is that topographically mediated microclimates generated by solar radiation differences lead to a detectable degree of biological acclimation in tree water use, even within a single species. This thesis also contributes findings related to species differences in water flux seasonality and quantity, and makes methodological contributions in instrument deployment and data analysis. It concludes with a description of ongoing work that aims to connect the observed biological acclimation in individual trees with representations of vegetation in a detailed ecosystem demography model.

This thesis is organized into six chapters: 1) An introduction; 2) A description of instruments, installation procedures and experiment design for an observational campaign at the Angelo Coast Range Reserve; 3) Exploratory data analyses; 4) Analysis of the resulting field data centered on characterizing water fluxes; 5) Analysis of the resulting field data centered on characterizing biological acclimation to microclimates; and 6) A description of follow-up experiments in a state-of-the-art vegetation demography module of an Earth System Model.

1.2 Forest water fluxes

1.2.1 Forests water fluxes: the dial on a regional thermostat

The water cycle is a key point of connection between forests and local climate. Recent work at a research site in the Mediterranean climate of Northern California Coast Range has shown that the seasonality of transpiration varies markedly by species in a mixed broadleaf/needleleaf evergreen forest, with Douglas fir trees (*Pseudotsuga menziesii*) having maximal transpiration in the wet season (winter-spring), and Pacific madrone trees (*Arbutus menziesii*) having maximal transpiration in the dry season (summer-early fall) [55]. This suggests that the timing and amount of water flux from the land to the atmosphere is sensitive to shifts in species composition within forests.

Because the Mediterranean atmosphere of this region in northern California is dry over the summertime, changing the seasonality of vegetation water fluxes changes summertime humidity in the atmosphere, and hence surface temperatures. Thus, the species composition of this forest determines when the surrounding region experiences a cooling ‘air conditioning’ effect via vegetation water fluxes into a dry atmosphere, which in turn change the regional balance of latent and sensible heat. Shifts in species, and thus the seasonality of peak ‘air conditioning’, determines whether extremes of high temperature and low humidity may be ameliorated or exacerbated relative to historical norms. An analysis using the Weather Research and Forecasting model found that the potential impact could be as large as 2.5°C in the hottest months of the year, based on the magnitude of this observed transpiration timing offset [56]. This is an impact on par with the expected magnitude of average regional warming stemming from global anthropogenic climate change [77].

1.2.2 Forest water flux interactions with climate change

In combination with other human pressures on forests, anthropogenic climate change is altering the physical climates hosting forest ecosystems globally at a rate which is unprecedented. This is impacting the extent, species composition, and structures of these ecosystems [67]. Because forests themselves interact with climate physically and biogeochemically [20, 73], changes in forest ecosystems also influence local and regional climates, affecting living conditions for vast numbers of people. Understanding the capacity of trees to acclimate to different climates, and hence anticipating how forest ecosystems will function under a changing climate, will enable decision-makers to make informed investments in future resilience.

The term ‘acclimation’ is used throughout this thesis to denote slow vegetation responses that have the potential to change the parameters of plant functional processes that act on faster time scales. Multiple changes to vegetation function are expected in the future, although the mechanisms and degrees of change are still under investigation. Still, there is evidence that changes in forests on long time scales in response to changes in physical climate will be substantive. Short-term vegetation responses to individual physical climate changes are well-studied, while longer-term responses, and interactions among responses, are uncertain. In all cases, the vegetation responses anticipated have direct bearing on vegetation water fluxes. For example, some areas of anticipated physical changes and vegetation responses are outlined below:

CO_2: Atmospheric CO_2 concentrations are rising globally [46, 37]. Changes to stomatal regulation are observed in the presence of elevated CO_2 levels (a phenomenon termed ‘CO_2 fertilization’), leading to an increase in water-use efficiency (WUE) [18]. Changes to trace nutrient (e.g., nitrogen or phosphorus) use and allocation in plant tissues have also been noted [1], as well as increases in overall carbon fixation (i.e., increasing plant growth). Trace nutrient use has downstream bearing on WUE as well [29]. In aggregate, these responses to CO_2 fertilization show competing impacts: Increases in WUE may decrease amount of water transpired, while increases in plant biomass may increase amount of water transpired by increasing the amount of transpiring leaf surface. How these and other factors will balance over longer timescales in a variety of regional contexts is unknown [54, 18].

Temperature: Temperatures are rising globally [25]. The diverse physiology of plants allows for a range of temperature tolerance, leading to variable impacts depending on species [48]. For plants that are pushed into or out of their optimal temperature ranges, ratios of photosynthesis to respiration will change, changing WUE as well.

Water: Depending on the region, changes in water availability may include trending wetter or dryer, alongside more- or less-extreme seasonal differences or year-to-year variability [23]. Studies anticipating the degree to which plants will alter their water use in response to perturbations have largely focused on drought responses and mortality thresholds (e.g., [61]), and show differing responses by species.

Trace nutrients: Global climate changes also impact the biogeochemical cycling of trace nutrients, alongside major impacts to nutrient cycles arising from anthropogenic activity that are regionally specific (e.g., excess meteoric nitrogen deposition from urban smog) [18]. The impact of changes in nutrients depends on the starting point of nutrient limitations in the ecosystem. In general terms, overlooking any accompanying negative impacts of the change (e.g., following from the prior example, acid rain damage to foliage), relaxing nutrient limitations enhances WUE by allowing more flexible biochemical optimizations of leaf enzyme levels (e.g., [16]).

Light: Possible changes to the light environment experienced by forested ecosystems come indirectly through ecosystem changes. For instance, anticipated reductions in biodiversity are expected to substantively change the vertical structure of forest canopies, with concomitant changes to light environments within the canopies [59]. CO_2 fertilization may increase leaf area in some forest ecosystems [54], which would also impact vertical light gradients. Poleward or upslope shifts by species seeking cooler environments to avoiding temperature stress (e.g., [71]) will also come with changes in light environment caused by differences in geometric orientation to the sun between old and new growth sites. Vegetation acclimation to changes in light environment has been observed on multiple time scales, from biochemical changes in leaf enzymes [58] to changes in overall growth habit [84, 47]. All of these changes are relevant to water use amount and WUE. Short-term changes in stomatal regulation (minutes) are modulated over time by changes in enzymes that set the photosynethetic rate (weeks), while longer-term changes in the canopy quantity and distribution of stomata due to changes in sun- and shade-leaf growth (months to seasons), or changes in the length or resistance of hydraulic pathways between soil and atmosphere caused by changes in crown geometry and branching architecture (years), can directly impact the water economy of the plant.

The fact that both fast and slow vegetation responses to these physical changes will impact WUE is key. Accurate representations of ecosystem-scale WUE are necessary for forecasting the impacts of climate change: a recent analysis identified water-use strategy and efficiency, ecosystem productivity, and carbon-use efficiency as three "major axes" of ecosystem function which together capture the range of ecosystem responses to change [65]. Hence, a large degree of changes to ecosystems or land-surface fluxes may exist within the uncertain impacts of long-term plant acclimation.

1.3 Research Contributions

This thesis centers on the challenge of characterizing the degrees and types of vegetation acclimation to inhabited microclimate. We undertook a multi-part investigation that yielded new data and several scientific findings.

1.3.1 New data

The field data were collected at the Angelo Coast Range Reserve as part of the NSF's Eel River Critical Zone Observatory project. A novel feature of this data set is the long duration and high frequency of observations and the large number of trees under observation, which is unusual for a sap flow study. All unprocessed data are available at an online repository (https://dendra.science/). A portion of the data, alongside original scripts for processing and analysis, are also published [7].

1.3.2 Scientific findings

Analysis of the field data led to several major findings:

1) In chapter 4, we show that sap flow measured in Pacific madrone (*Arbutus menziesii*) on two opposing hill slopes with distinct solar environments

document substantive differences in water flux, and that trees on the drier south slope have higher transpiration integrated over the summer.

2) In chapter 5, we show that analysis of these differences with an environmental response model shows evidence for functional acclimation of Pacific madrones to variable climate. The trees on the different slopes have different sensitivities to insolation, soil moisture, and vapor pressure deficit (VPD).

The data additionally confirm several previously-documented findings:

3) In chapter 3, we show that not all evergreen tree species have the same transpiration seasonality: there is an offset of several months in the respective timings of peak sap velocities in Pacific madrone and Douglas fir (*Pseudotsuga menziesii*), as first documented by [56].

4) In chapter 5, we show the hysteresis in relationships between sunlight, VPD, and sap velocity, as previously discussed and documented in [32] and [94].

Our data also showed several features that may be more unique to our site, but are suggestive that similar degrees and scales of variation could exist elsewhere:

5) In chapter 2, we show that sap velocity is non-uniform circumferentially around a tree. This was separately documented in Pacific madrone, Douglas fir, and coast live oak (*Quercus agrifolia*) trees. This has implications for how sap velocity data are interpreted.

6) In chapter 2, we show that Pacific madrone rooting networks do not have the capability of hydraulic redistribution at our observation site, while nearby Douglas fir rooting networks do. Hence, synergy may be present where Pacific madrones and Douglas firs co-exist. In at least one location near a Douglas fir, we observed overnight moisture recharge in shallow soil layers, but have not definitively connected this to sap flows in the Douglas fir roots.

7) In chapter 2, we show that shallow (upper 30 cm) soil moisture varies substantially at a 10 m lateral length scale at this site, while in chapter 3, we show that this variation does not correlate with vegetation distribution or function.

8) In chapter 2, we show that sub-canopy gradients in air temperature and humidity both evolve seasonally due to changing soil temperatures and moisture content, and also react strongly to transient patches of sunlight filtering through the canopy to reach the forest floor.

Chapter 2

Instrumentation, field design, and data processing

2.1 Introduction

My dissertation is focused on variation in sap velocity in different environments. The research was carried out in two phases, as major equipment failed one month after the initial installation. The prohibitive cost to replace the initial type of sap velocity sensor necessitated the purchase of a new type of sap velocity sensor from a different manufacturer, as well as a re-design of the field deployment.

This chapter introduces field design and instruments used in this dissertation work, the research goals and field deployment for each phase, data processing, and preliminary data analyses.

2.2 Instrumentation

This section covers the theory and use of all sensors deployed in this research. We begin by describing two types of sap velocity sensor, including a description of a pilot installation at the University of California Botanical Garden. We conclude by describing the environmental sensors deployed in this research to measure soil moisture, air temperature, and humidity.

2.2.1 Sap velocity measurement theory

Sap velocity, defined as the speed of water moving through the xylem tissues of a plant, can be measured by inducing a heat signal in the stem, measuring changes in the heat signal over time, and analytically backing out a heat advection term attributable to the movement of sap. Sensors consist of a heat source and a temperature monitoring instrument, typically thermocouples. In woody, thick-stemmed plants such as trees, both the heater and temperature monitoring elements of the sensors are inserted into the stem tissue at a depth sufficient to reach past the bark, phloem, and cambium into the xylem, through a combination of carving and drilling.

2.2.1.1 HRM sensors

Heat Ratio Method (HRM) sensors consist of three parallel probes: a heating element in the center, flanked by thermocouples upstream (below) and downstream (above) from the heating element. Figure 2.1 shows the orientation of the probes in an idealized setting.

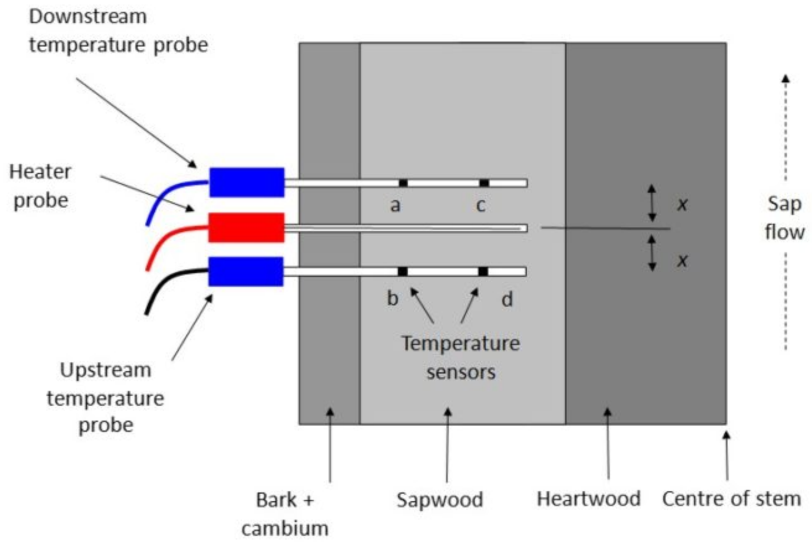

Figure 2.1: A schematic of a heat ratio method sap flow sensor, showing the relative positions of the probes, reproduced from the manual [43].

As derived in [60], the logarithm of the ratio of the temperatures reported by the upper and lower probes (v_1, v_2) is used to track the sap velocity (V), scaled by the ratio of the distance between the heating element and flanking probes (x) and the thermal diffusivity of the living wood (k):

$$V = \frac{k}{x} \times \ln\left(\frac{v_1}{v_2}\right) \tag{2.1}$$

This method of measuring sap velocity requires the assumption that the upper and lower thermocouples are equidistant from the heater, and that thermal properties of the living wood are symmetrical above and below the heater. When these are met, this measurement method has several advantages. Firstly, zero flow conditions are directly measured, rather than computed. Secondly, reverse flow rates can be measured. Thirdly, the thermal properties of wood, which can be a source of uncertainty *in situ*, impact the scale of flow but not the ordinal signal, and most importantly, not the measurement of zero flow conditions [17].

2.2.1.2 TDP sensors

Thermal Diffusivity Probe (TDP) sensors operate on principles similar to HRM sensors: thermocouples monitor changes in an induced heat signal in the plant stem, and back out the sap advection term. Unlike in the HRM, raw data from TDP sensors are reported in the form of temperature differences ($d\mathrm{T}$) between a thermocouple on an upper, heated probe and a lower, unheated probe (see figure 2.2).

At zero flow, the temperature difference between the upper and lower probes is maximized. As flow increases from zero, sap moving across the upper heated probe advects heat away, reducing the temperature difference. Sap velocity u is an exponential function of temperature differences relative to the maximum observed difference:

$$u = aK^b, \tag{2.2}$$

where

$$K = \frac{(d\mathrm{T}_{\mathrm{Max}} - d\mathrm{T})}{d\mathrm{T}} \tag{2.3}$$

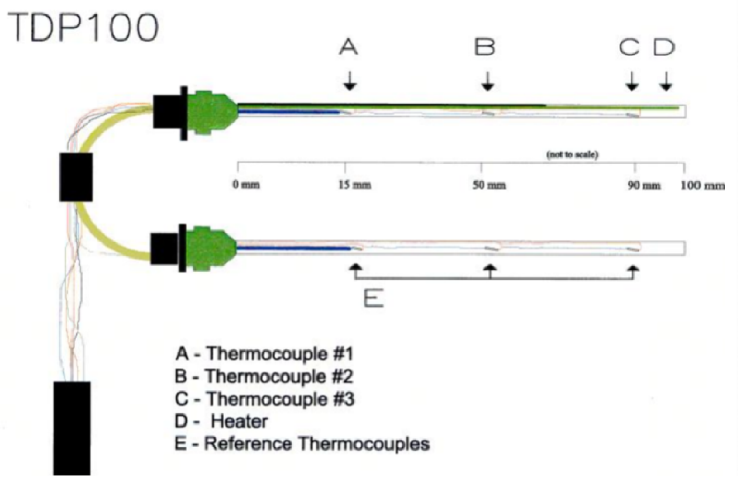

Figure 2.2: A schematic of a 100 mm thermal dissipation probe sap flow sensor, showing the relative positions of the heated and unheated probes, and multiple sensing junctions with depth. Reproduced from the manual [42].

This method requires that the heat field around the heated probe be carefully controlled. Empirical parameters a and b, derived and presented in [34], are suitable for a heat field around the top probe sufficient to create $d\mathrm{T}_{\mathrm{Max}}$ values of approximately 10°C, and the two needles need to be spaced far enough to avoid heat from the heated probe reaching the unheated probe.

2.2.1.3 Challenges and comparison of methodologies

Challenges of working with HRM sensors stem from meeting the physical assumptions of symmetric installation. Installing HRM probes symmetrically around the central heater requires three parallel conduits to be drilled into living wood tissue prior to insertion, which is both difficult to achieve and to immediately verify after drilling. Another geometric hurdle arises from the fact that xylem conduits themselves are rarely precisely parallel to the direction of growth (for example, see figure 2.3). Aligning the probes with the xylem tissue is necessary in order to accurately capture flow rates, but the wood grain is not always visible. For this reason, some varieties of HRM sensors include the use of lateral probes to the left and right of the heater to derive an angle of flow, but then must further contend with the complication that xylem tissue does not diffuse heat isotropically, due to the bunched-straw-like geometry of the wood–water matrix. Before the installation, I carried out several tests to understand some of these challenges.

Figure 2.3: An HRM sensor was installed into a coast live oak tree (*Quercus agrifolia*) at the University of California's Botanical Garden. The thin grey bark sits atop a thick (∼2cm) red layer of phloem (sugar transporting tissues) and cambium (wood growing layer). The lacy tissue beneath the sensor is the last layer of soft tissue before striking hard xylem (a small patch of which is visible below the bottom probe). This layer is preserved to limit evaporative water loss from the installation, and also to guide the probe alignment. It shows a clear diagonal growth orientation, with which the probe set is aligned.

My tests with a plank of milled wood revealed that, while using a power drill to make three holes each 3 cm deep, best efforts to maintain a precise 6 mm spacing between the three holes led to errors of 1-2 mm, even when using the standard drill guide. Better results were achieved using a slow hand-powered drill, with spacing accurate within 0.5 mm. Near-perfect results were achieved without using the drill guide, but instead with a second pair of eyes verifying that that the slow hand-powered drill was going in straight from another angle. In this configuration the drill guide presented a barrier to seeing the exact angle of the drill bit where it met the wood, so was not used. We found these methodological improvements necessary for good-quality field data with HRM sensors, but note from experience that slowly hand-drilling under multiple viewing angles may be challenging under field conditions, especially where uneven or poor footing exists around trees growing on steep slopes.

Differences in geometry give each type of sensor a unique set of strengths and weaknesses. While HRM sensors are highly sensitive to parallel installation paths for the three sensor prongs, TDP sensors are not. In exchange for this added convenience at the installation step, users lose the ability to monitor reverse flows. TDP users also contend with empirically determining zero-flow conditions, which can vary seasonally based on fluctuating wood water content. Quantitatively robust data from TDP sensors requires site-specific judgements about atmospheric variability to determine zeroing window length. In contrast, HRM sensors directly sense zero-flow conditions.

There are several other notable differences between the sensing platforms. While HRM sensors typically use a transient pulse of heat to initiate measurement, TDP sensors are typically continuously heated. This leads to greater power demands for the same size of installation. Additionally, TDP sensors must maintain a precise operating voltage to "tune" the heat field generated, to enable the use of Granier's empirically derived parameters for converting to sap velocity. These aspects pose challenges both to installation logistics and to data quality assurance. Lastly, at the time of this research, TDP probes were substantially more affordable, and hence maximized the number of trees we could place under observation.

2.2.2 HRM pilot installation

Data from a pilot installation of 35 mm HRM sensors (ICT International HRM30) in coast live oak trees (*Quercus agrifolia*) display several common errors in HRM sensor data, and also demonstrate that sap velocity is not uniform circumferentially around a tree.

Data from some of the installation sites showed consistent offsets between zero and the daily minima, which are expected to be zero or near-zero. Figure 2.4 shows an example of data from three adjacent installation sites on the same tree. In site 1 (figure 2.4 panel a), the data minima are offset from zero in both data streams, but to a greater extent in the deeper site. This is characteristic of asymmetrically crooked sensor prongs, leading to increasing asymmetry with depth. In site 2 (figure 2.4 panel b), the data minima are also offset from zero, but to a similar extent in both data streams. This is typical of conduits that are parallel but subtend asymmetrical tree tissues. This could arise either due to a spacing error, or potentially due to differences in thermal properties of the wood above and below the heater. No geometric errors were obvious during the installation process. Instead, examination of the data for several days after installation can verify installation quality.

The data also show variation in sap velocity magnitude between sites on the same tree. Both sites 1 and 2 (figure 2.4 panels a and b) show sap velocities peaking roughly 3-5 cm/hr above minimum flow (presumed to represent zero flow after accounting for geometric errors). In contrast, site 3 (figure 2.4 panel c) shows peak sap velocities 4-5 times greater (17-20 cm/hr) than those observed at sites 1 and 2. Because there is no way to calibrate sensors prior to installation, we verified the differences in magnitude by swapping new sensors into the three installation sites. As shown in the bottom three panels (h-j) of figure 2.4, we were able to reproduce the pattern of different magnitudes with a different set of sensors, demonstrating that this is due to circumferential variation in sap velocity around the tree.

These non-zero minima could also be showing that the tree maintains overnight flows, with interior tissues at site 1 flowing faster. Choosing between interpretations of non-zero minima as either indicating a real positive flow or a spacing error requires some detective work. We reached our conclusions based on several clues. Firstly, tree physiological function allows the assumption that under low or zero atmospheric water vapor pressure deficit (VPD), trees have no sap flow. Given the weather conditions during the study, we found this line of reasoning sufficient to discard the possibility that the elevated minima were representing real non-zero overnight flow rates. Secondly, the offset minima are

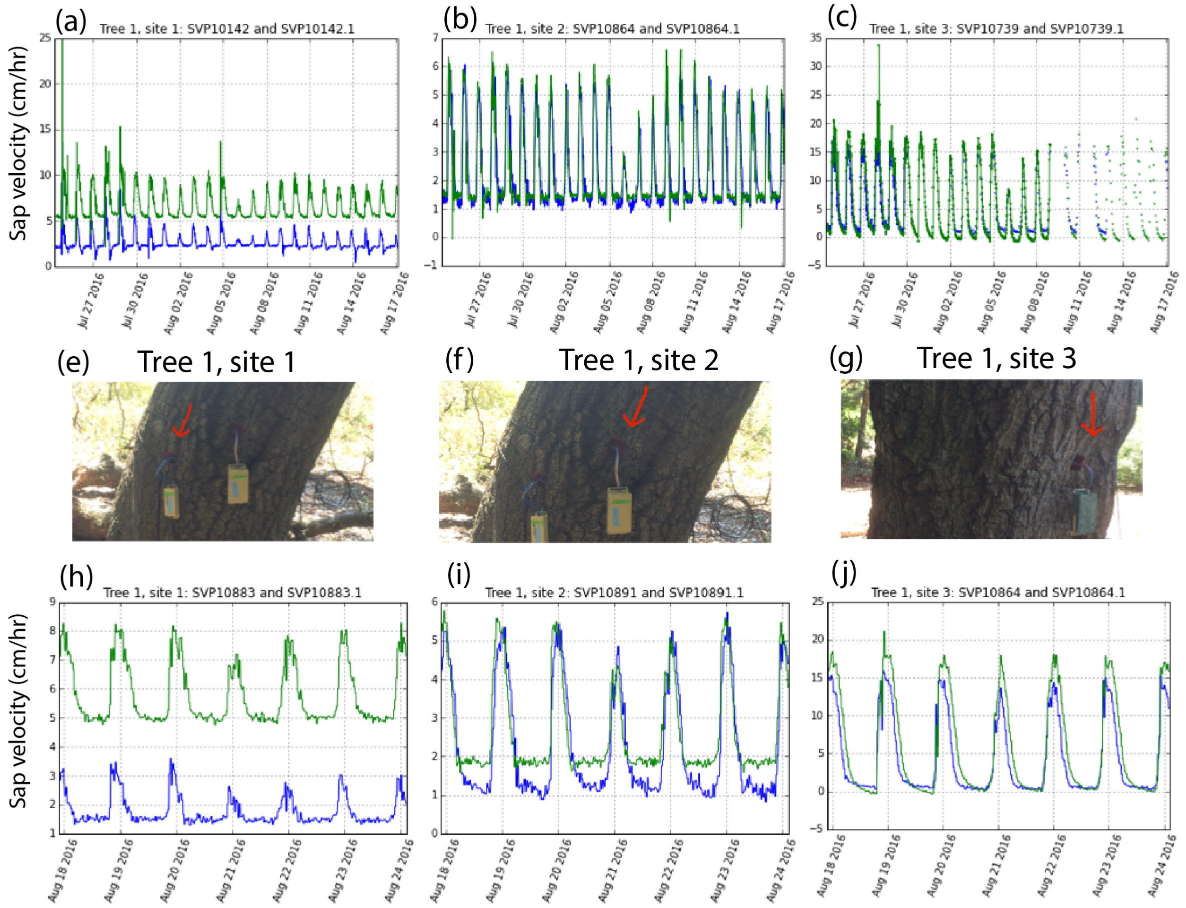

Figure 2.4: Three HRM sensors were installed into a coast live oak tree (*Quercus agrifolia*) at the University of California's Botanical Garden during Summer 2016. The sensors collect data from two depths (tree radii) simultaneously. The blue line shows data collected at 12.5 mm depth, while the green line shows data from 27.5 mm depth. The top panels a-c show data reported over 24 days, while the middle panels show the physical installation sites in relation to one another. The bottom panels show 7 days of data from the same installation sites collected with a different set of sensors.

constant over time, which, even in the hypothetical absence of weather data, would suggest that the trees are not responding to high overnight VPD, which would be a more temporary weather phenomenon if it occurred. Thirdly, another line of evidence we considered was the fact that site 3 (figure 2.4 panel c) reaches zero flow at night as expected. These observations are consistent with the fact that HRM-based measurements at zero flow conditions are only impaired by a violation of the assumption of symmetry, either in probe spacing or in wood thermal properties, above and below the heater.

2.2.3 Environmental sensors

To provide the environmental context for understanding the sap velocity data resulting from our Phase 1 deployment of HRM sensors, as indicated in 2.3, we deployed additional sensors to measure soil moisture, air temperature and humidity on the south slope. These variables were already under observation on the more heavily-instrumented north slope (see site description in section 2.3).

Air temperature and humidity were sensed jointly on a single instrument (Cambpell Scientific CS215). These sensors are straightforward to install and we encountered no complications in the resulting data.

Our soil moisture data were generated by Water Content Reflectometers (WCR, Campbell Scientific CS650), which operate on the principle of Time Domain Reflectometry (TDR). Sensors consist of two long (30 cm) parallel prongs that measure changes in the dielectric permittivity (K_a) of the soil medium between the prongs. Soil permittivity relates to volumetric water content (θ_v) through an empirical relationship derived in [85]:

$$\theta_v = -5.3 \times 10^{-2} + 2.92 \times 10^{-2} K_a - 5.5 \times 10^{-4} K_a^2 + 4.3 \times 10^{-6} K_a^3. \quad (2.4)$$

The dielectric permittivity of soils (K_a) also varies with soil texture and salt content. Though this degree of variation is relatively small compared to that arising from different water contents, it may still introduce systematic differences in TDR measurements arising from different soil mediums. Therefore, in order to confirm the inter-comparability of data from different locations, we undertook soil analyses to determine that, though soil texture changed with depth, there was no significant lateral variation in soil texture found in soils harvested from 30 cm depth around our field site. Because there were also no variations in the underlying rock material from which soils were derived, we presumed that there was no substantial variation in soil salt content around the site without explicitly testing this. Due to soil texture variation with depth, we avoided comparing soil moisture magnitudes from measurements arising at different depths.

2.2.4 Concluding remarks

HRM and TDP sensors both sense sap flow along similar physical principles, but nevertheless have trade-offs that give them distinct advantages in different research settings. Our pilot installation confirmed that HRM sensors are highly sensitive to installation geometry, and further emphasized the degree to which installation errors may be undetectable at the time of installation. This renders accurate HRM data dependent on exacting installation practices. We improved on recommendations for best installation practices by outlining new drilling procedures involving a slower, hand-powered drill and establishment of multiple lines of sight. Our pilot installation also showed variation in sap velocity circumferentially, meaning that a single sensor will not reliably characterize the average rate of sap velocity within a tree. These findings informed our installation design and protocol in Section 2.3.1.1.

2.3 Research aims and Field Installation Considerations

'Rivendell' is a steep, forested, north-facing slope at the University of California's Angelo Coast Range Reserve (39.729N, -123.644W). During the campaign of the Keck Hydrowatch project (2006-2011), it was heavily instrumented. Over a 8000m^2 area, slightly larger than a standard soccer field, over 1000 instruments– weather stations, wells, soil moisture probes, sap velocity sensors, streamflow gauging stations, hanging arrays of temperature and humidity sensors, and a deep (25m) lateral rock moisture sampling apparatus– shed light on the path of water through this ecosystem.

Here, researchers found vegetation deriving nearly 30% of their water from 'rock moisture' from a fractured layer of weathered bedrock beneath the thin soil layer [74]. This helped to explain the water economics of trees that appeared, based on observations of sap velocity, to transpire maximally in the dry summer, up to 3 months after the last rains of the spring [55, 56]. The sap velocity observations also demonstrated that functional differences in the seasonality of tree water use exist between evergreen tree species, even among those traditionally presumed to share functional characteristics (e.g., different species that are both extra-tropical broadleaf evergreen trees). This result showed that the annual distribution of land-to-atmosphere water flux has a species-dependent component.

However, observations stemming from a single north-facing hillslope left uncertainty about the generalizable extent of these results, both across topography and within a species. In 2013, the Rivendell site began hosting the Eel River Critical Zone Observatory, which funded an expansion of instruments to the neighboring south-facing slope. Our research questions ask: "What degree of differential hydraulic function is observable between trees growing in different microclimates? How much of this can be attributed to long-term acclimation to different growing climates?" To investigate whether the rules governing hydraulic function in trees looked similar across the landscape, or whether acclimation to local microclimates plays a substantive role in determining tree water use timing and amount, we used the fact that the adjacent south-facing hillslope experienced a significantly hotter and drier climate.

Our first deployment of sap flow sensors (Phase 1) used HRM sensors to match the type of sensor used previously by [55]. This HRM sensor deployment also shaped our deployment of environmental sensors, which fit around the Phase 1 instrumented trees. Our second deployment of sap flow sensors (Phase 2) moved to a new type of sap flow sensor, TDP sensors. Differences in the sap velocity sensing platform and also the number of sensors available drove the evolution of research aims.

2.3.1 Phase 1

We aimed to directly measure of how much influence a moderate (roughly 2°C) climate difference had on a particular species' water use patterns and quantities, in order to understand how vegetation responses to long-standing climate differences feed back into regional climate via the water cycle.

2.3.1.1 Phase 1: HRM sap flow on Rivendell's south-facing slope

Sap flow observation plans were formulated with the aim of comparing within-species water use on opposing slopes. Because few HRM sensors were available, new observations were taken only on the south-facing slope. The intention was to use a predictive sap velocity model developed for this site to predict sap velocities in a single species from ambient environmental conditions, a relationship which is implicitly based on north-slope tree function for this species, and then analyze how the south-slope observations in this species differed from these predictions. We chose to focus on Pacific madrone (*Arbutus menziesii*), because these trees reach peak transpiration latest in the dry season, as much as three months after the last rains. This was an appealing feature under a hypothesis that a late transpiration peak implies richer access to water resources during the dry season than neighboring tree species, enabling more sensitivity to above ground temperature and humidity gradients between slopes.

11 HRM sensors were available. Eight madrone trees over a small, 35 x 25 m footprint were selected for instrumentation with a single HRM sensor each. HRM sensors were installed on north-facing (up-slope) sides of trees at ∼1.5 m from the ground. The remaining three HRM instruments were reserved as 'rovers' that would move between secondary installation sites on all trees on a weekly basis, thereby capturing a degree of circumferential variation in sap velocities. Alongside sap flow observations, we undertook observations of south slope air temperature, humidity, and shallow soil moisture (30 cm) to generate *in situ* environmental forcing for the predictive sap velocity model. Additionally, we extended safe trail access down the steep slope. Environmental installations are detailed in section 2.3.1.2. See figure 2.5 for a map of the installations.

2.3.1.2 Phase 1: Environmental observations of the south slope

Our motivating research question asks how and to what extent trees of a single species acclimate to long-term climate differences. Our phase 1 investigation approach involves testing whether different quantities or drivers of tree water use could be detected between tree populations inhabiting different adjacent microclimates. However, the challenge of characterizing the microclimates of

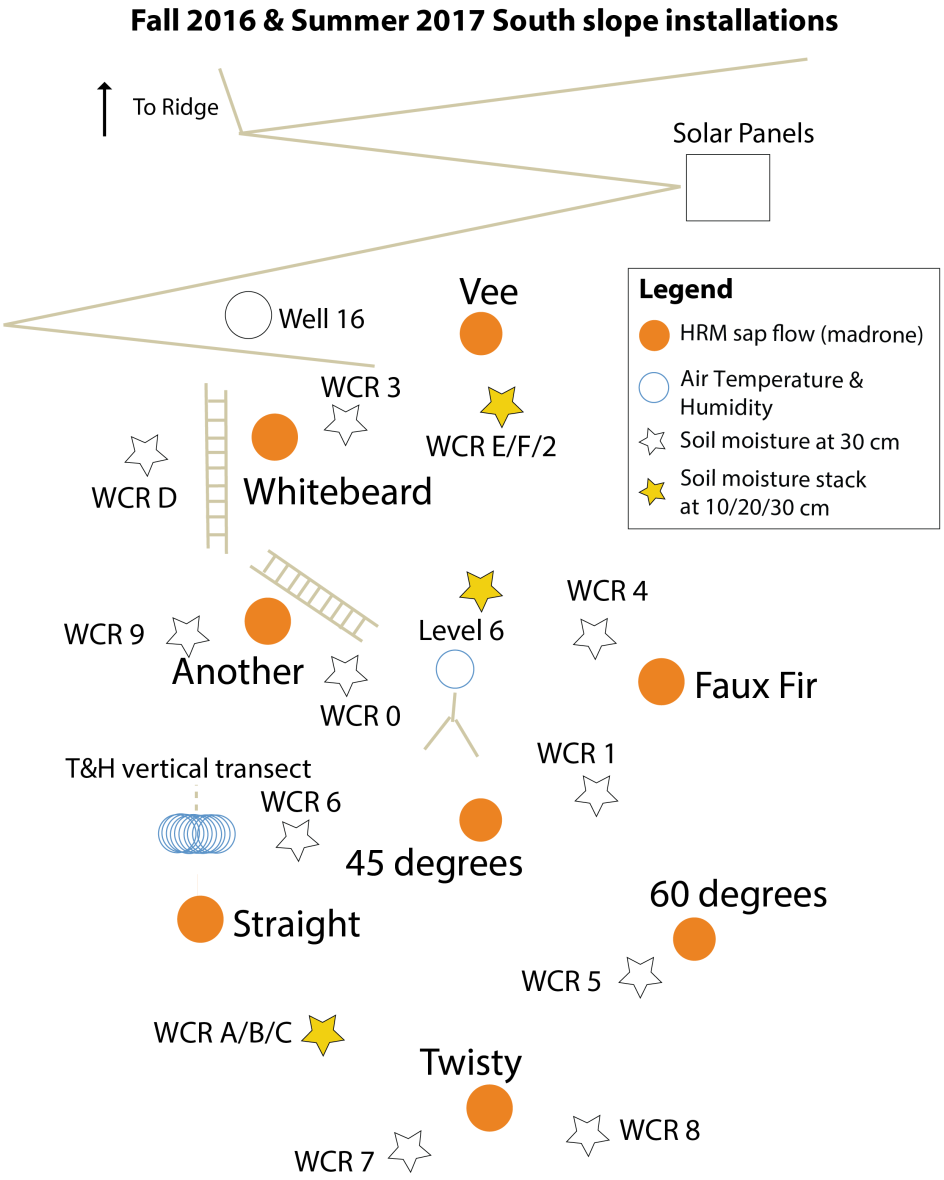

Figure 2.5: See next page for caption.

individual trees with ambient environmental measurements led us to two upstream research questions: 1) What is the relationship between ambient temperature and humidity below the closed forest canopy (2 m above ground) and the higher air space occupied by the transpiring leaves (20-30 m above ground)? 2) Is there transfer of water from the deeper unsaturated vadose zone to the surface soils via hydraulic redistribution at this research site, as

Figure 2.5: (on previous page) A schematic map (not to scale) of the Phase 1 Rivendell HRM sap flow installation, showing the relative locations of sap-flow-instrumented madrone trees, temperature and humidity sensors, and the soil moisture network. The sap flow network was installed in September 2016, the weather station (level 6) was installed in May 2017, the soil moisture network and hanging string of temperature and humidity sensors was installed July 2017. Power for all sensors derived from a solar panel array positioned up the slope. Power for the sap flow installation was routed to a data logger (ICT international Smart Logger) positioned on the tree labeled "Another". HRM sensors from all trees connected to this logger for power and data transfer. Power for the temperature, humidity, and soil moisture sensors was routed to a data logger (Campbell Scientific CR1000X) positioned on the Level 6 weather station. All temperature, humidity, and soil moisture sensors connected to this logger for power and data transfer. Telemetry connections allowed data from Level 6 to transfer wirelessly to remote database storage. The sap flow logger did not have this capability and required manual data transfer.

has been observed in other Douglas-fir-dominated forests [13]?

Alongside the initial HRM sap flow network described in 2.3.1.1, in phase 1 we also installed environmental sensors to capture the local microclimate on the south-facing slope. Our aims were twofold: firstly, to generate forcing data specific to the south slope microclimate for use with the predictive sap velocity model, and secondly, to investigate additional sources of environmental variation that could further inform these aspects of the relationship between ambient environmental conditions and vegetation water fluxes. We designed a sensor network that would mirror the environmental observations available on the north slope, as well as explore these additional environmental features of the south-facing slope.

2.3.1.3 Soil Moisture

The design of the soil moisture array on the south slope was informed by assumptions regarding the scale of soil moisture variability. We hypothesized that soil moisture would show variation on a steep slope, and that trees might therefore have diverse rooting strategies, including variable timing and extent of seasonal switching from shallow to deep moisture (e.g., [26]) or hydraulic redistribution [12, 13]. Our dense network of shallow soil moisture observations (see 2.5) was designed to 1) generate an area-averaged shallow soil moisture variable characteristic of the whole south-facing slope for the predictive sap flow model, 2) characterize each tree's local environment as one line of evidence indicating whether trees seasonally switch to deeper moisture reserves, and 3) capture the signature of hydraulic redistribution, if present.

Soil moisture sensors were deployed during phase 1, and hence occupy the same footprint as the HRM installation. Sensors are mapped out in figure 2.5. To characterize each tree's local soil moisture, we installed two shallow (30 cm depth) soil moisture sensors flanking each sap-flow-instrumented madrone tree on the south-facing slope, with overlap where trees were spaced closely enough (figure 2.5, white stars). This resulted in 13 locations of shallow soil moisture observation around the 8 instrumented trees. To capture the signature of hydraulic redistribution, at three locations we installed nests of three soil moisture sensors stacked vertically 10 cm apart (figure 2.5, yellow stars). To inform our decision of which depths to target with our stacked soil moisture sensors, we analyzed existing soil moisture data from the ridge area of Rivendell and saw that the characteristic 'sawtooth' pattern, attributable to the presence of roots performing hydraulic redistribution, was most prominent at 35 cm. Figure 2.6 shows an example of this pattern from data arising from similar sensors installed at the ridge between the two hill slopes. Because this ridge site lies close to large Douglas fir trees *(Pseudotsuga menziesii)*, we were unsure whether we would see similar dynamics in the soils of the Pacific-madrone-dominated south-facing slope. Though we aimed to install sensors at 20, 30, and 40 cm depths based on this analysis, in the process of installation we ran into layers rich in decomposing fractured rock (saprolite) that were unsuitable for hosting sensors below 30cm, and ultimately installed sensors at 10, 20, and 30cm.

Installation involved digging soil pits and inserting sensors horizontally into the wall of the pit (see figure 2.7). During this process we avoided severing large roots >1 cm in diameter within our soil pits in order to avoid disturbing roots of sap-flow-instrumented trees, and also not to disrupt the root networks that would be driving hydraulic redistribution if it were occurring. To avoid

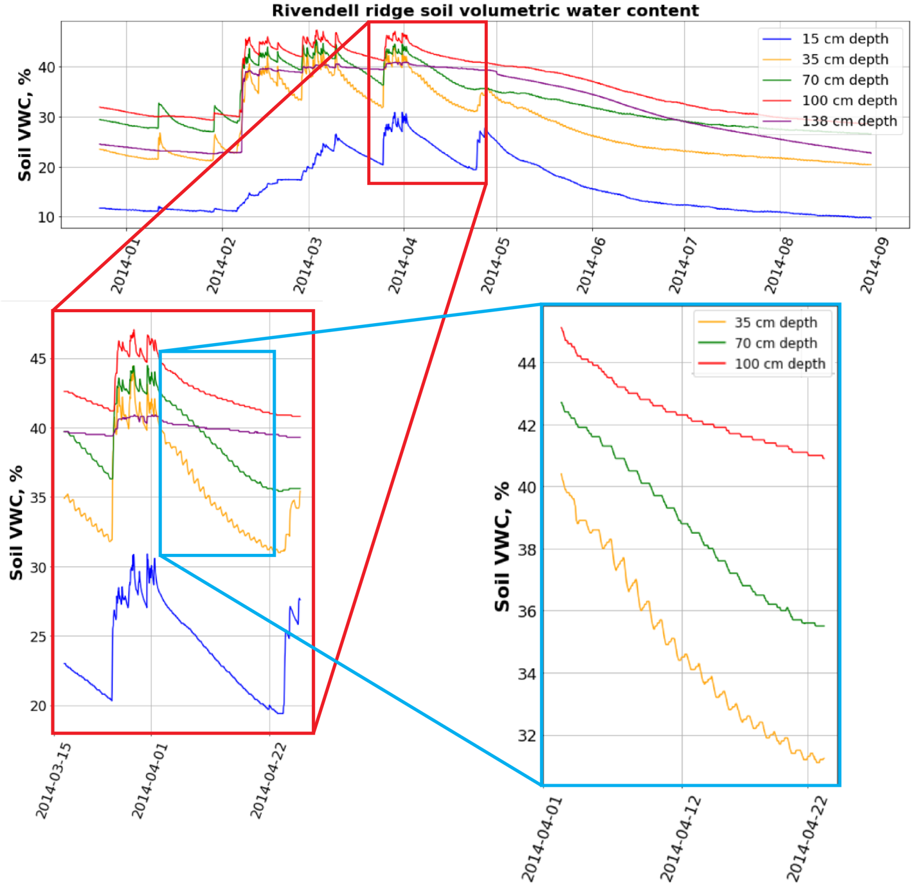

Figure 2.6: Diurnal fluctuations in soil moisture show the signature of hydraulic redistribution in some layers of the ridge zone soils of Rivendell. The 'sawtooth' diurnal pattern visible at 35 cm depth indicates moisture recharge overnight, attributable to hydraulic redistribution through tree roots, in contrast to the 'stairstep' pattern at 70 and 100 cm depths. This site lies proximate to large Douglas firs (<10 m away).

hitting roots or stones along the probe path, we first identified paths with little resistance using a pilot rod and hammer. Because we inserted the probes into undisturbed soils, we could not verify the absolute lack of stones or roots winding between the two parallel probes.

Figure 2.7: A shallow soil moisture probe pictured mid-installation, showing orientation of sensor before being inserted into the undisturbed soil of the pit wall. Large roots traversing the installation site were left intact.

2.3.1.4 Air Temperature and Humidity sensors

The design of air temperature and humidity observations was likewise informed by our assumptions of the scale of variability. We assumed that because ambient air under the canopy is well-mixed during the day, air temperature and humidity would be laterally similar across the 35 x 25 m observational footprint, but may show vertical gradients because the transpiring surface of the canopy is concentrated higher up. Our installations were therefore designed to characterize the mean sub-canopy air temperature at 2 m, as well as observe the relationship between ambient temperature and humidity below the closed forest canopy (2 m above ground) and the higher air space occupied by the transpiring leaves (20-30 m above ground).

A weather station hosting an air temperature and humidity sensor at 2 m was installed in the middle of the eight trees, in addition to a 22 m string of 10 evenly spaced temperature and humidity sensors extending from the canopy to the ground (locations shown in figure 2.5). Air temperature and humidity sensors require a correctly situated radiation shield to reduce signal variability from direct exposure to sunlight. When installing the flexible string of air temperature and humidity sensors, ensuring that all the sensors' radiation shields remained upright while hanging from the canopy was a challenge because we had no rigid structure on which to mount the sensors. To solve this, we engineered a triple-stranded design that anchored the shields in an upright position from three corners. Figure 2.8 shows the orientation of the completed installation.

Figure 2.8: The top four in a string of 10 air temperature and humidity sensors, vertically suspended from a branch in the upper canopy, 25 m above the forest floor. Three strands keep the radiation shields in the correct upright position even under windy conditions.

2.3.2 Phase 2

2.3.2.1 Phase 2: research aims

Electrical failures in the custom data loggers deployed in Phase 1 which were required to power the HRM sensor installation led to a complete redesign of the sap flow installation at Rivendell around a new sensing platform, TDP sensors. Switching sap flow sensing platform from HRM to TDP sensors avoided the sources of error in the Keck Hydrowatch sap flow data, improving our ability to consider quantitative questions. Because of the new potential for quantitative analysis, we expanded the observation footprint to include the north slope, and also to include Douglas firs (*Psuedotsuga menziesii*). We expanded from our existing research questions to additionally ask: "What is the quantitative difference in transpiration flux between a shady north-facing slope and a sunny south-facing slope?" as well as: "What is the quantitative difference in transpiration between Pacific madrone and Douglas fir?"

2.3.2.2 Phase 2: TDP sap flow on both Rivendell slopes

This section describes the design of the TDP installation at Rivendell, and documents the data processing procedure for the TDP sap flow data.

The TDP installation at Rivendell featured two types of sensor: one in which the probe prongs are 100 mm in length and take three radial measurements at 15, 50, and 90 mm depth (shown in figure 2.2), and one in which the probe prongs are 80 mm in length and take two radial measurements at 15 and 70 mm depth. The spacing and number of thermocouples make 80 mm probes suitable for trees roughly 30-75 cm in diameter, and 100 mm probes suitable for trees that are even larger. Smaller trees hosting 80 mm probes received two probes per tree, while three large Douglas firs were the only targets for 100 mm probes and were intended to host four probes per tree. The difference in the number of sensors per tree reflects circumferential differences between the two size classes of tree.

The logistics of setting up a TDP installation are challenging due to the high power load, the precise operating voltage requirements of each sensor type, and voltage attenuation over long cable lengths. Because off-the-shelf infrastructure packages to regulate voltage and log data are expensive, we solved these challenges with our own custom design. We include diagrams and wiring maps of our set up in appendix 2.5.3. After installation, 20 trees spanning both slopes hosted sap flow sensors: 6 Pacific madrone and 4 Douglas fir trees on the north-facing slope, and 8 Pacific madrone and 2 Douglas fir trees on the south-facing slope. Figure 2.9 shows a map of the installations.

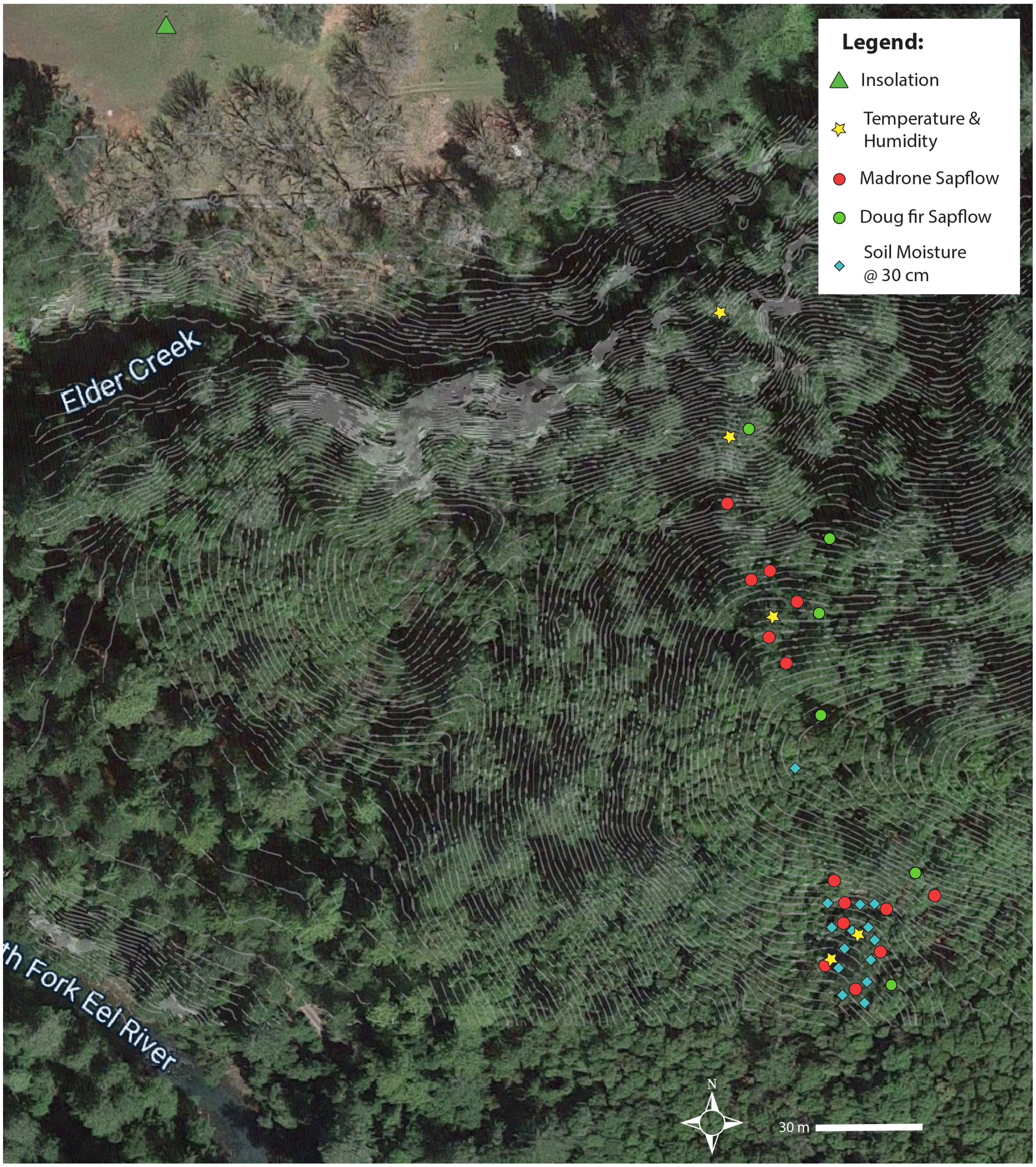

Figure 2.9: See next page for caption.

The small number of south-slope Douglas firs (2) is due to low numbers of the correct size class within our observational footprint. Because there were so few south-slope Douglas firs, and those that were there experienced data

Figure 2.9: (on previous page) A map of the study site in Northern California (39.729°N, 123.644°W), and the locations of data for this analysis. The canopy covering the north slope is largely made up of Douglas fir (*Pseudotsuga menziesii*), bay (*Umbellularia californica*), and evergreen oak tree species (Tan oak *Notholithocarpus densiflorus*, Coastal live oak *Quercus agrifolia*, Canyon live oak *Quercus chrysolepis*), with some Pacific madrone trees (*Arbutus menziesii*) in the upper half of the hillslope. In contrast, the south slope is mostly populated with Pacific madrone trees, with a few Douglas fir and oak trees primarily occurring in the upper half of the slope near the ridge. One-meter topographic lines are shown in light gray. Underlying high-resolution satellite imagery is from Maxar Technologies, accessed through Google Earth Engine [33].

disruptions from power outages, ultimately we compared transpiration between slopes using Pacific madrones only (see chapters 3, 4 and 5), and compared transpiration between species using north-slope trees only (see chapter 3.2).

2.4 TDP Data processing

Data processing for TDP sensors has several steps, some of which rely on qualitative judgments that have the potential to impact the scale of the signal. Because of this, we are documenting our processing protocols.

Prior to analysis, we processed our sap flow data in the following steps: 1) cleaning the raw data, which are in the form of reported temperature differences between the two prongs (dT), 2) applying a standard zeroing procedure to each data stream using a 5-day window to determine zero-flow conditions, and lastly 3) converting the temperature differences to sap velocities using Granier's equation [35, 34]. In some analyses, we used population averages of sap velocity. Before computing population averages, we took steps to identify and remove outlying data streams.

2.4.1 Data quality assurance and cleaning:

Data cleaning involved hand-identifying problem areas, deleting untrustworthy data, and gap-filling with NaNs. Gaps in data and data quality arose from power outages in the solar system at the field site (illustrated in figure 2.10 panel b), failures of voltage regulators that controlled the power delivered to the sensors, exposure of weak electrical junctions to variations in temperature and humidity (illustrated in figure 2.10 panel b), software updates to data loggers which impacted the loggers' time keeping, and animal disturbance. The signature of these external factors, when contrasted to the degrees and types of natural data variability, was generally easy to identify. Nevertheless, individual decisions made in diagnosing and handling these issues have the potential to affect accuracy in both timing and magnitude of the clean data. Therefore the QA/QC process for each data stream is presented in detail in code notebooks published at [7].

2.4.2 Zeroing procedure:

The zeroing procedure uses a rolling 5-day window as the period over which the maximum observed temperature difference ($d\mathrm{T}_{\mathrm{Max}}$) between the sensor's upper and lower thermocouple junctions is interpreted as corresponding to zero-flow conditions. In standard practice, $d\mathrm{T}_{\mathrm{Max}}$ is identified over a local window of time. $d\mathrm{T}_{\mathrm{Max}}$ is essentially a measurement of the temperature reached in the center of a heat field generated by diffusion of a constant heat from the heated probe into a low- or non-flowing matrix of wood and water, and is therefore sensitive to the heat capacity of the living wood. This varies substantially over time with biological changes in wood water content within tree trunks, which can be impacted by rainfall or dry heat waves [89]. $d\mathrm{T}_{\mathrm{Max}}$ is also identified uniquely for each thermocouple pair, as the wood water content of individual installation sites is variable both around the circumference of a tree and with depth. Two data streams on opposing sides of the same tree cannot be assumed to have the same zero, as the proportions of lignin, cellulose, and water which determine the local heat capacity of the wood vary around a tree trunk in unpredictable ways. Similarly, for the same reason two data streams arising from the same sensor at different depths within the tree trunk will not have

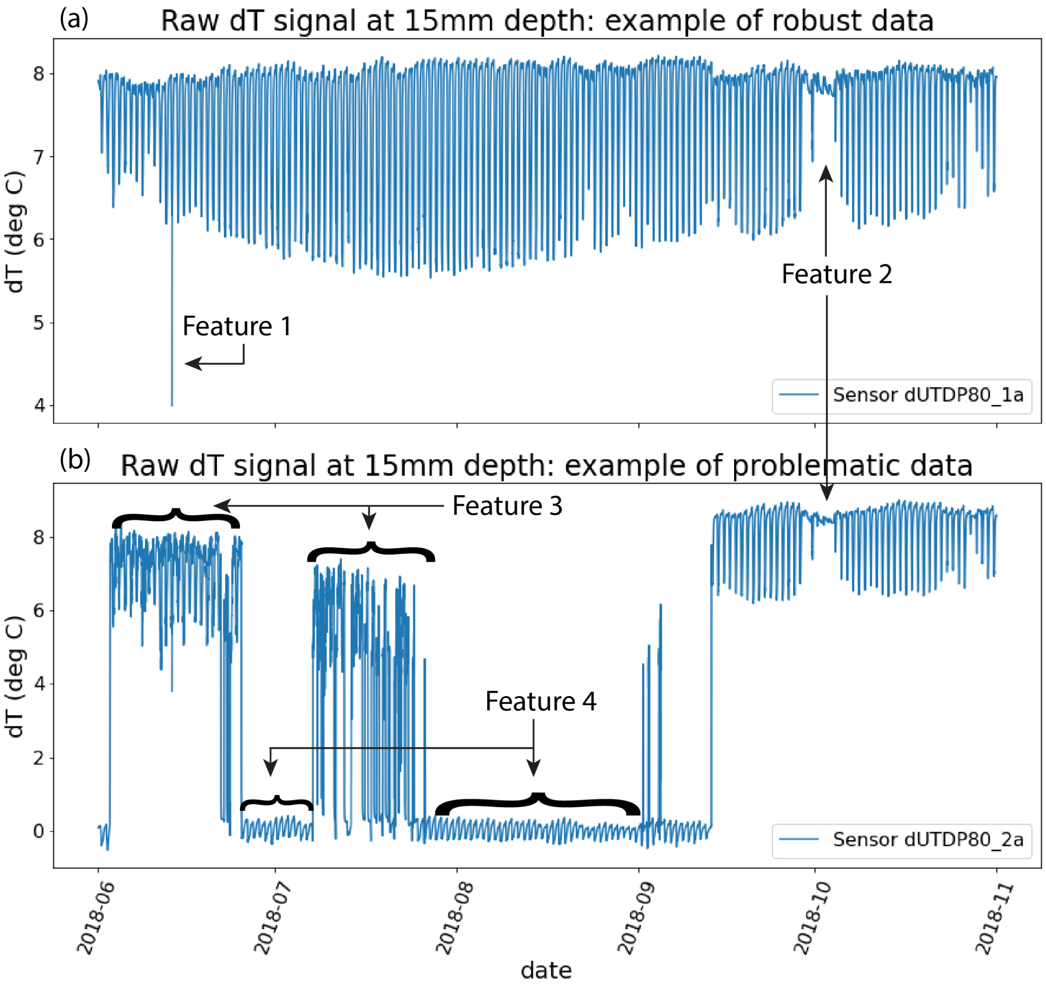

Figure 2.10: See next page for caption.

the same zero, despite sharing the same heated upper heated probe. See figure 2.11.

The choice of zeroing window duration is informed by the estimated rate at which wood water content changes substantively in the studied ecosystem. A window which is too short masks possible night-time flows and underestimates daily peak sapflow during dry spells, while windows that are too long introduce errors during moist conditions. Not all trees showed the same extent of wood water content variability. Here, we chose 5 days to capture weather-induced variability in wood water content in the most responsive trees.

Figure 2.10: (on previous page) Common features of the raw data are demonstrated here. Sensor dUTDP80_1a, in the top panel, is an example of robust data that went through minimal processing, while sensor dUTDP80_2a, in the bottom panel, shows problematic data that required extra steps. In both panels, each day shows a cycle of $d\mathrm{T}$ decrease and then increase as sap velocities speed up in the morning, advecting heat away from the heated junction, and then slow down in the afternoon, diminishing this cooling effect. Feature 1 shows the impact on $d\mathrm{T}$ of brief electrical disconnections typical of installation maintenance. Feature 2 is a natural signal of high $d\mathrm{T}$ during a rain storm, when sap velocities are near zero. Feature 3 shows the unusually variable $d\mathrm{T}$ and $d\mathrm{T}_{\mathrm{Max}}$ typical of intermittent electrical disconnections caused by faulty wiring. Feature 4 shows the background signal of sensed temperature gradients within the tree when the heaters are disconnected. The cycling of this background temperature gradient is driven by the daily warming of the tree trunk by the ambient air temperature, causing water in the xylem to experience warming on its journey from the cool subsurface up the relatively warm tree trunk. Due to the low $d\mathrm{T}_{\mathrm{Max}}$ and the high sensitivity to ambient air temperature, this signal is not possible to interpret as sap velocity under the Granier equation.

2.4.3 Conversion to sap velocity:

Sap velocity was derived from temperature differences between the upper and lower thermocouple junctions, as in [34] (See equation 2.6).

The empirical parameters a and b are tailored for $d\mathrm{T}_{\mathrm{Max}}$ values of approximately 10°C. As seen in Figures 2.10 and 2.11, $d\mathrm{T}_{\mathrm{Max}}$ was not always 10°C. Studies examining the impact of parameter choice on the accuracy of conversions from $d\mathrm{T}$ to sap velocity have found that accuracy improved with parameters custom-derived for species type [83]. Because it was logistically infeasible run the types of experiments necessary to fit our own custom parameters for Pacific madrone, we adopt Granier's original parameters for Douglas firs with a minor scaling differences to result in units of cm/hr:

$$a = 42.84, b = 1.231, \tag{2.5}$$

Resulting in a final formula of:

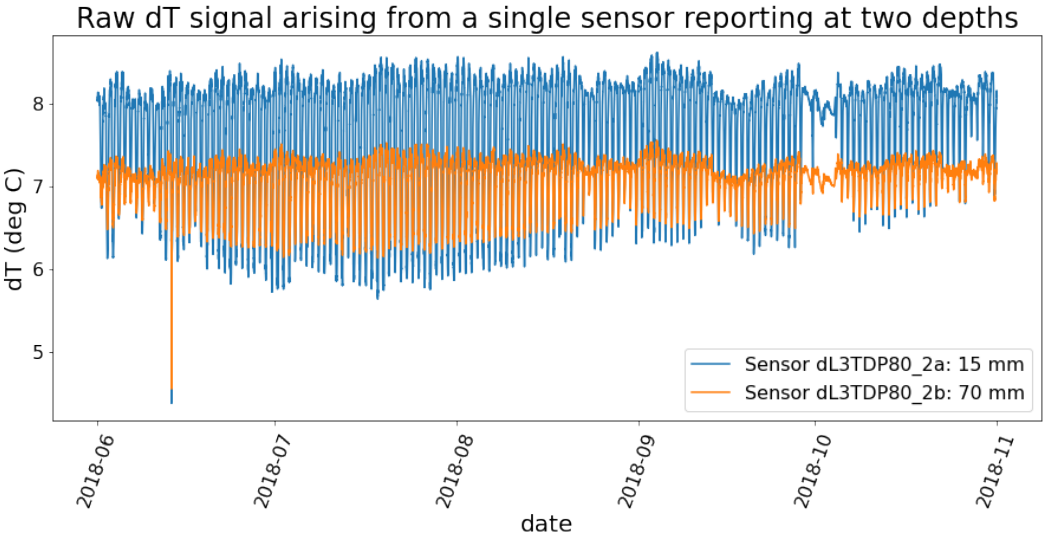

Figure 2.11: Raw data from a single instrument with two sensing junctions at different depths shows the variability in $d\mathrm{T}_{\mathrm{Max}}$ within a single data stream attributable to changing weather conditions (seen as the 'wiggle' in the maxima of the blue and orange signals), as well as the offset in $d\mathrm{T}_{\mathrm{Max}}$ due to changes in wood composition with depth within the trunk (seen as the consistently lower $d\mathrm{T}_{\mathrm{Max}}$ of the orange line compared to that of the blue line). The variability in $d\mathrm{T}_{\mathrm{Max}}$ within a single data stream between the inner and outer junctions of a single probe set demonstrate why $d\mathrm{T}_{\mathrm{Max}}$ must be computed over a local window of time and for each data stream separately.

$$u = 42.84 \times \left(\frac{(d\mathrm{T}_{\mathrm{Max}} - d\mathrm{T})}{d\mathrm{T}}\right)^{1.231} \tag{2.6}$$

Figure 2.12 shows the sap velocity traces resulting from the raw data examples shown previously in figures 2.11 and 2.10.

The impact of using parameters that were not customized to Pacific madrone or varying $d\mathrm{T}_{\mathrm{Max}}$ on the resulting accuracy of computed sap velocity is unknown. Because of this, confidence in magnitude-based comparisons between individual data streams is lowered. However, based on the parameter sensitivities shown in [83], we are confident that the variability in sap velocity magnitudes seen in the final data are reflective primarily of real differences in sap velocity, controlled by biological differences in overall tree function and

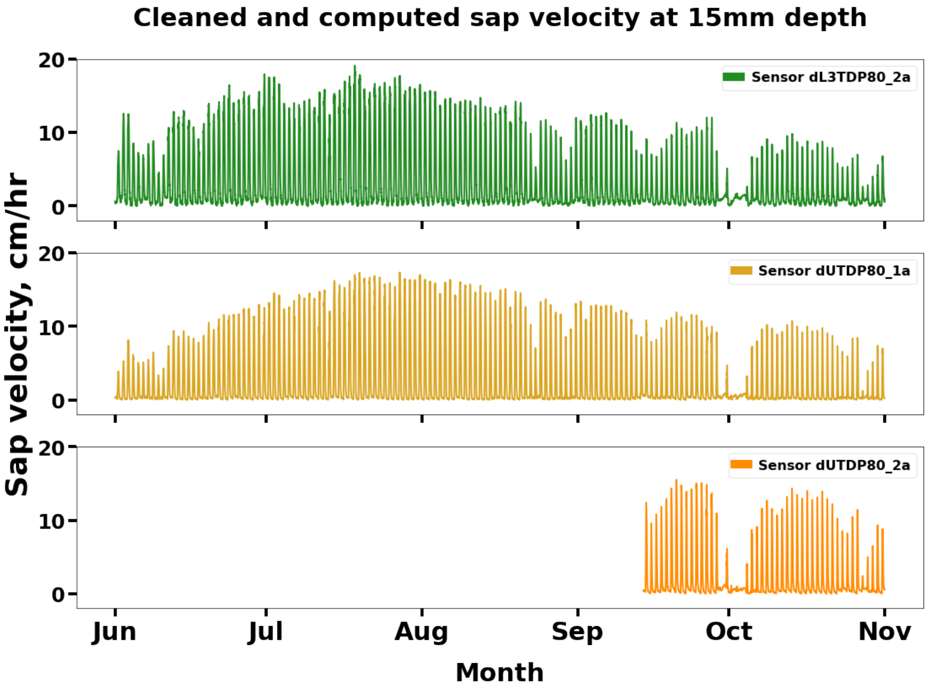

Figure 2.12: Final sap velocity data derived from the raw data examples shown in previous two figures. After zeroing over a local window, sensor dL3TDP80_2a (top panel) shows less variability in nighttime low flows, but still displays more variability in nighttime low flows than sensor dUTDP80_1a (middle panel). This extent of difference is interpreted as real biological variation in nighttime transpiration. Sensor dUTDP8_2a shows the truncated data stream that remains after unreliable data were discarded.

varying distributions of fast-flow or slow-flow tissues within the trunk. Furthermore, because the extent of this variability is similar within each slope's tree population, we consider that impacts arising from non-customized parameters is uniform across the slopes and does not affect the validity of our population-to-population comparisons.

2.4.4 Removing outliers, averaging by slope, and uncertainty analysis:

Some analyses used population averages as their basis. Before computing the mean sap velocity characteristic of each slope or species, we remove outliers on a sensor-by-sensor basis, relative to each slope's group of sensors. We define outliers as data streams with a seasonal mean sap velocity falling outside the range of twice the inter-quartile range (IQR) of seasonal means within the slope's group of sensors away from the slope-averaged seasonal mean sap velocity (with no outliers excluded).

After excluding outliers, all remaining data streams were averaged together by slope, resulting in a sap velocity time series for an average north-slope madrone tree, an average north-slope Douglas fir tree, and an average south-slope madrone tree. Because the medium of living wood and moving water hosting the sensors is unique to each installation site, traditional sensor calibration and error analysis is not possible. Therefore, we interpret the standard deviation of our average-tree data streams as representing total uncertainty in our measured sap velocity magnitude. This is illustrated in Figures 3.3 and 4.2.

2.4.5 Conclusions and lessons learned:

The redesign of the sap flow installation was spurred by an equipment failure and an inability to access product support. Swapping HRM sensors for TDP sensors is not possible in all settings, but because the initial HRM data at our site showed that flow minima did not vary substantially (<1 cm/hr) in the presence of substantial weather variability, and that reverse flows in the trunk did not occur, we found the trade-offs between HRMs and TDPs to be overall in favor of TDP sensors for this setting. Moving to the new platform had the added benefit of enabling quantitative dimensions of our research agenda.

Given the irregularity of tree spacing in a natural forest and cost limitations, we found that installing and interfacing with our own data-logging and voltage-regulating equipment was preferable to off-the-shelf options. Working around limitations in suitable trees, available field power, and voltage drops over long cable lengths proved time consuming but cost-effective (see Appendix

A). Though our installation was tailored to this specific array of trees, the added permanent infrastructure necessary to support this installation will enable future expansion of sap flow monitoring at this field site, on any trees.

2.5 Results

This section covers results from exploratory analyses of HRM and environemental data streams.

2.5.1 Results from Phase 1 HRM sap velocity at Rivendell:

HRM sap flow installations operated well for roughly a month before a combination of electrical failures in data loggers prevented further data collection over the following year. The symptoms of logger failure included inconsistent data collection rate (switching from 15-minute reporting to hourly reporting), unreliable internal timekeeping (occasionally overwriting stored data due to shared timestamps), and generally unreliable powered operation (internal battery became discharged at random and the logger powered off). The data logger failures delayed and ultimately prevented deployment of ‘roving’ sensors. Because the sensors and loggers operated with customized hardware connections and logging software that was not made available by the manufacturer, repairing the platform without technical support was beyond our capacity. After failing to access technical support from the manufacturer, we did not find a resolution of these issues, and ultimately the HRM installation was removed in Fall 2017.

Despite the unfortunately short duration of data collection, the HRM sap flow data from Rivendell’s south slope contain several significant features, and fortuitously the observation period captured two rain events (seen as multi-day periods of low sap velocities). See figure 2.13. Firstly, the resulting data show that overall the installation quality was good, following the best practice of using a slow hand-powered drill and engaging secondary lines of sight during drilling. Four of the eight trees had no installation abnormalities, and the issues visible in the remaining four were minor. Secondly, some trees showed

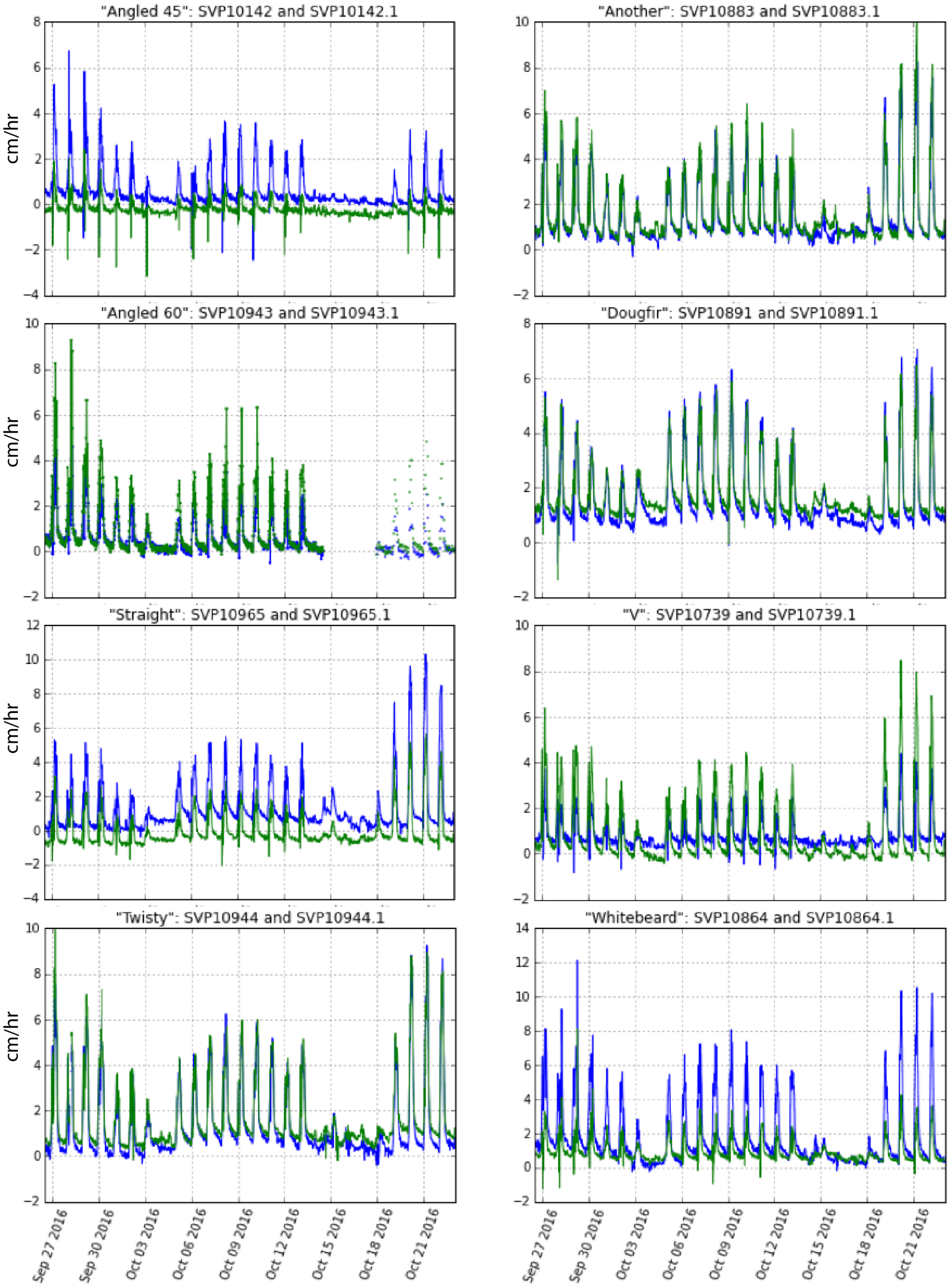

Figure 2.13: See next page for caption.

Figure 2.13: (on previous page) HRM sap velocity data for eight madrone trees, September 27-October 22, 2016. Trees ‘Another’, ‘Angled 60’, ‘Twisty’, and ‘Whitebeard’ show signs of good installation geometry, with both data stream depths (green and blue lines) reaching similar minima and achieving zero flows over the observation period. Minor offsets between data streams in trees ‘Angled 45’, ‘Dougfir’, ‘Straight’, and ‘V’ indicate minor geometric abnormalities. Rain events October 3-4 and 15-18 depress sap velocities to near-zero from a combination of leaf wetness and high ambient humidity.

nocturnal flows of <1cm/hr following the first rain event (see e.g., ‘Twisty’). Thirdly, most (but not all) trees showed a substantial uptick in peak sap velocities following the second, larger rain event, suggesting a previous state of water limitation in these trees. Fourthly, we interpret the data as showing no negative flows, including during the rain events. Though it is unknown what causes the downward spikes below zero visible in figure 2.13, the short duration of these spikes suggests a signal processing issue in the software rather than negative flows. We cannot be more specific in our interpretations because we did not have access to the software, or to technical support. A lack of negative flows matches expectations for the location of the sensors (breast height in the trunk), but is nevertheless useful confirmation. Deeper analysis of the environmental response of these sap velocities, including contrasts with the output of the predictive sap velocity model, was not pursued due to the short duration of the data.

2.5.2 Results from south slope environmental sensors at Rivendell:

2.5.2.1 Soil moisture:

The soil moisture array showed minimal traces of hydraulic redistribution at 30 cm, or in the case of the stacked sensors, above 30 cm. Data at all depths showed clear ‘stairstep’ declines. From this we concluded that, in contrast to Douglas firs, root properties of Pacific madrone trees do not lead to hydraulic redistribution at our site. This could be due to several reasons that we did not have the means to test further: 1) madrone roots may present higher resistances to flow within the roots; 2) madrone root masses may present higher cumulative resistances over the root network if the root mass of madrones is small compared to that of Douglas fir; and 3) madrone rooting distributions may differ, and may possibly subtend smaller soil water potential gradients in comparison to Douglas firs.

Volumetric soil water content at 30 cm showed a surprising degree of spatially organized variation, which persisted in both wet and dry seasons of the year. Spread among the sensors during the wet season ranged from 10-40% soil volumetric water content, while dry season spread ranged from <1-15% soil volumetric water content. A further surprise lay in the spatial organization of the variability. Though in theory shallow soil moisture is expected to become monotonically wetter as one moves down slope due to expected water storage patterns in a hill, the organization of the variability did not follow the slope position. The wettest zone was at the bottom of the slope as expected, but the driest zone lay directly above this on the eastern portion of the mid-slope, while a still-dry but slightly wetter zone occupied the western portion of the mid-slope, and the up-slope zone had the second wettest soils. Figure 2.14 shows the spatial organization of the shallow soil moisture.

Because possible non-soil materials between probes could be a source of systematic variability influencing this spatial pattern, we manually sampled soils from the driest zone and the wettest to confirm systematic moisture variation in these adjacent regions. Our manual soil sampling protocol involved digging a pit in each soil region 70 cm deep and sampling undisturbed soils from the pit wall at varying depths. Our analysis yielded gravimetric water content rather than volumetric water content, yet the ordinal signal of the samples agreed with the sensor network: the dry region was drier than the wet region. We also observed systematic differences in rooting density between the two soil pits, with the dry zone showing sparser roots than the wet zone (Figure 2.15). From this we conclude that 1) the soil moisture sensor network is capturing ordinally accurate spatial variation in shallow soil moisture on this hill slope, though the precise magnitudes are unverified; and 2) tree root distributions respond to these patterns by clustering the wetter zones. We acknowledge that denser rooting in the wetter zones may amplify the soil moisture signal detected if roots invade the probe space, due to the greater presence of water

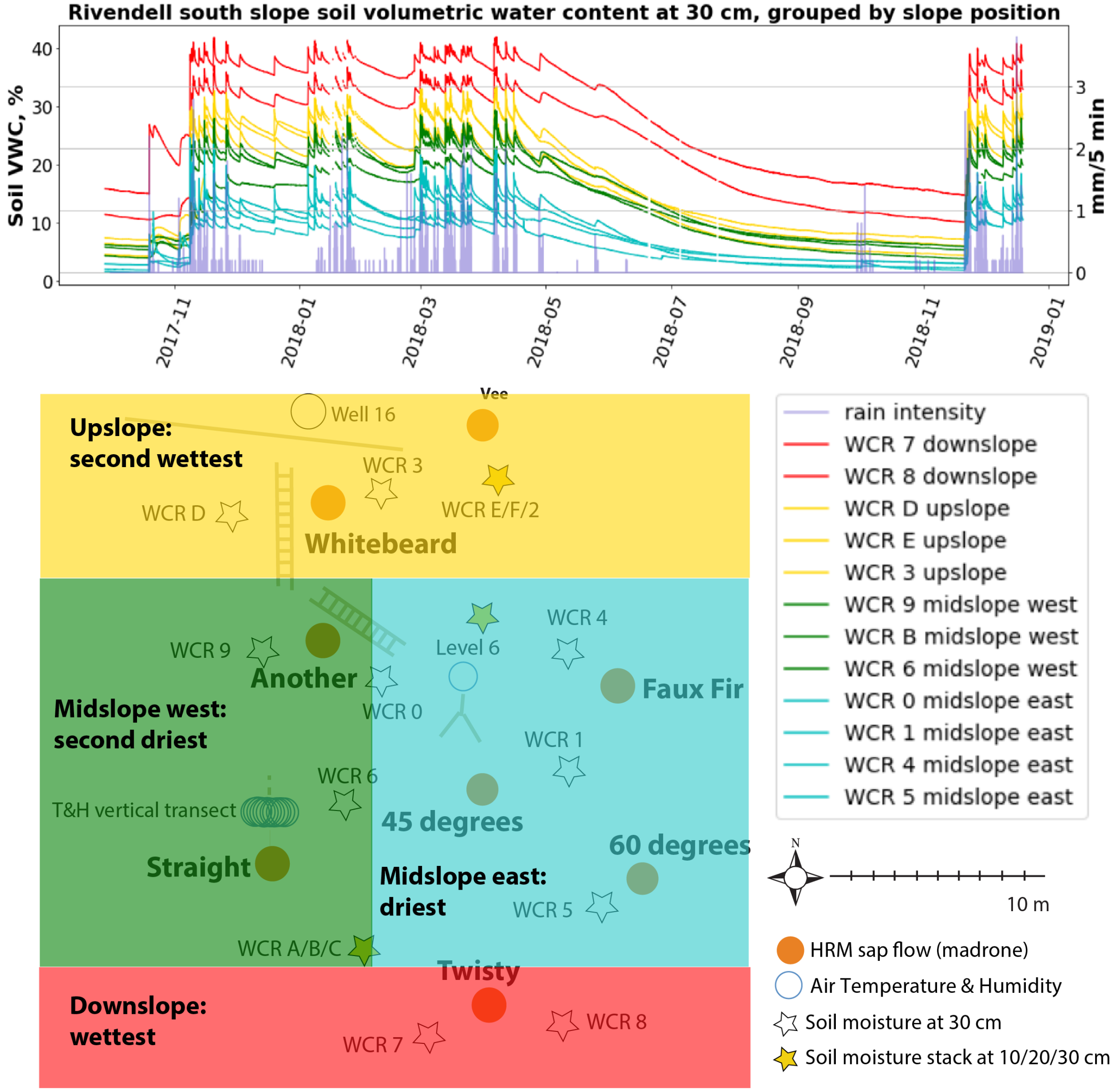

Figure 2.14: Shallow soil moisture (30 cm depth) showed high variability and clear spatial organization.

in root tissues than in soil.

To explain the spatial organization of variability, we revisited the question of whether the classic view of hill slope hydrology, in which water moves vertically though a soil column to a permeable layer and then down slope to a point of drainage (as illustrated in [75]), was applicable at our site. The soils within our sampling footprint lay atop a uniform parent material of argillite

Figure 2.15: Root density in the wet soil region was noticeably higher than that in the dry soil region.

mudstone, in between two lateral ridges of sandstone to the east and west of our sampling footprint. Based on the topographic features and underlying geology, geomorphology experts at our Critical Zone Observatory determined that discontinuities in the sandstone-mudstone boundary on the eastern side of our footprint were generated by a relict landslide that scooped out the mid-slope region of the site. Because the sandstone holds more water than the mudstone, this disturbance could have created paths of lateral water flow arising from the sandstone ridge to the east which then wet the mudstone soils. Based on the shape of the landslide scoop, it was determined that these lateral flow paths plausibly exist in the upper and lower regions of the hill slope, but are disrupted in the mid-slope regions. This speculative explanation of the unexpected spatial pattern of moisture variability suggests that this degree of surface soil moisture variability may be common outside of this field site.

For the purposes of estimating the impact of this degree of soil moisture variation on transpiration, assumptions about rooting quantity and distributions over a hypothetical region of whole-root-zone-moisture are needed. For instance, assumptions of lateral rooting extents inform the degree to which trees may ‘smooth out’ the observed scale of shallow moisture variability, while assumptions about vertical rooting extents, coupled with assumptions about the moisture profile in the subsurface, further impact whether the shallow soil moisture variability is a good proxy for whole root zone moisture. Under the simple assumption that the surface variability extends to similar variability in total root zone moisture, then in the predictive sap velocity model for Pacific madrone of [56, 55], this range of variability represents the entire spectrum of functional transpiration sensitivity to total root zone moisture, ranging from conditions too dry to support any transpiration under 10% VWC (values shown by all but two sensors in dry, pre-rain conditions) to non-limiting conditions above 25% VWC. We explore this assumption in more depth in section 3.1 in the context of sap velocity data, but ultimately determined that this simple assumption was implausible in the face of brisk transpiration activity in all instrumented trees. Without more extensive field sampling, we could not determine the magnitude of variation in total root zone moisture on an individual basis. Instead, recognizing the common dynamics of all data streams, future analyses take a site-averaged soil moisture state to represent a dynamic rate of moisture decline common to all trees.

2.5.2.2 Results from the air temperature and humidity string

The hanging string of air temperature and humidity sensors operated for 18 months before going offline due to animal disturbance. In that time, the string showed a seasonally-changing vertical gradient of vapor pressure deficit (VPD), a measure of the remaining water holding capacity of the ambient air based on combined temperature and humidity conditions, between the canopy and forest floor. Figure 2.16 shows that the bottom sensors showed more daily variability than those higher up, so that departures from the mean conditions of the sensor string were driven primarily by changing surface conditions. Hu-

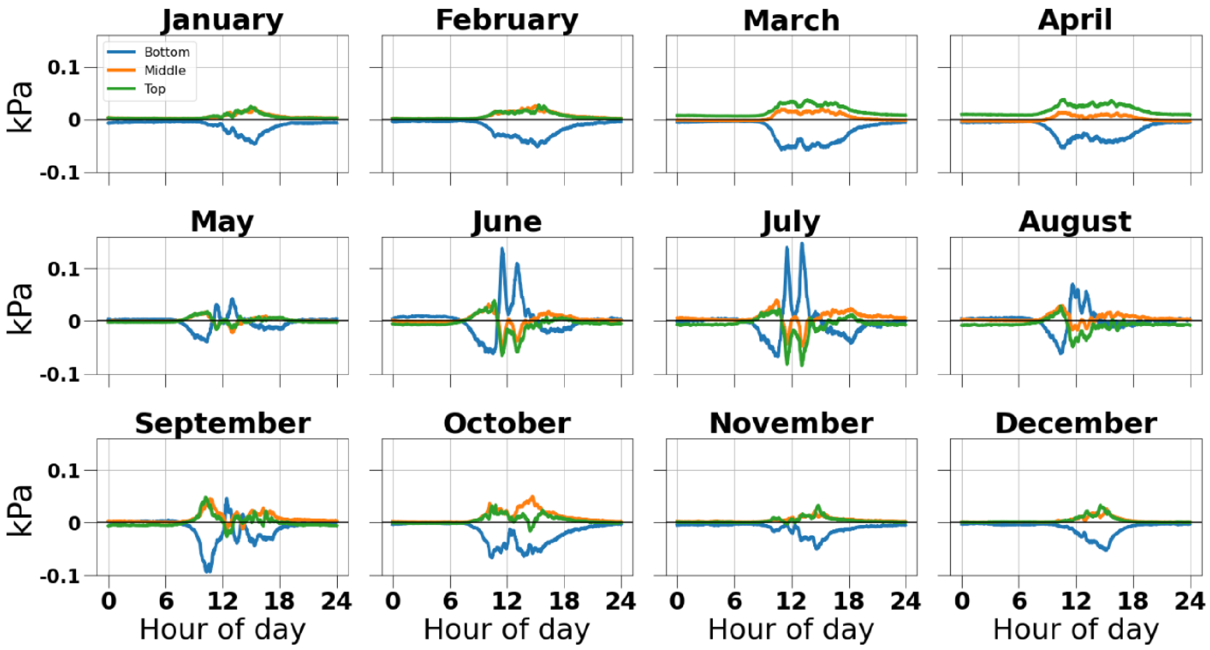

Figure 2.16: Monthly climatological departures from mean conditions in VPD are shown for the bottom three sensors, the middle four sensors, and the top three sensors, derived from data spanning September 2017 to April 2019. The grouping of the sensors serves to highlight the seasonally shifting climatic gradient from the canopy to the forest floor, and mean conditions are computed by averaging values over the entire sensor string. The sensors are spaced roughly 2 m apart, so that the bottom three sensors span the lower 6 m of the 22 m string, while the top three span the upper 6 m. The string displays climatic gradients that change seasonally, responding to shifting surface conditions in soil moisture and solar radiation. The VPD differences between the bottom (blue) and top (green) of the string in the month of March are driven primarily by differences in relative humidity, while the differences in June and July are driven more by differences in temperature arising from transient solar heating from sunflecks.

midity differences along the string are driven primarily by seasonal shifts in evaporation from soils, and are maximized in March, when the average among the bottom three sensors can reach a peak humidity 5% higher than that shown by the average among the top three sensors of the string due to their closer proximity to moist sunlit soils. Temperature differences along the string are driven by the changes in solar heating from below, which beneath the canopy is dominated by the presence of temporary sunflecks heating the forest floor. Temperature differences are strongest over the summer and are maximized in June, when the average among the bottom three sensors reaches twin peaks 1.2°C and 0.9°C hotter than that shown by the average among the top three sensors of the string. In July, higher ambient temperatures in combination with lower humidities lead to maximal VPD differences along the string of sensors.

The primary question we wanted to address with this installation was whether these gradients were large enough or seasonally variable enough to warrant a systematic adjustment of VPD data streams collected at 2 m when attempting to understand the responsiveness of transpiration to environmental conditions. Ultimately, we did not do this. We reasoned that the temperature impact of temporary sunflecks is not generalizable to the remainder of the site, and though in contrast the impact of moist soils is likely to be systemic around the site, this effect was largest in the winter months, which were excluded from our subsequent analysis. Nevertheless, the gradients usefully shape the intuition that conditions sensed at the ground are more seasonally variable but overall substantially similar to those aloft in the canopy. Temperature variability due to temporary changes in solar gain both on the ground (sunflecks) and within tree canopies (neighbor- and self-shading) is a likely source of out-of-phase variability in VPD data streams from beneath the canopy and sap velocity.

2.5.3 Conclusions and lessons learned:

The deployment of HRM sap flow at Rivendell led to several key conclusions that supported our eventual transition away from the HRM sap flow platform to the TDP sap flow platform. Our environmental installations on the south slope successfully served the dual aims of providing forcing data specific to the south slope microclimate for use with the predictive sap velocity model developed by [56], and investigating additional sources of variability in VPD and soil moisture. We learned:

1) Reverse sap flows in the trunk were not seen, including during the first rains following the summer-season dry spell.

2) Overnight sap flows are possible under a combination of well-watered conditions and dry weather, as seen between the two October 2016 rain events, but they are small when they occur (<1cm/hr).

3) Even under best installation practices, slight geometric errors (<1cm/hr) impact the reported sap flow magnitude in HRM sensors.

4) Hydraulic redistribution by tree roots is detectable in shallow (<1m) soils at the ridge, an area close to large Douglas firs. In contrast, hydraulic redistribution is not detectable in the shallow soil layers of the south slope, an area dominated by Pacific madrone.

5) There exists significant variability in shallow soil moisture (10-40% during the rainy season) on the south slope, in a spatially coherent pattern suggestive of lateral flows deriving from a landslide disturbance. Tree roots respond to this surface soil moisture variability by clustering more densely in the wet regions. We do not believe this variability accurately represents the degree of functional variability in moisture available to trees.

6) Gradients in temperature, humidity, and VPD between the canopy air space and the forest floor are present and seasonally changing, driven primarily by changing surface conditions rather than by changing transpiration fluxes in the canopy air space. Both sunflecks and seasonally evolving soil moisture have an impact on the strength of the gradient.

These conclusions justified our switch from HRM to TDP sensors, and also the simplified environmental framing of the sap velocity model. The major strength of HRM sensors lies in capturing reverse and overnight flows. In the madrones at our field site, the extent of overnight and reverse flow was small and comparable to the degree of geometric installation errors even under best practices. This suggests that our research aims would be equally well-suited to a TDP sap flow sensing platform. To represent the dynamic environmental conditions of the south side tree population, we use site-averaged variables in soil moisture and VPD.

The environmental data also suggest additional avenues of investigation. For instance, the importance of sub-canopy gradients in air temperature and humidity could be further informed by screening for windy conditions, because gradients are expected to be maximized on days with little wind. Investigations into the deeper rocky layers of the vadose zone through the usage neutron probes down boreholes, or tracking water potentials at the trunk or roots of trees, could help constrain the hypothesis space regarding rooting depth and density distribution. Excavation of madrone roots and installation of HRM sap flow sensors on these roots could directly investigate the existence of hydraulic redistribution in madrone root systems by tracking the direction of sap flow, while psychrometers measuring stem water potentials on these roots could better inform the soil conditions under which hydraulic redistribution occurs.

Appendix A

TDP deployment plans

A.1 Wiring diagram

The following figures illustrate the wiring of the TDP installation. 8-stranded cable carried data and power between multiplexers on each instrumented tree and centrally-located data loggers. Separately, power cables carried specially-tuned power from voltage regulators to TDP sensors.

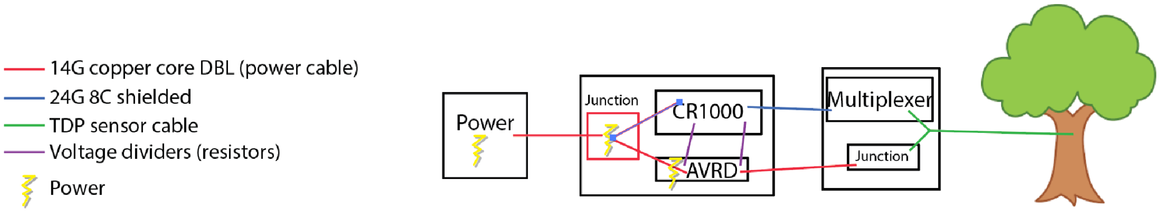

Figure A.1: A diagram of how power splits through the data logger (CR1000) and voltage regulator (AVRD) and then runs separately to the multiplexer and the tuned power junction, which each connect to the sensor cables.

A.2 Installation maps

The following are maps that describe the TDP deployments at Rivendell. The power cables carrying tuned voltage were all the same length, to create identical voltage drops over the cable length. The length of the data cables could vary.

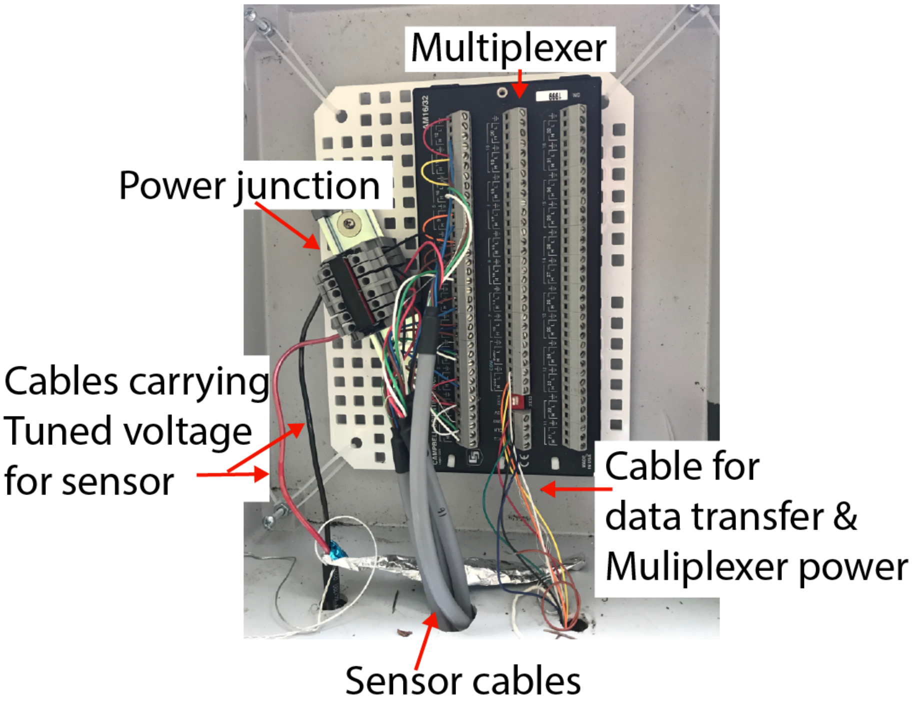

Figure A.2: A labeled diagram showing the arrangement of components in the environmental enclosures hung from the instrumented trees. When deployed, the enclosure holes were sealed.

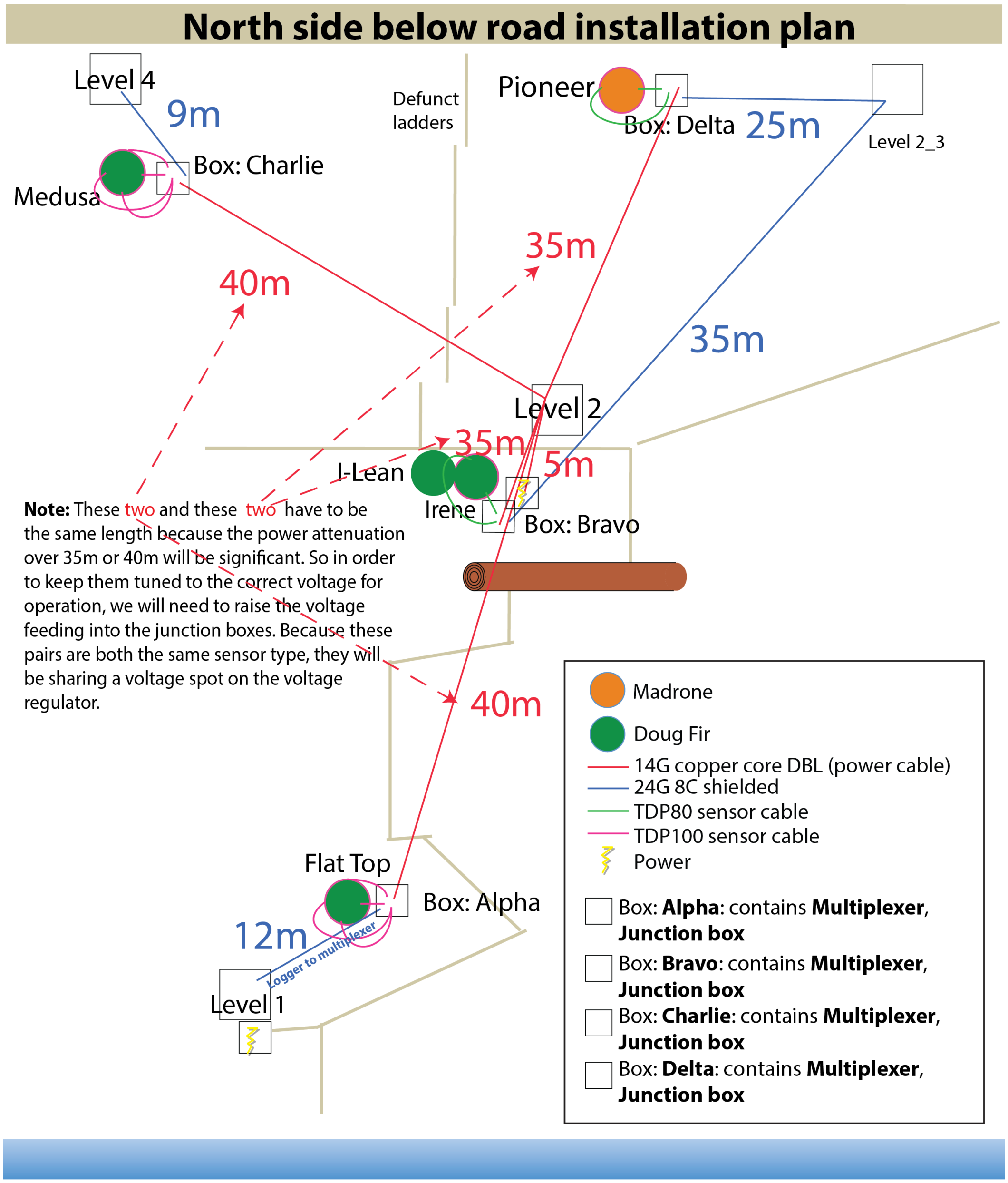

Note: These two and these two have to be the same length because the power attenuation over 35m or 40m will be significant. So in order to keep them tuned to the correct voltage for operation, we will need to raise the voltage feeding into the junction boxes. Because these pairs are both the same sensor type, they will be sharing a voltage spot on the voltage regulator.

Needed: 4 multiplexers; 4 terminal strip junctions; 1 voltage regulator, 2 voltage dividers, 4 weather tight enclosures and mounting gear, 2 power cables 40m, 2 power cables 35m, 1 power cable 5m, 1 24G8C cable each of 35m, 25m, 12m, and 9m, code modifications for Level 1_2, Level 4, and Level 2_3, and ~6W power from I-Lean.

Figure A.3: A schematic (not to scale) of the installation wiring for the north-slope trees occurring below Conger road, which bisects the north slope. Douglas fir tree 'Flat Top' did not generate data, due to trouble communicating with the Level 1 logger. Douglas fir tree 'Medusa' was not instrumented due to deeply scarring tree disease discovered beneath the bark.

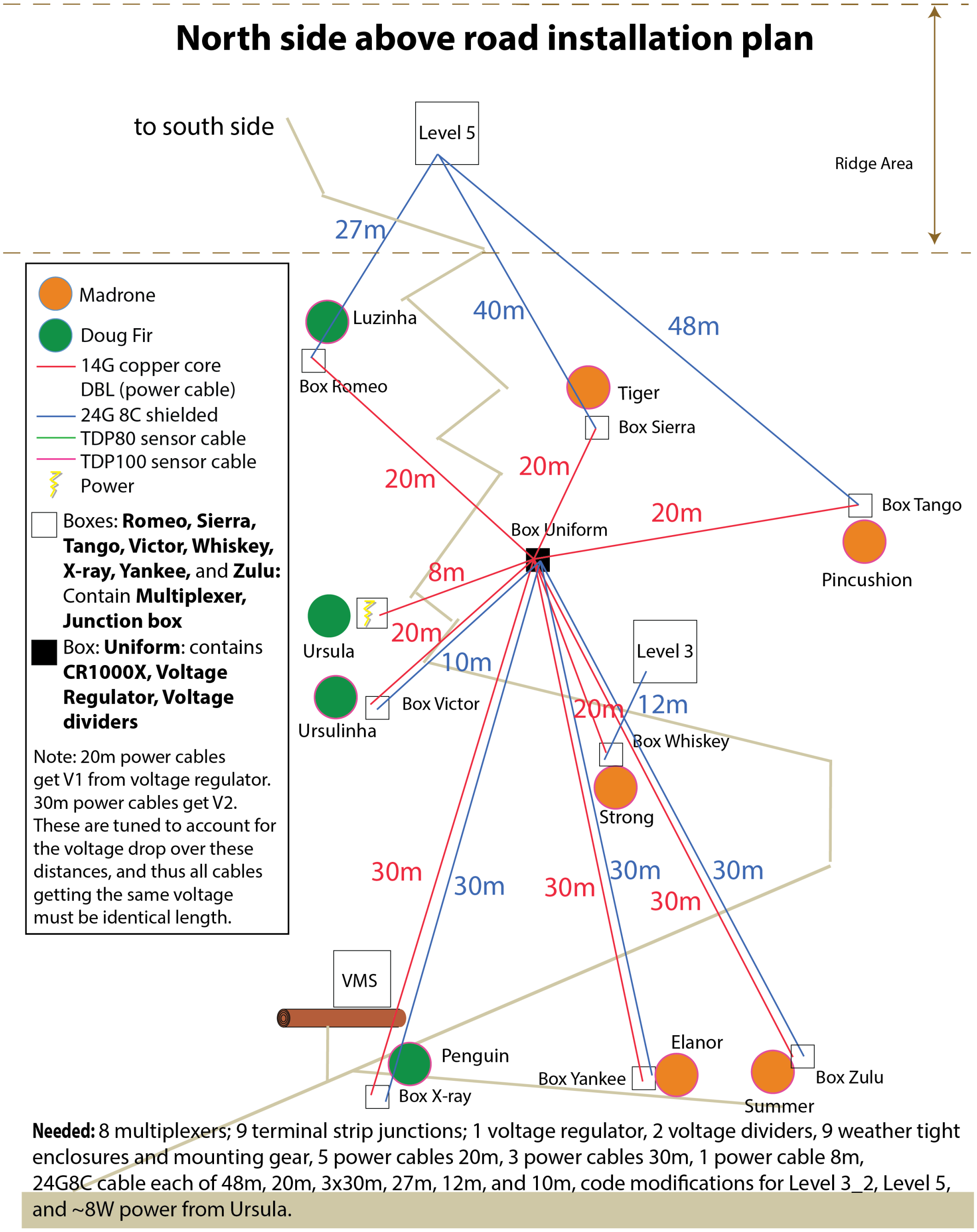

Boxes: Romeo, Sierra, Tango, Victor, Whiskey, X-ray, Yankee, and Zulu: Contain **Multiplexer, Junction box**

Box: **Uniform**: contains **CR1000X, Voltage Regulator, Voltage dividers**

Note: 20m power cables get V1 from voltage regulator. 30m power cables get V2. These are tuned to account for the voltage drop over these distances, and thus all cables getting the same voltage must be identical length.

Needed: 8 multiplexers; 9 terminal strip junctions; 1 voltage regulator, 2 voltage dividers, 9 weather tight enclosures and mounting gear, 5 power cables 20m, 3 power cables 30m, 1 power cable 8m, 24G8C cable each of 48m, 20m, 3x30m, 27m, 12m, and 10m, code modifications for Level 3_2, Level 5, and ~8W power from Ursula.

Figure A.4: A schematic (not to scale) of the installation wiring for the north-slope trees occurring above Conger road.

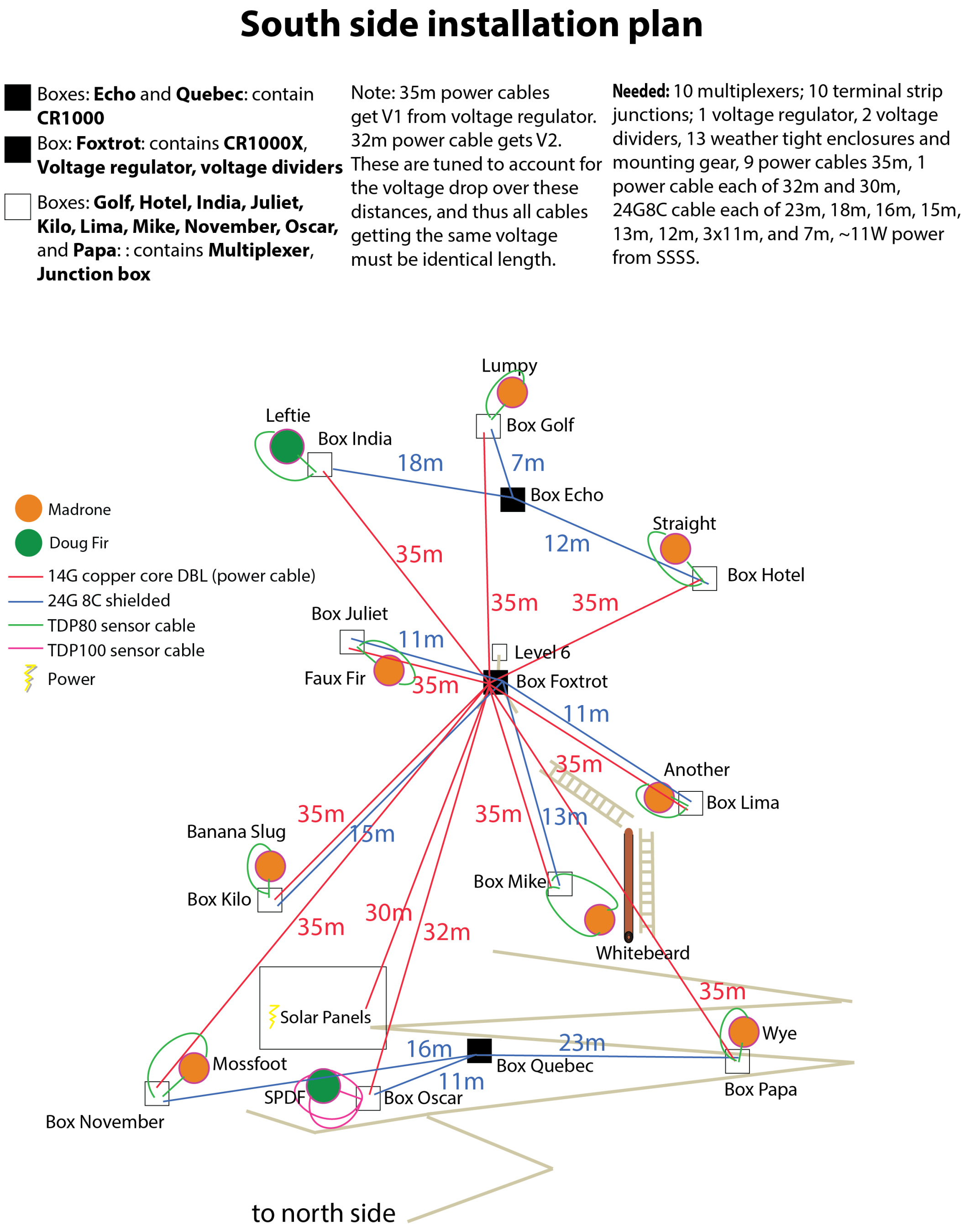

South side installation plan

■ Boxes: **Echo** and **Quebec**: contain **CR1000**

■ Box: **Foxtrot**: contains **CR1000X**, **Voltage regulator, voltage dividers**

☐ Boxes: **Golf, Hotel, India, Juliet, Kilo, Lima, Mike, November, Oscar,** and **Papa**: : contains **Multiplexer**, **Junction box**

Note: 35m power cables get V1 from voltage regulator. 32m power cable gets V2. These are tuned to account for the voltage drop over these distances, and thus all cables getting the same voltage must be identical length.

Needed: 10 multiplexers; 10 terminal strip junctions; 1 voltage regulator, 2 voltage dividers, 13 weather tight enclosures and mounting gear, 9 power cables 35m, 1 power cable each of 32m and 30m, 24G8C cable each of 23m, 18m, 16m, 15m, 13m, 12m, 3x11m, and 7m, ~11W power from SSSS.

Figure A.5: A schematic (not to scale) of the installation wiring for the trees occurring on the south slope.

Chapter 3

Preliminary sap flow analyses using TDP data

This chapter explores the preliminary analyses using the TDP sapflow and environmental data together. These analyses begin a quantitative discussion of Pacific madrone–Douglas fir comparisons and comparisons among individual madrones.

3.1 Regressions of madrone sap flow and VPD on Rivendell's South slope

3.1.1 Research aims

Chapter 2 documented a large degree of 15m-scale variability in shallow soil moisture (section 2.5.2.1) and no appreciable above ground variability in vapor pressure deficit (VPD). The South slope soil moisture ranged from under 10% Volumetric Water Content (VWC) (values shown by all but two sensors in dry, pre-rain conditions) to above 25% VWC. This range functionally spans conditions too dry to support any transpiration to non-moisture-limiting in a predictive sap velocity model for Pacific madrone [56, 55]. If surface soil moisture variability extends to similar variability in total root zone moisture, then under this model, that would imply substantial differences in water limitation status across the madrone individuals of the south slope.

Because VPD directly modulates transpiration flux day to day, we considered how a tree's sap flow response to changes in VPD could relate to that tree's water supply. We hypothesized that 1) trees growing under water-limited conditions would show reduced increases in sap flow in response to increases in VPD (shallower regression slope); 2) trees experiencing more dramatic seasonal changes in subsurface moisture availability– moving from non-limiting to limiting conditions– will show a weaker relationship between sap flow to VPD over the season (lower R^2); and finally 3) that both of these responses would track coherently with shallow soil moisture variation at 30 cm, proving a linkage between proximate shallow moisture conditions and whole-root-zone moisture. Upstream from these hypotheses is the simplifying assumption that within a single species all similarly-sized individuals, through optimizations of crown geometry, leaf area, and leaf angles, experience equivalent bulk canopy conductance; and that canopy conductance is never limited by persistent low light conditions during the summer season. These assumptions, if true, allow us to expect equivalent sap flow responses to VPD across individuals experiencing equivalent soil moisture conditions, which in turn allows us to attribute variable responses to VPD across individuals to different soil moisture conditions.

3.1.2 Methods

To test the hypothesis that trees growing under water-limited conditions would show a diminished sap flow response to variation in VPD, we ran linear regressions of daily integrated VPD against daily integrated sap velocity. To compute the integrals, we focused on the dry summer months to see the impact of steadily declining soil moisture. We discarded days with incomplete data before computing the integrals. Regressions were done on a sensor-by-sensor basis for the whole dry season, and also by month. All computations were performed with Python 3.8.5.

3.1.3 Results & Discussion

The results over the dry summer months (June-October) are shown in figure 3.1, while the results of the monthly regressions, alongside a map showing the locations of installation, are summarized in figure 3.2.

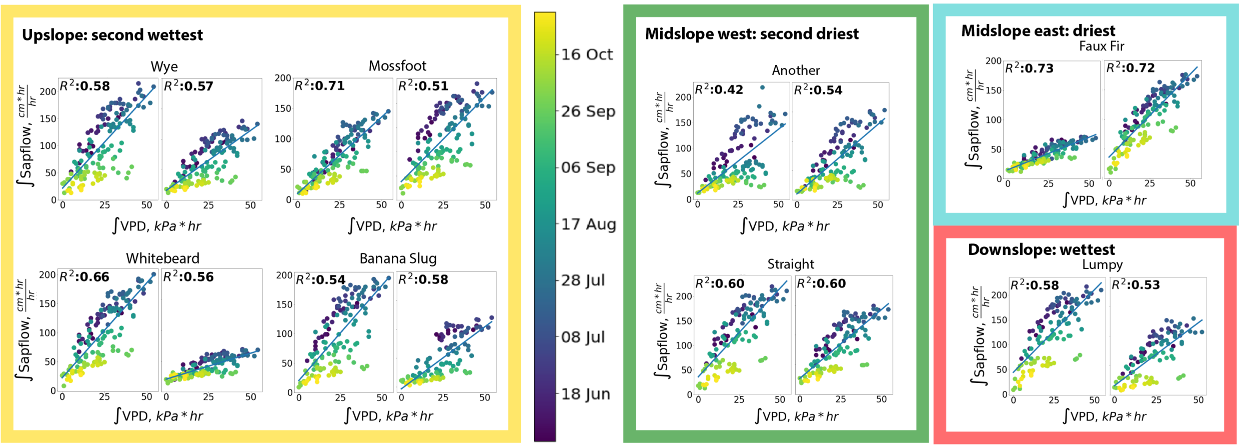

Figure 3.1: Sap velocity integrated over time yields a daily distance that water moves up the tree trunks at the point of observation, which serves as a proxy for daily transpiration. Here, daily integrated sap velocity is regressed against daily integrated VPD. Two panels per tree reflect two sensors per tree, and color indicates date. Slope steepness indicates the degree of sap flow response to VPD, while tightness of regression fit indicates the linear predictability of sap flow from VPD over the whole season. Variability in regression slope and overall fit does not follow variability in shallow soil moisture, and even within a single tree, the slope and regression fit varies by sensor, due to circumferentially varying sap flow dynamics.

Figure 3.1 shows a seasonal progression in regression slope. The wetter early summer (purple and blue dots) shows a steeper relationship between daily integrated sap flow and daily integrated VPD than the dry early fall (yellow dots), which may be attributable to evolving soil moisture availability, as VPD and solar radiation intensity evolve relatively little over the same time period. Interestingly, any variation in regression slope steepness, and in the predictability of the relationship between sap flow and VPD (R^2) did not follow the variation in surface soil moisture. In fact, the results show that large differences in regression slope and R^2 can exist between the two sensors on a single tree. This suggests that variance around the trunk in sap velocity, and consequently the variability in response of sap velocity to environmental drivers in different wood tissues existing around the trunk, are too large for the sap flow dynamics of an individual tree to be fully characterized with only

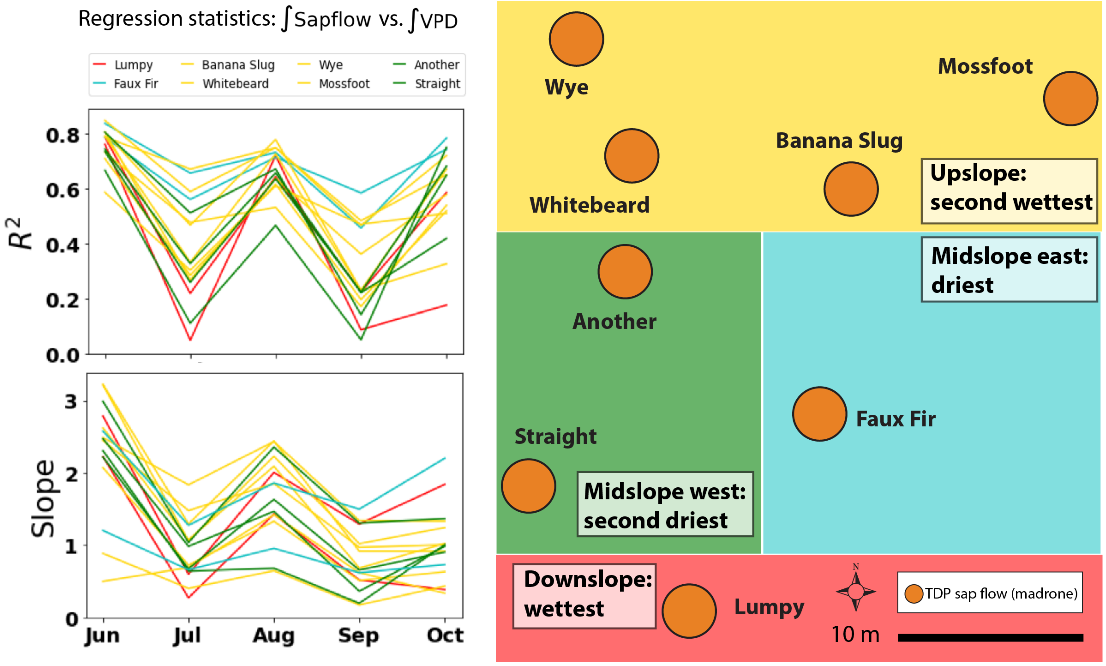

Figure 3.2: Daily integrated sap velocity was regressed against daily integrated VPD on a monthly basis, and the resulting statistics are summarized in the left two panels while on the right, a map shows how the madrone trees instrumented with TDP sensors align with the color-coded regions of soil moisture differences. The top left panel shows the seasonal evolution of R^2 values, while the bottom panel shows the seasonal evolution of the regression slope. Each line represents one sensor, with the colors coded to match the soil moisture region hosting the instrumented tree.

two sensors per tree.

The monthly changes in regression statistics are visually summarized in figure 3.2 so that the color of the lines match the soil moisture region hosting the sensor. None of the months show a ranking of R^2 or regression slope that coheres with the variation in surface soil moisture. The months of July and September stand out as having particularly weak correlations between VPD and sap velocity, as well as particularly shallow regression slopes. We interpret this as indicating the presence of other factors playing a larger role in controlling sap velocity variability during these months. In the month of July shallow regression slopes and low R^2 are partly explained by consistently high

VPD conditions, which led to other factors controlling the bulk of sap flux variability. In September, daily VPD conditions varied greatly while the sap flux response to equivalent VPD conditions diminished as the month progressed. We hypothesize that this is the impact of declining soil moisture across the site. The comparative uptick in both regression slope and R^2 in the month of October could be explained by the rainstorm at the start of the month coupled with low VPD conditions throughout the month changing the economics from supply limitation (soil moisture) to demand limitation (VPD).

Phenological events in both July and September may also be shaping the regression results. Despite being evergreen, madrone trees experience an annual leaf turnover with a temporary double canopy in July as the new leaves flush before the old leaves drop. Evolving leaf surface area over the month could create changing relationships between VPD and sap flow throughout the month, muddying the relationship between VPD and sap flow. In September, madrone trees are fruiting, which may create a reproductive demand for water beyond that needed for photosynthesis and transpiration. We do not know of any research that has documented the impact of these phenological stages on water usage in madrone.

In light of declining soil moisture over the same time period (see figure 2.14), the seasonal progression in regression slope shown in figures 3.1 and 3.2 supports our first hypothesis that reduced soil moisture conditions lead to a smaller sap velocity responses to VPD. However, the variation in regression slope among sensors stationed on the same tree show that natural variation in wood tissues across installation sites has the potential to impact regression slope and its degree of seasonal evolution beyond soil moisture conditions alone. Furthermore the exceptionally low regression slopes of July indicate that the context of the relationship between sap velocity and VPD is complicated by observational conditions and potentially phenological factors. Hypothesis 2, which states that larger seasonal variability in subsurface water resources will impact R^2 values, was not proved. Based on the evidence available, our third hypothesis fails, suggesting that deeper moisture reserves accessed by trees are not governed by the spatial patterns of variation that are observed in surface soil moisture. Because of this, we aren't able to determine which trees experience greater changes in their total root zone moisture over the seasons. This leaves us unable to fully test hypothesis 2.

The relevance of our simplifying assumption of equivalent bulk canopy conductance among similarly-sized individuals is called into question by the variability between two sensors mounted on a single tree. Variation in sap flow dynamics on two different sides of the same tree imply that either perceived canopy conductance downstream from the sensor either varies circumferentially around a tree, with xylem conduits connecting to different canopy regions; or, that variation in wood properties around the tree makes equivalent downstream canopy conductance result in different rates of sap flow around a trunk. Either explanation would indicate that two installation sites can not be directly compared without more contextual data of wood type, or studies of crown illumination.

3.1.4 Conclusions

Regressions of integrated daily VPD against integrated daily sap flux over variable regions of surface soil moisture lead to several conclusions:

1) Sap flow dynamics do not respond to surface soil moisture in a manner consistent with their total root zone moisture experiencing similar spatial patterns. This suggests that either root networks laterally subtend these zones of moisture or deeper moisture reserves are differently spatially distributed.

2) Sap flow speed and response to VPD are not consistent across sites within an individual tree.

Conclusion 1 led us to consider area-averaged surface soil moisture as an ordinal proxy (magnitude agnostic) for deeper soil moisture reserves experienced by trees on both slopes. Conclusion 2 led us to move forward in our analysis with population-averaged sap flows, so that variation between sites and individuals could be averaged out among a larger number of sensors to characterize the population.

3.2 Comparison of sap flow in Douglas firs and Pacific madrones on Rivendell's north slope

3.2.1 Research aims and methods

In this section, we explore species differences in water flux dynamics and seasonality in the sort of quantitative framing that had not been feasible with the Keck Hydrowatch HRM data.

Over the span of two years of TDP sap flow data, for each species we analyzed the seasonal timing of maximum sap velocities and documented daily integrated sap flux. This analysis was limited to north slope trees because number of Douglas firs on the south slope was too small to support a comparison with neighboring south slope madrones. To prepare the data for the daily maxima and the daily integrated sap flux computations, we computed population averages by species for the north slope, discarded days with data gaps remaining, and then derived daily maxima or integrals from the population averages over the complete days that remained.

For time spans selected from the first year of data, we also used empirical orthogonal function (EOF) analysis to find distinctive features in the shape of the diurnal cycles and seasonal progression of sap flow characteristic of each species. For this analysis, data from both slopes was used. To prepare the data for the EOFs, we aggregated all data streams for both slopes and both species into a matrix, and then selectively reduced the data by row (time stamp) or column (sensor ID) to a set of observations that contained no missing values that are not shared among all sensors. The remaining data set has discontinuities in time, but no NaN values. While reducing the data, we optimized for including more unique data streams, at the expense of introducing more gaps in time. Ultimately, EOFs were performed over a set of 36 sensors on 19 trees, focusing on two different time spans: both for a long span of the 2018-2019 sap flow year, and for a single sunny day in July 2018. All computations were performed in Python 3.8.5.

3.2.2 Results

3.2.2.1 Daily sap velocity maxima and integrated sap flux:

The seasonal progression of daily sap velocity maxima in Pacific madrone and Douglas fir shown in figure 3.3 confirms the species differences in the timing of peak sap velocity described in Link 2014. Annual peak sap velocities in Doug fir occur up to three months before those in Pacific madrone, and during the driest summer months, their daily maxima peak at significantly slower velocities.

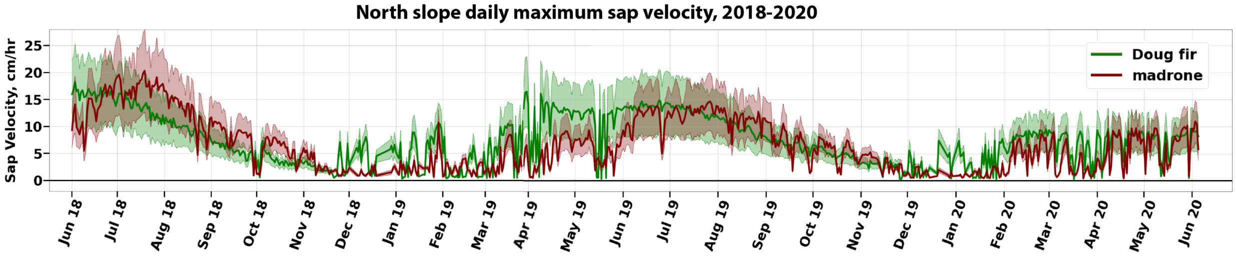

Figure 3.3: Average daily maximum sap velocity for Douglas firs and Pacific madrones on the north slope is plotted for two years, with the population standard deviation shown by the shade. Averages are derived from all reporting sensors on 6 madrones and 4 doug firs. The number of sensors feeding into the average per species varied from 4 to 10 as data streams cut in and out under field conditions. Near the winter solstice in both years, power deficits caused gaps in the data, which have been interpolated as straight lines.

Though Douglas firs display slower maximum sap velocities over the dry summer, time integration of their diurnal cycle of sap velocity (plotted in figure 3.4) shows that they nevertheless continue to move a greater or equal amount of water per sapwood area as their madrone neighbors. This is because they have a longer daily span of sunlight due to their tall stature. Intriguingly, the two species show remarkable agreement on the daily rate of water flux through their respective sapwood areas during the driest months, despite operating at different speeds throughout that period.

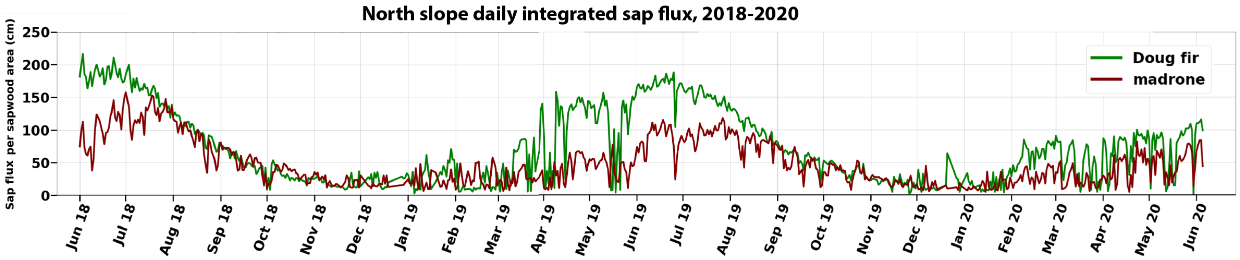

Figure 3.4: Daily integrated sap flux per sapwood area plotted for Douglas firs and Pacific madrones on the north slope, based on the population mean sap velocity for each species. The magnitude of Douglas fir sap flux is greater than that of madrone even at similar sap velocities (see figure 3.3) because their crowns remain illuminated for longer due to being taller.

3.2.2.2 EOFs:

The first three principal components for each EOF analysis are shown in figure 3.5. Both analyses show separation of species and slope aspect in principal components 2 (PC2) and 3 (PC3), respectively. The shape of the principal components for the analysis of a single day (figure 3.5 panel a, left column) shows that the separation in positive or negative weights for that principal component (figure 3.5 panel a, right column) is, in the case of PC2, due to the length of the diurnal cycle of sap flow. This confirms that Douglas firs experience a longer daily cycle with a slower peak flow compared to madrone. The exceptions to this pattern are trees in low-elevation positions on both the north and south slopes, where the duration of solar radiation received is most impacted by the effect neighbor-shading. The shape of PC3 in the daily analysis shows that the south slope trees have a daily cycle of sap flow that is time-shifted relative to their north neighbors. In this case, the exceptions occur on the extreme western edge of the north slope (Summer) or eastern edge of the south slope (Faux fir), which is likely to correspond to different crown orientation than other trees in their slope cohort.

The EOF analysis of the longer span of data shows a slightly greater degree of separation by species and slope, with differences in individual daily cycles compounded by differences in seasonal progression of daily cycles.

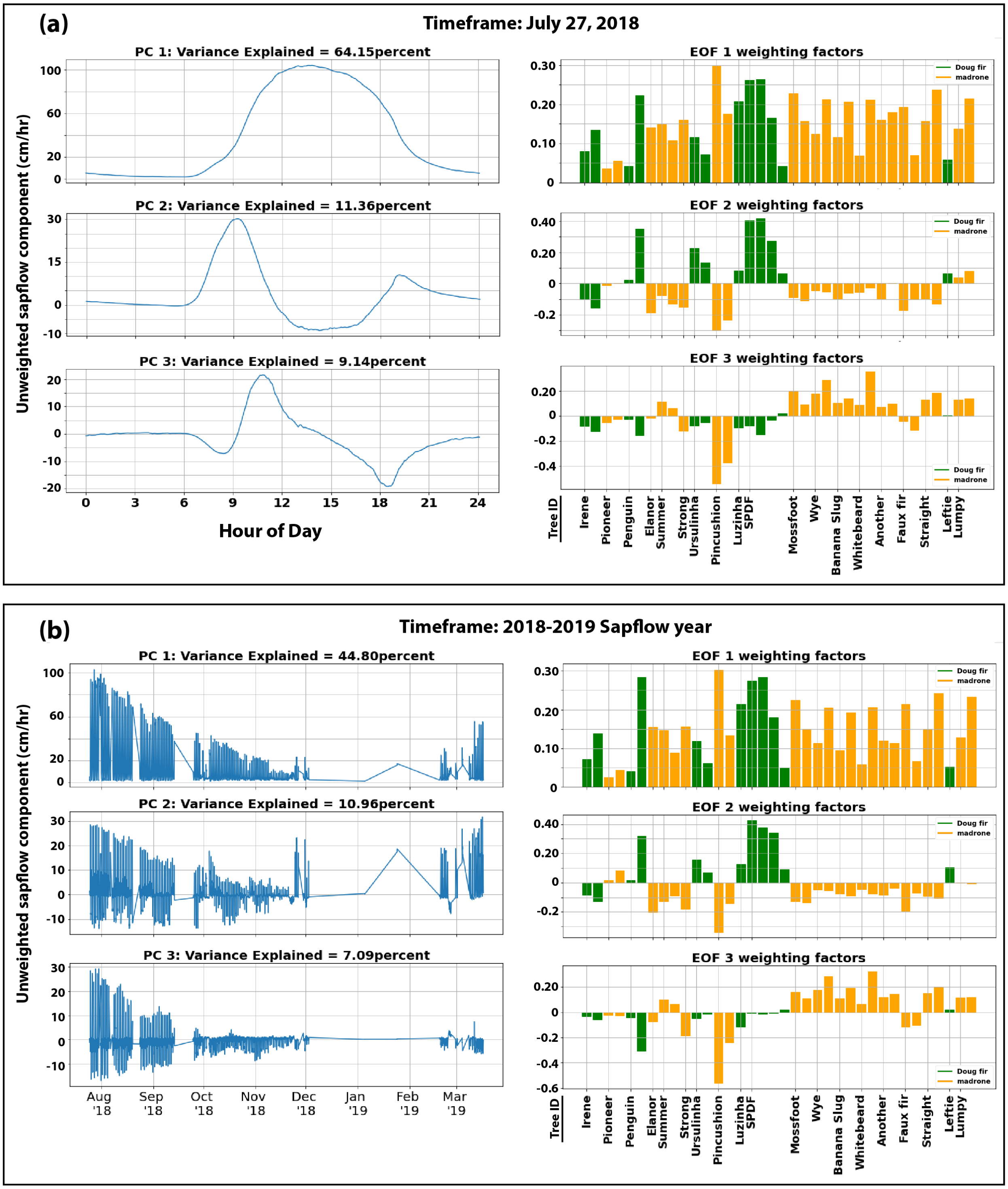

Figure 3.5: See next page for caption.

Figure 3.5: (on previous page) EOFs were performed for over a typical sunny day in late July (panel (a)) and a longer span of 2018-2019 (panel (b)). For each time span, the first three principal components are plotted in the left panels, with weighting factors color coded by species given in the right hand panels. The weighting factors are organized left-to-right in order of the sensor's slope position, from low-elevation trees on the north slope to low-elevation trees on the south slope.

3.2.3 Conclusions

With the new TDP data set, we were able to expand the documentation of species differences in water flux dynamics and seasonality between Pacific madrone and Douglas fir. Our findings are summarized below:

1) We confirmed the seasonal offset in annual peak sap velocities between these two species, noted in [55].

2) We further found that, due to species differences in crown height and shape, and hence differences in experienced day length, the differences in annual peak sap velocity did not correspond to differences in transpiration flux. We found that generally Douglas firs displayed greater or equal transpiration fluxes per unit of sapwood area compared to Pacific madrones, even during the driest part of the summer. When considering that mature Douglas firs are a larger size class of tree than mature Pacific madrones, with correspondingly greater sapwood area, we conjecture that the net water flux from Douglas firs individuals greatly outstrips that of their Pacific madrone neighbors, no matter the season.

3) We found that differences in timing and duration of crown illumination best explained the species and slope-aspect separation highlighted in the EOF analysis. This suggests possible avenues for inferring crown geometry or orientation from sap velocity signals.

Findings 2 and 3 were made possible by the new TDP platform.

Chapter 4

Direct observations of microclimatic and water flux differences

4.1 Introduction

Slope aspect influences microclimate directly via insolation differences, and this effect varies depending on latitude and slope gradient. Our aim is to understand how, and to what extent, microclimates caused by topography are associated with variations in tree transpiration. To do this, we embarked on a study at the University of California's Angelo Coast Range Reserve in Northern California, a site which is now NSF's Eel River Critical Zone Observatory. The focus is the temporal and cross-slope variations of sap velocities of a population of Pacific madrone trees (*Arbutus menziesii*)– a deeply rooted, drought-tolerant, broadleaf evergreen tree– straddling a microclimate gradient created by differences in solar radiation on adjacent north- and south-facing slopes of a hill. We hypothesize that slope aspect in the mid-latitudes influences microclimate and hence tree transpiration, leading to cross-slope differences in both the timing and amount of vegetation water fluxes. For simplicity, we focus only on data from the dry summer. We define microclimate by ambient air temperature and humidity beneath the canopy, incoming solar radiation adjusted for the slope and aspect of the closed canopy, and soil moisture measured at 30 cm.

In this chapter, which includes material previously published in [8], we describe the research site and we present field observations documenting the microclimatic differences across the hill slope divide, and analyze the differences in transpiration from the populations of Pacific madrones living on each hill slope.

4.2 Methods

4.2.1 Site description

Our study took place at the University of California's Angelo Coast Range Reserve (39.729N, -123.644W), a site with large variation in year-to-year precipitation (e.g., 1027 mm in 2013-14, 2991 mm in 2016-17), and hosting a heavily instrumented, steep, forested north-facing slope. The forest is composed of mixed broadleaf and needleleaf evergreen trees typical of the Douglas fir Pacific alliance [86].

Our installations took the observations to the opposing south slope. Because of the near-direct north–south orientation of the hillslopes, the microclimatic differences between the two slopes are pronounced. Our observations show that the south slope can be nearly 7°C hotter and experience VPDs up to 1.8 kPa greater during late September mornings (see Table 4.1). There is a visible transition in tree species composition across the ridge of the hill (see Figure 4.1). Because the instruments deployed across the two sides of the hill and adjacent meadow are less than 400 m apart, we assumed precipitation inputs and cloud-induced variations in solar radiation are identical for the meadow and both sides of the hill. Soil samples taken near the surface and rock cores extracted from deeply drilled wells confirmed that soil type and underlying lithology are comparable on both sides of the hill.

4.2.2 Instrumentation

The field program collected 1) sap velocity measurements on Pacific madrone trees; 2) ambient understory temperature and humidity microclimate; 3) incoming solar radiation to an open meadow adjacent to the site; and 4) soil moisture at 30 cm (Figure 4.1).

Sap velocity sensors (Dynamax Granier-style Thermal Dissipation Probes, as in [35] and [34]) were installed into 14 madrone trees, 8 on the south slope and 6 on the north slope (Figure 4.1, red dots). Our study trees ranged from 36

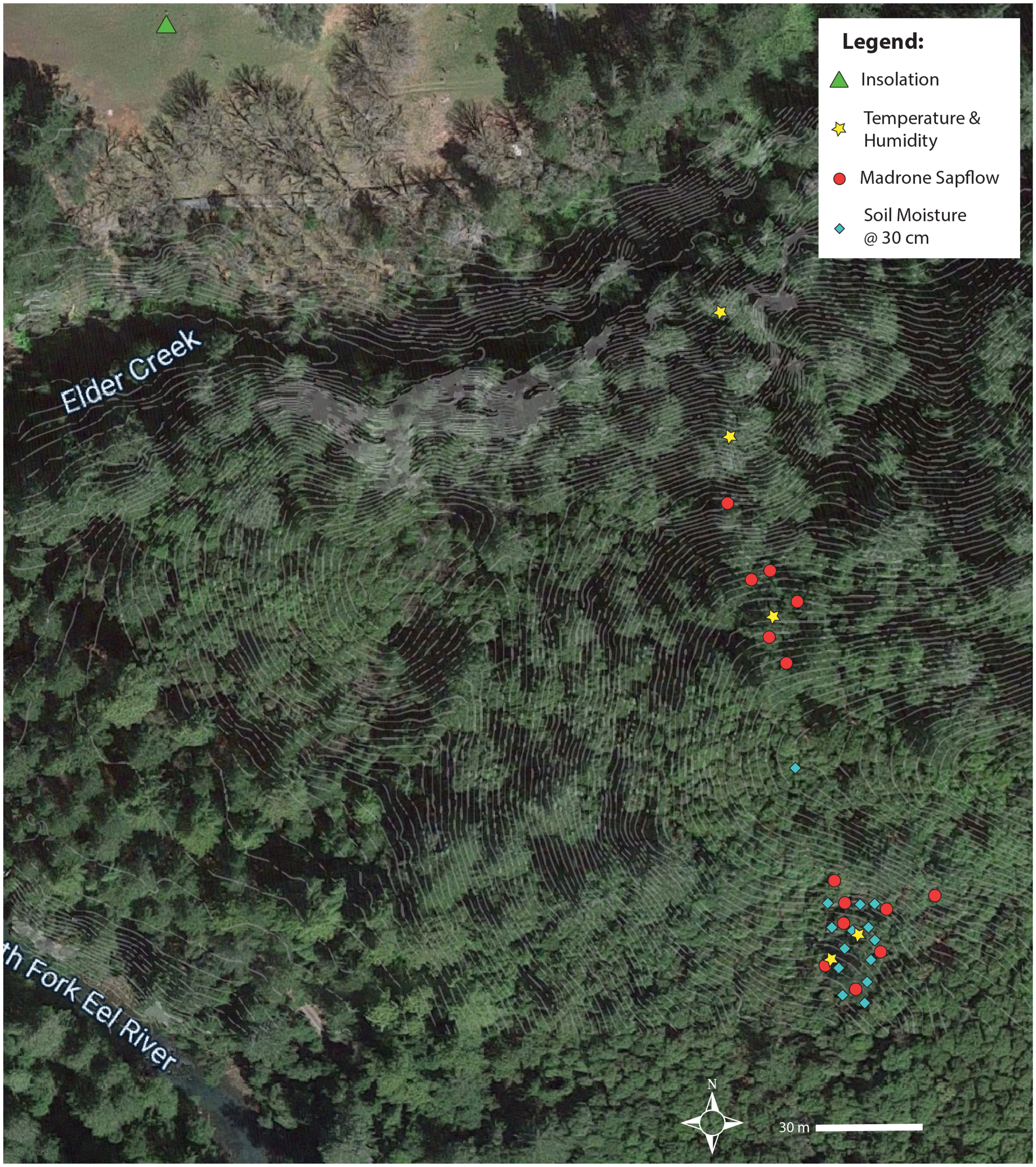

Figure 4.1: See next page for caption.

to 72 cm in diameter, and each tree hosted two 80-mm-long sensors (each with thermocouple junctions at 15 and 70 mm) placed approximately 180°apart. In

Figure 4.1: (on previous page) A map of the study site in Northern California (39.729°N, 123.644°W), and the locations of data for this analysis. The canopy covering the north slope is largely made up of Douglas fir (*Pseudotsuga menziesii*), bay (*Umbellularia californica*), and evergreen oak tree species (Tan oak *Notholithocarpus densiflorus*, Coastal live oak *Quercus agrifolia*, Canyon live oak *Quercus chrysolepis*), with some Pacific madrone trees (*Arbutus menziesii*) in the upper half of the hillslope. In contrast, the south slope is mostly populated with Pacific madrone trees, with a few Douglas fir and oak trees primarily occurring in the upper half of the slope near the ridge. One-meter topographic lines are shown in light gray. Underlying high-resolution satellite imagery is from Maxar Technologies, accessed through Google Earth Engine [33].

this analysis, we considered only data from the outer thermocouple junctions, at 15 mm depth. This resulted in 16 and 12 data streams on the south and north slopes, respectively.

Sixteen soil moisture sensors (Campbell Scientific CS650) monitored surface soil moisture at 30 cm in a network that covered the south slope and ridge area (Figure 4.1, blue diamonds). Unfortunately, similar soil moisture observations on the north slope were compromised during the study period, and were therefore not used in this study. Three temperature and humidity sensors (Campbell Scientific CS215) were installed 1.5 m above the ground in weather stations on the north slope, while eleven existed on the south slope, ten of which hung in a vertical string from the canopy to the ground, and the last of which was installed 1.5 m above the ground in a weather station (Figure 4.1, yellow stars; vertical string represented as one point). A weather station in an adjoining meadow provided information about incoming radiation, wind speeds, and precipitation (Figure 4.1, green triangle).

4.2.3 Data processing

All data were collected at 1–15-minute intervals and resampled to 5 minute intervals with no interpolation. Cleaning and analysis of field data was conducted with Python 3.7.4. All data and scripts for processing are available for download [7].

Sap velocity: We processed our sap flow data according to the methods described in detail in section 2.4 of chapter 2. In sum, we began by applying a standard zeroing procedure to each data stream [89] using a 5-day window. Then, after excluding outliers (one data stream on the north slope), all remaining data streams were averaged together by slope, resulting in a sap velocity time series for an average north-slope madrone tree and an average south-slope madrone tree. We interpret the standard deviation of our average-tree data streams as representing total uncertainty in our measured sap velocity magnitude (see figure 4.2).

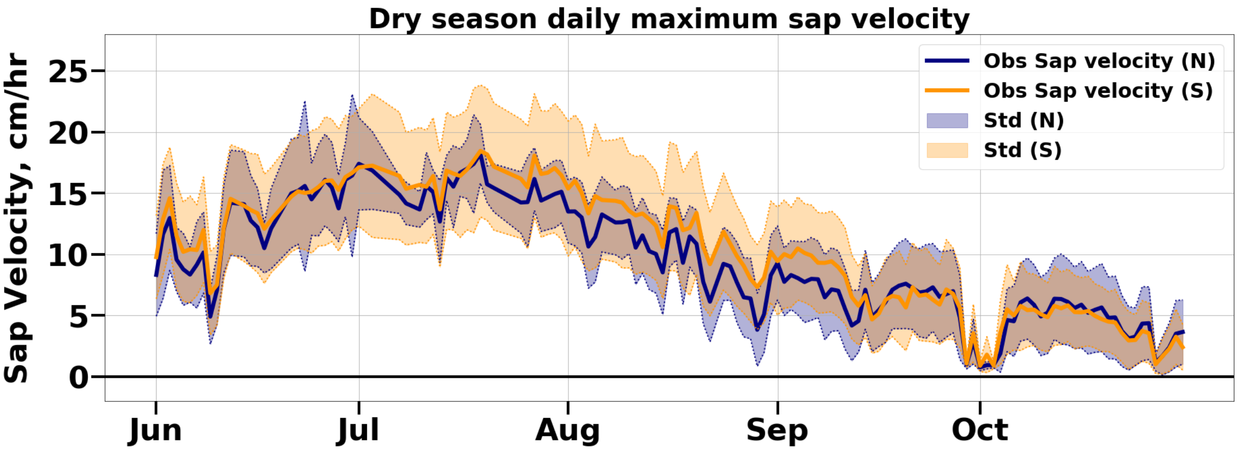

Figure 4.2: Daily maximum sap velocities averaged (μ) for each slope, plotted with +/-1 standard deviation (σ) reflecting spread among the data streams for each slope's tree population. The coefficient of variation ($CV = \frac{\sigma_t}{\mu_t}$, where t=time) for sap velocities on the north slope ranges from 9.5% in mid-July, to 91.0% in mid-October. The larger south slope population exhibited slightly wider spread in sap velocities on average; CV for the south slope ranges from 25.9% in mid-September to 86.0% in mid-October. The south slope has faster peak velocities on average throughout most of the dry season up to the middle of September, yet during the end of the dry season the north slope experiences faster peak sap velocities on average. Nevertheless, as Figure 4.6 shows, the south slope transpires more water per sapwood area even during the month of October due to a longer diurnal cycle of transpiration.

VPD: Temperature and humidity were both reported by a single type of instrument (Campbell Scientific CS215, Figure 4.1, yellow stars). We averaged temperature and humidity data streams by slope and then derived vapor pressure deficit (VPD) as:

$$\mathrm{VPD} = \mathrm{SVP}(1 - \mathrm{RH}) \tag{4.1}$$

where SVP is the saturated vapor pressure (kPa) estimated as a function of temperature by the Clausius–Clapeyron equation [11], and RH is the relative humidity.

4.2.3.1 Insolation:

Unobstructed total (combined direct and diffuse) solar radiation is measured in an adjacent meadow (LI-COR LI200X-L, Figure 4.1, green triangle). Scaling sunlight for each slope's environment from the meadow sensor is a key underlying feature of our analysis. To do this, we scaled measured total solar radiation by a theoretically-derived factor representing the relative proportion of direct-beam radiation received by each slope, based on their unique geometry. This approach is an approximation, as it does not account for the fact that the diffuse fraction of total radiation incident upon the slopes depends not on geometry, but rather on the sky view angle (i.e. horizons generated by neighboring hills) of each slope. The diffuse fraction is high under cloudy skies and at low sun angles. During our study period, clouds and fog were rare, and sap velocities were low at dawn and dusk, so the omission of partitioning and separately scaling diffuse radiation for each slope should not impact the bulk of our analysis.

To derive the sunlight scaling factor for each slope, we used: 1) slope aspect, derived from topographic maps, based on the average aspect of each sampled tree's location (the south slope's aspect is 189.1°, where 180° is due south, and the north slope's aspect is 344.2°, where 360° is due north); and 2) the canopy slope, derived from 12 LiDAR cross-sections of the vegetation (e.g. [53]) on each slope (the south slope's canopy has a slope of 21.97°, while the north slope is steeper, with a canopy slope of 32.82°). We then computed idealized clear-sky direct-beam solar radiation for different times and days (solar zenith and azimuth angles) using Python's 'solarradiation' library [81], which follows the formulation of [24].

The calculation runs as follows: At a time given by day of year n and hour of day $thour$, the incident beam insolation on a horizontal surface S_{flat} at latitude lat (degrees) and 0 degree longitude, is:

$$S_{\text{flat}} = SC \times (1 + 0.033 \times \cos(360/365)) \times \cos\theta_z, \tag{4.2}$$

where

$$\delta = 23.45 \times \sin\left(360\frac{284+n}{365}\right), \tag{4.3}$$

$$\omega = (thour - 12)/15 \times d2r, \tag{4.4}$$

$$\phi = lat \times d2r, \tag{4.5}$$

$$\cos\theta_z = \cos\phi\ \cos\delta\ \cos\omega\ +\ \sin\phi\ \sin\delta \tag{4.6}$$

$$\tag{4.7}$$

and $SC = 1361$ W/m^2 is the solar constant, and $d2r = \pi/180$ converts degrees to radians. δ is declination; ω is the hour angle; θ_z is the zenith angle.

The ratio R_b between the direct-beam on horizontal and hilly surface with *slope* (in degrees) and *aspect* (clockwise from North in degrees) is:

$$R_b = \frac{\cos\theta}{\cos\theta_z}, \tag{4.8}$$

where

$$\begin{aligned}\cos\theta = {} & \sin\delta\ \sin\phi\ \cos\beta - \sin\delta\ \cos\phi\ \sin\beta\ \cos\gamma + \cos\delta\ \cos\phi\ \cos\beta\ \cos\omega \\ & + \cos\delta\ \sin\phi\ \sin\beta\ \cos\gamma\ \cos\omega + \cos\delta\ \sin\beta\ \sin\gamma\ \sin\omega\end{aligned} \tag{4.9}$$

and $\beta = slope \times d2r$, $\gamma = (aspect - 180) \times d2r$ is the azimuth angle of the sloped surface, and θ is the angle between the incident beam and the normal to the sloped surface. The terms S_{N} and S_{S} that appear in equation 4.10 below are $S_{\text{flat}} \times R_b$, with R_b tailored to the geometry of each respective hill slope.

This calculation was done for a flat surface (S_{flat}) as well as for north and south slopes (S_{N} and S_{S}, respectively), using the latitude, canopy slope steepness, and slope aspect estimated for each slope. Then, to obtain the approximate total insolation for each slope, we scaled the total radiation measured at the meadow by the scaling factor for each slope:

$$I_{\mathrm{N}} = I_{\mathrm{meadow,\,observed}} \times \frac{S_{\mathrm{N}}}{S_{\mathrm{flat}}} \tag{4.10}$$

$$I_{\mathrm{S}} = I_{\mathrm{meadow,\,observed}} \times \frac{S_{\mathrm{S}}}{S_{\mathrm{flat}}} \tag{4.11}$$

Figure 4.3 provides a visualization of the computed solar trajectories for our study site and the scaling factors based on direct-beam radiation for each slope. The relative angles of the hillslopes and solar trajectories illustrate why it is that early in the dry season, the north slope receives more afternoon sunlight than the south slope, and late in the dry season, the north slope gets very little direct sunlight at all. Late in the dry season, the south slope receives more sunlight than the flat meadow, while the north slope receives less.

4.2.3.2 Soil Moisture:

Our dense network of 14 soil moisture sensors at 30 cm (CS650 Water Content Reflectometers, Figure 4.1, blue diamonds) shows large-magnitude variation in soil volumetric water content at a roughly 15 m length scale, independently confirmed by manual soil sampling (see more detailed discussion in section 2.5.2.1 of chapter 2). Analyses of soil texture and soil water retention conducted by another team working at this site show that there are no significant differences between the two slopes in these variables, rendering the relationship between soil volumetric water content and water freely available to tree roots comparable in the shallow soil layers of both slopes (D. Rempe, personal communication). This variation in shallow soil moisture is spatially organized, and appears to relate to the geomorphology and history of shallow landslide disturbance in the area (W. Dietrich, personal communication). The variation is not correlated with variation in sap velocity magnitude of proximate trees, suggesting lateral and vertical extents of the tree roots may be accessing moisture from a wider area and from deep moisture in weathered bedrock, in line with previous findings at this site [74, 87]. Unable to observe these deep moisture reservoirs, we used observations of water table dynamics from 16 wells on both slopes to understand that, once the rains cease, the overall dynamics of root-zone moisture are closely correlated with those of 30-cm soil moisture over

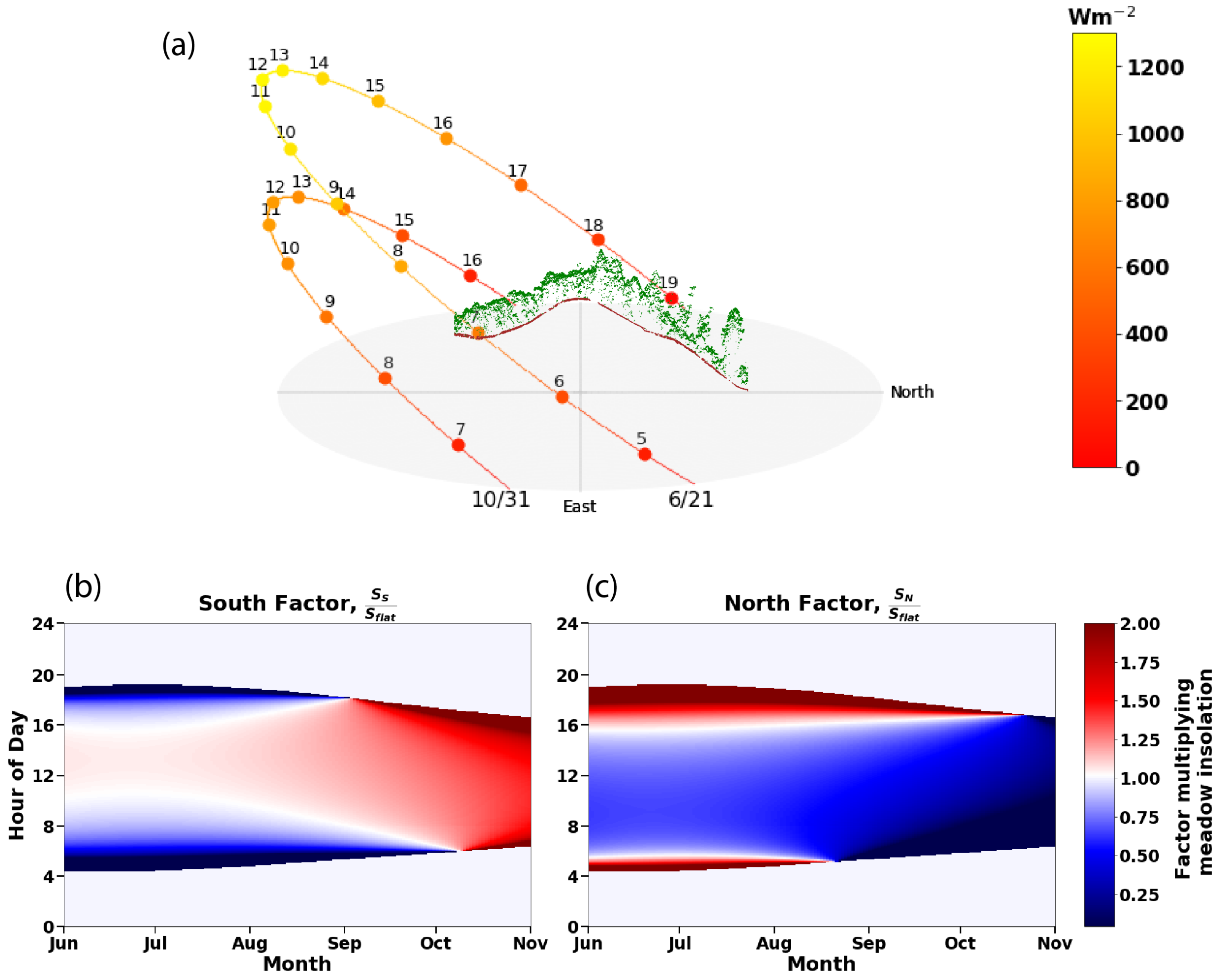

Figure 4.3: See next page for caption.

the summer dry season (i.e., both show a steady decline). We thus consider an area-averaged 30-cm soil moisture to be a loose proxy for deep root zone moisture on the both slopes.

4.2.3.3 VPD:

Temperature and humidity were both reported by a single type of instrument (Campbell Scientific CS215, Figure 4.1, yellow stars). We averaged temperature and humidity data streams by slope and then derived vapor pressure

Figure 4.3: (on previous page) A summary of the solar model. Panel a: The solar trajectories at the latitude of the study site for the summer solstice (6/21) and the end of the dry season (10/31), showing that the sun rises and sets north of due East and due West for part of the dry season. The numbers indicate local time. A LiDAR cross section of the Rivendell site is provided for orientation. Panels b) and c): the scaling factor derived for each slope's direct-beam insolation relative to the meadow's direct-beam insolation, as it evolves throughout the day (y-axis) and the dry season (x-axis). The asymmetry in panels b) and c) reflects the slightly westward aspect of both slopes, also visible in Figure 4.1.

deficit (VPD) as:

$$\mathrm{VPD} = \mathrm{SVP}(1 - \mathrm{RH}) \tag{4.12}$$

where SVP is the saturated vapor pressure (kPa) estimated as a function of temperature by the Clausius–Clapeyron equation [11], and RH is the relative humidity.

4.3 Results & Discussion

4.3.1 Microclimate and sap velocity time series on the north and south slopes

The observations cover the dry season (June–October) of 2018 and include sensor-averaged VPD and sap velocities for the north and south slopes, as well as soil moisture for the south slope. While soil moisture declines through the dry summer, sap velocities on both slopes peak in July when 30-cm soil moisture is ∼10%, about 1-2 months after the start of the dry season. The north-slope insolation declines as the summer progresses into early autumn, while insolation on the south slope remains approximately constant. VPD on both slopes fluctuates, depending on whether winds are on-shore or off-shore, but shows no seasonal trend (Figure 4.4).

Table 4.1 provides another view of the evolving climate over the dry season months, looking at both the time series maxima and the climatological maxima.

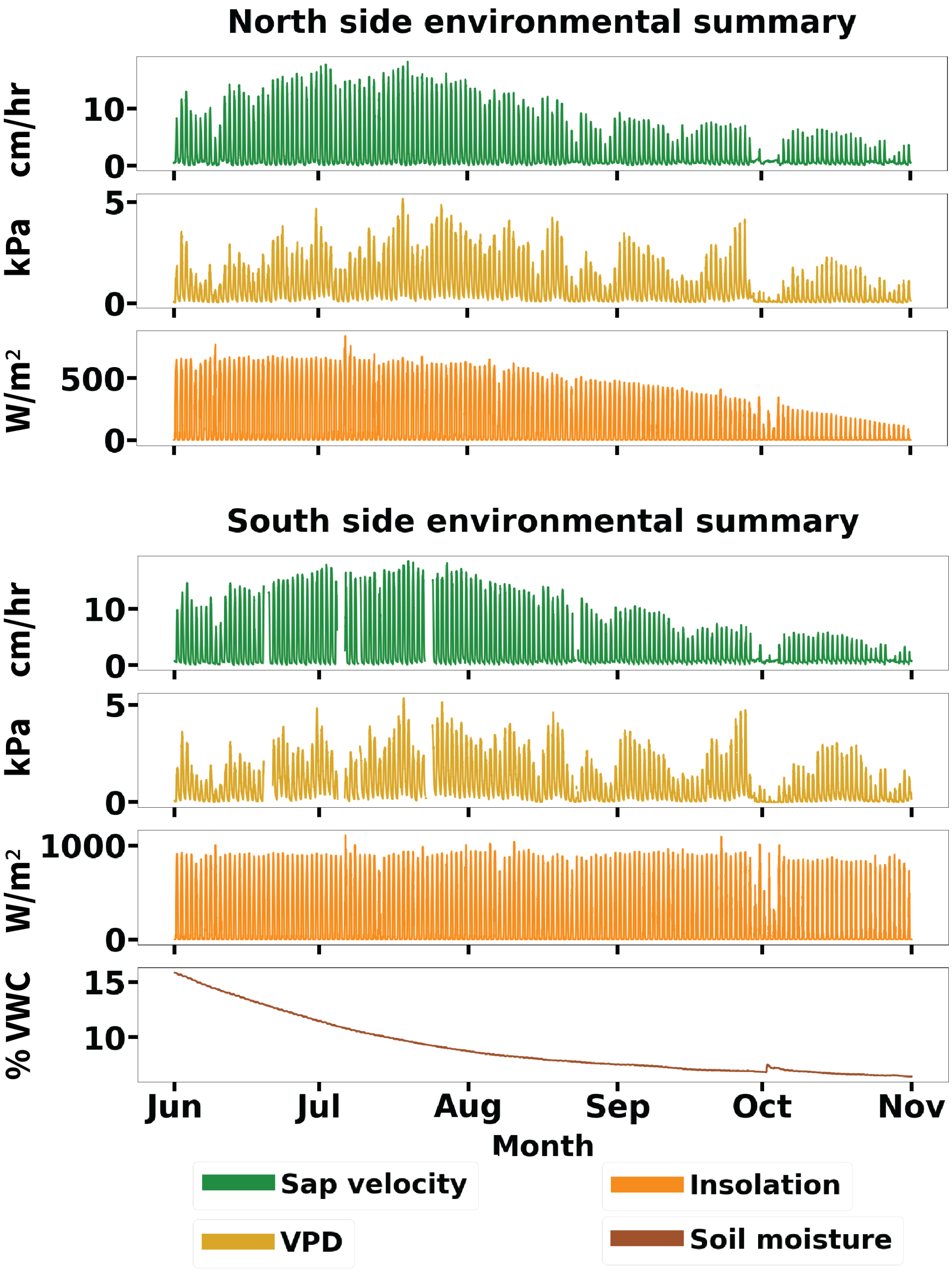

Figure 4.4: See next page for caption.

The climatological maxima correspond with the climatologies shown in Figure

Figure 4.4: (on previous page) Time series of environmental drivers of sap velocity for each slope. While soil moisture shows a steady decline through the dry summer, sap velocities on both slopes peak in July when 30 cm soil moisture is generally around 10%, about 1-2 months after the start of the dry season. Sap velocities decrease to near zero during a rainstorm in early October when both insolation and VPD decline, and soil moisture increases. Thereafter both VPD and sap velocities picked up while soil moisture continues to decline. Day-to-day variations in VPD are large, and show no significant trend through the dry season, but insolation (approximated here as observed total solar radiation scaled by slope and aspect as though it were direct-beam radiation) varies substantially on the north slope over the dry season.

4.5, but the time series maxima show the extremes for the whole month, to help set the context. For instance, in late September and October, the south slope can become nearly 7°C hotter with 1.8 kPa higher VPD, and this climate difference occurs in the late morning-early afternoon. In contrast, in July, the month of peak sap velocity and cross-slope sap velocity differences, the largest cross-slope temperature and VPD differences are less than half the magnitude seen in October. Early in the dry season, the north slope also has a predictable time of day during which it is hotter and drier than the south slope, in the early evening. This is because the solar azimuth angle is north of due west in the evening prior to the equinox (see Figure 4.3), which has a noticeable impact on north slope microclimate until about mid-August. Evening cross-slope differences become negligible in the later dry season, when the sun sets closer to due West.

Table 4.1: A month-by-month summary of shifting environmental conditions on each slope. Rows labeled “Max” refer to the maximum value observed over the whole month, and values are reported with the date, hour, and minute recorded. “ClmMax” refers to the climatological maximum, i.e. the maximum of the average diurnal cycle of each variable observed over the whole month.

Sap Velocity (cm/hr) Maxima, by month:					
	June	July	August	September	October

Max (N)	**16.44** 06-30 15:55	**18.22** 07-19 13:55	**13.51** 08-02 13:45	**9.30** 09-01 14:00	**6.40** 10-08 14:25
Max (S)	**16.65** 06-30 15:35	**18.45** 07-19 13:00	**16.01** 08-02 13:40	**10.48** 09-04 14:05	**5.83** 10-14 15:10
Max (S-N)	**9.54** 06-30 10:05	**11.35** 07-25 10:20	**9.16** 08-01 10:50	**5.79** 09-04 11:25	**2.38** 10-04 12:55
Max (N-S)	**3.23** 06-23 18:45	**3.11** 07-01 18:50	**0.94** 08-07 19:45	**2.41** 09-20 14:25	**1.53** 10-19 14:25
ClmMax (N)	**12.08**, 14:15	**15.05**, 13:50	**9.65**, 14:20	**6.30**, 14:25	**4.09**, 14:50
ClmMax (S)	**12.62**, 13:05	**16.00**, 12:35	**11.89**, 14:05	**6.77**, 14:55	**3.83**, 15:00
ClmMax (S-N)	**5.97**, 10:30	**9.44**, 10:20	**5.72**, 11:15	**2.99**, 11:45	**0.92**, 12:15
ClmMax (N-S)	**1.66**, 18:45	**1.19**, 18:40	**0.46**, 19:40	**0.27**, 18:40	**0.32**, 14:30
VPD (kPa) Maxima, by month:					
	June	July	August	September	October
Max (N)	**4.66** 06-30 13:55	**5.13** 07-18 13:55	**4.21** 08-18 14:45	**4.13** 09-27 13:35	**2.27** 10-14 14:25
Max (S)	**4.79** 06-30 13:55	**5.30** 07-18 13:50	**4.59** 08-18 14:35	**4.69** 09-27 12:40	**3.03** 10-16 12:20
Max (S-N)	**0.62** 06-30 20:00	**0.76** 07-17 11:20	**0.88** 08-18 10:55	**1.83** 09-26 10:55	**1.69** 10-13 11:40
Max (N-S)	**0.36**	**0.54**	**0.46**	**0.18**	**0.11**

	06-24 16:15	07-28 17:00	08-08 16:55	09-10 17:05	10-27 17:30
ClmMax (N)	**2.07**, 15:25	**3.05**, 16:00	**2.37**, 14:50	**2.09**, 13:50	**1.15**, 14:00
ClmMax (S)	**2.12**, 14:00	**3.16**, 13:20	**2.46**, 14:30	**2.30**, 12:40	**1.56**, 13:50
ClmMax (S-N)	**0.20**, 09:10	**0.30**, 09:05	**0.32**, 10:25	**0.56**, 10:45	**0.71**, 11:45
ClmMax (N-S)	**0.17**, 16:30	**0.23**, 16:50	**0.18**, 16:55	**-0.001**, 06:10	**0.01**, 05:40
Air Temperature (°C) Maxima, by month:					
	June	July	August	September	October
Max (N)	**34.53** 06-30 14:35	**35.95** 07-18 14:00	**32.21** 08-18 14:50	**32.22** 09-27 14:10	**23.46** 10-13 14:15
Max (S)	**35.20** 06-30 13:55	**36.83** 07-18 13:10	**33.38** 08-18 14:15	**34.34** 09-27 12:35	**27.76** 10-13 13:15
Max (S-N)	**2.54** 06-23 00:25	**2.38** 07-01 08:05	**3.17** 08-18 11:00	**6.34** 09-26 10:55	**6.61** 10-20 11:30
Max (N-S)	**1.97** 06-17 15:50	**1.57** 07-28 17:00	**1.71** 08-21 15:30	**0.89** 09-05 18:25	**0.78** 10-22 17:10
ClmMax (N)	**24.28**, 15:20	**29.67**, 15:50	**26.61**, 14:05	**24.24**, 13:45	**19.37**, 14:25
ClmMax (S)	**24.73**, 12:55	**30.37**, 13:20	**27.34**, 14:15	**25.28**, 13:20	**21.29**, 14:15
ClmMax (S-N)	**1.14**, 08:25	**1.44**, 08:55	**1.60**, 09:45	**2.77**, 10:20	**3.30**,11:40
ClmMax (N-S)	**0.82**, 16:30	**0.90**, 16:55	**0.79**, 16:55	**−0.30**, 21:20	−**0**.41, 05:10
Insolation (W/m^2) Maxima, by month:					
	June	July	August	September	October

Max (N)	**774.4** 06-09 16:35	**841.9** 07-06 14:55	**654.5** 08-05 13:50	**475.9** 09-01 13:30	**347.5** 10-04 13:55
Max (S)	**1006** 06-09 11:55	**1108** 07-06 11:55	**1039** 08-10 12:40	**1096** 09-22 12:15	**1006** 10-04 13:55
Max (S-N)	**332.5** 06-09 11:15	**378.9** 07-31 12:15	**479.0** 08-31 11:35	**711.7** 09-30 11:40	**790.9** 10-28 11:45
Max (N-S)	**360.0** 06-20 17:55	**487.8** 07-07 17:50	**277.08** 08-02 17:45	**115.6** 09-01 17:25	**0.00** 10-04 05:55
ClmMax (N)	**650.5**, 14:10	**613.8**, 14:55	**524.4**, 13:50	**380.1**, 13:20	**171.9**, 13:20
ClmMax (S)	**897.5**, 12:25	**883.6**, 12:30	**890.0**, 12:40	**870.0**, 11:40	**743.9**, 12:05
ClmMax (S-N)	**288.7**, 11:20	**300.5**, 11:55	**391.0**, 11:45	**534.8**, 11:40	**593.2**, 10:50
ClmMax (N-S)	**320.0**, 17:45	**298.5**, 17:50	**166.71**, 17:30	**27.5**, 17:15	**0.00**, 05:50

4.3.2 Microclimate and sap velocity climatologies for the north and south slopes

Monthly climatologies of the diurnally cycling variables (i.e., all except soil moisture) display the microclimate and sap velocity differences between the two slopes, and provide a snapshot of how these variables evolve together throughout the dry season (Figure 4.5). As expected from Figure 4.3, noontime insolation on the south slope is nearly double that of the north slope from August until October, leading to instantaneous air temperature differences of up to ~7°C and VPD differences of up to 1.8 kPa (Table 4.1). In the late afternoons of early summer through mid-August, insolation is greater on the north slope than on the south slope (see Figure 4.3), leading to brief (~2-

hour) periods of higher air temperature, VPD, and sap velocity on the north slope. A symmetrical period of greater insolation in the early mornings does not materialize, due to a slight westward aspect of both slopes (see Figure 4.1).

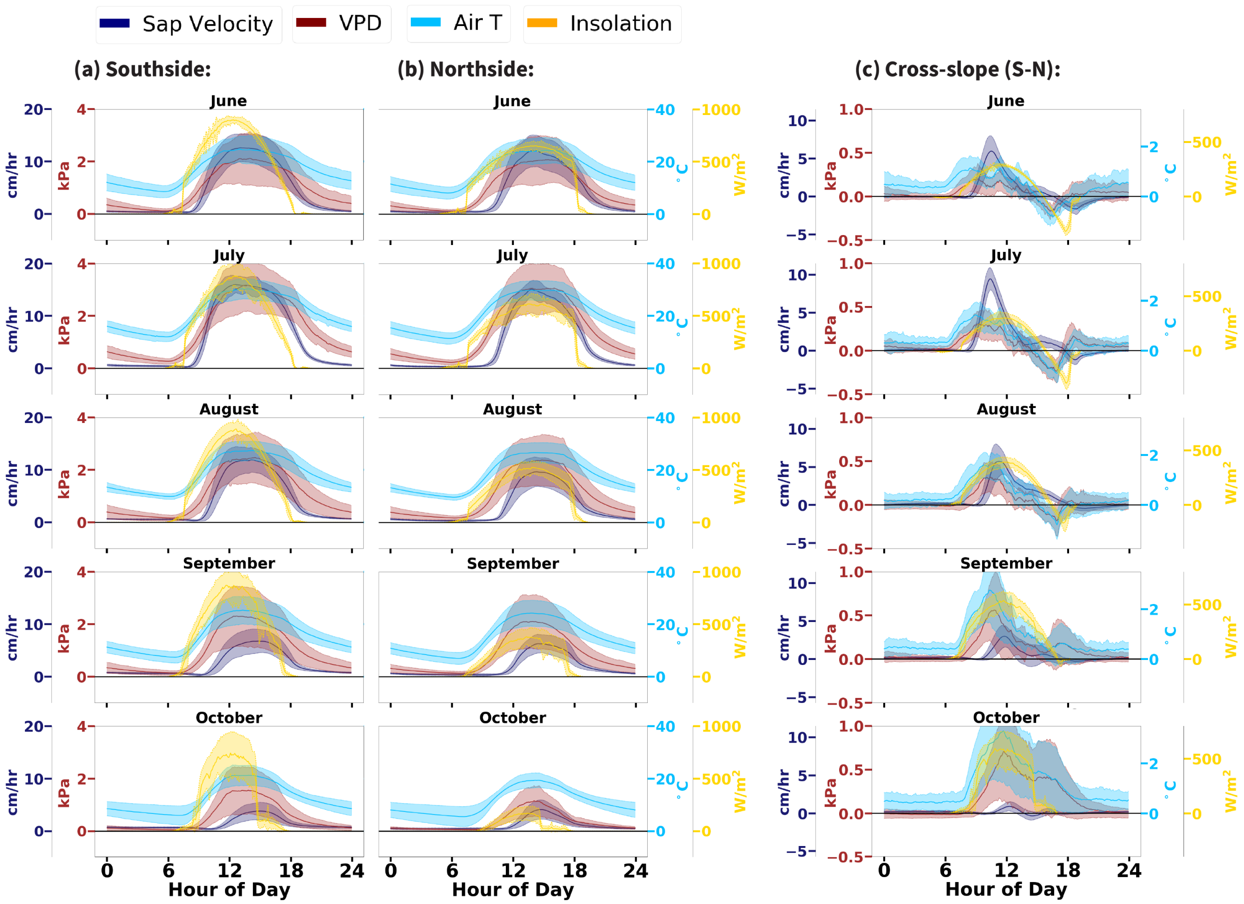

Figure 4.5: Monthly climatologies of diurnally cycling environmental drivers of sap velocity for the south slope (panels of column (a)), the north slope (panels of column (b)), and for the cross-slope differences (panels of column (c)). Shading shows +/- 1 standard deviation of the monthly climatology, and thus reflects the variability over the month. For all the months of the dry season and on both slopes, air temperature (pale blue) rises and falls in close concert with the sun (yellow), while the VPD diurnal cycle (burgundy) lags behind, and sap velocity (purple) lags behind even further. Though cross slope differences in sap velocity peak in July, the cross-slope microclimate differences peak in the late dry season, in September and October.

Both the south and north slopes show sap velocities that peak, not surprisingly, around mid day. However, the south-slope sap velocity is substantially faster than north-slope sap velocity in late morning, while the north slope flows slightly faster than the south slope in the late afternoon and early evening in the early summer. The cross-slope dynamics of the sap velocity diurnal cycles thus reflect the cross-slope dynamics of the diurnal cycles in above-ground microclimate.

4.3.3 Comparison of integrated sap velocity between slopes

Figure 4.6 underscores the differences between the two slopes in timing and amount of sap velocity in the diurnal cycle. We use time-integrated sap velocity as a proxy for transpiration on each slope, assuming that tree populations have equivalent sapwood area in trunks of equivalent diameter. Under this assumption, on average, south-slope madrones transpire 20% more water per day over their combined sapwood area during the dry season. August shows the largest percentage differences in transpiration, with south-slope madrones transpiring on average 32% more water per day over their combined sapwood area during this month. While for most of the dry season the average south-slope madrone tree moves water as fast or faster than the average north-slope madrone tree at their respective moments of daily peak sap velocity, Figure 4.2 shows that late in the dry season the north slope madrone trees are slightly faster, although they still transpire less per day.

4.4 Conclusions

It is known that vegetation exhibits a wide range of responses to ambient environment. Here, we show that microclimatic variability arising from topographic complexity has a substantial impact on the spatial distribution of water fluxes. In particular, 1) There are substantive microclimate differences between slopes; and 2) Population-level sap velocity differences between tree populations inhabiting the north and south slopes indicate substantive transpiration differences between slopes.

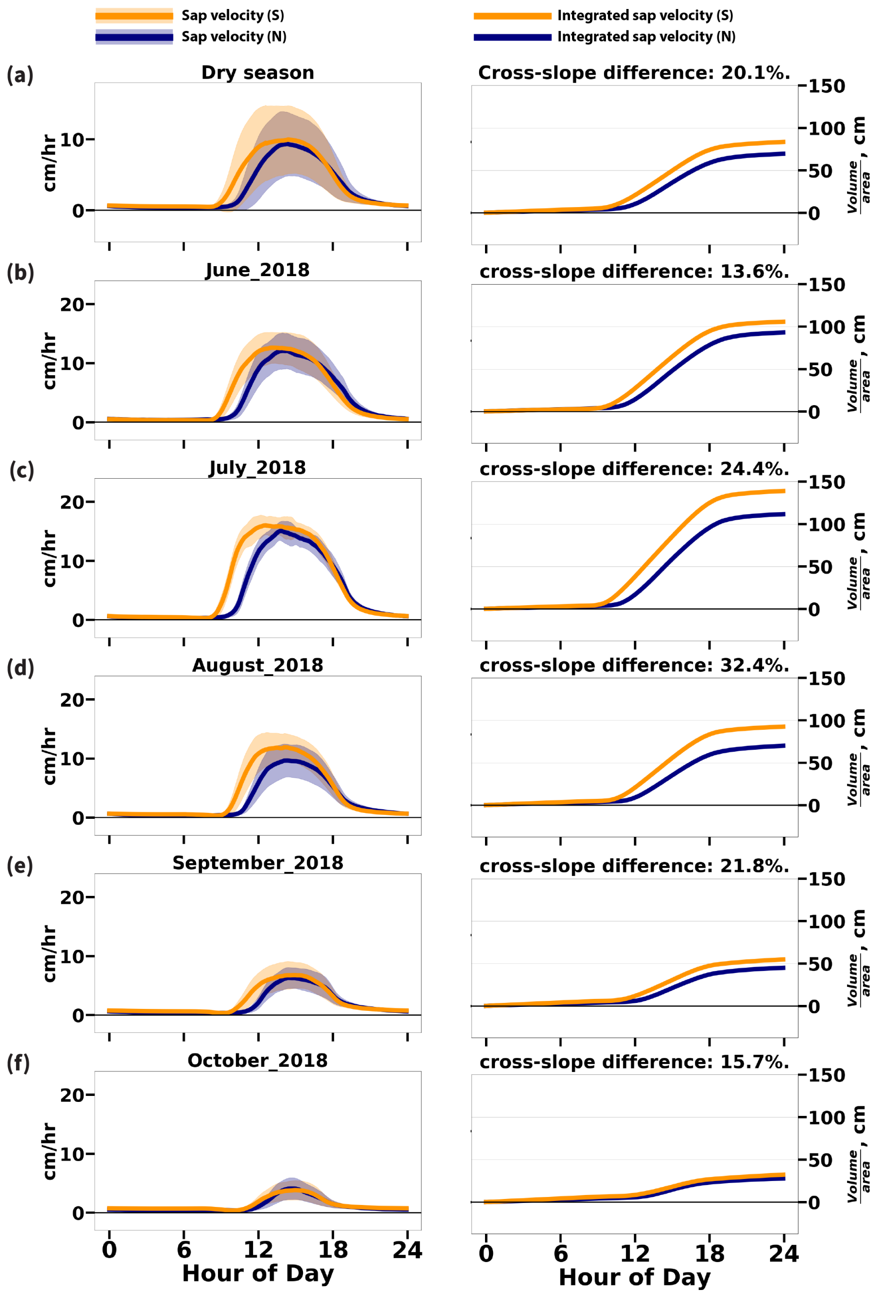

Figure 4.6: See next page for caption.

This lends spatial complexity to the anticipated vulnerability of vegetation to future change. Beneath an optimum light intensity for photosynthesis, trees living in dimmer light environments will demand less water under similar conditions of soil moisture and VPD. However, given that trees are known to

Figure 4.5: (on previous page) Average diurnal cycles (left panels) and cumulative integrals (right panels) of sap velocity for the entire dry season (panels in row a) and by month (panels in rows b-f). Time-integrated sap velocity, used here as a proxy for transpiration, results in units of centimeters, which can be understood as volume per area (right-hand axis), or put another way, the average distance water travels up the trunks, through the trees' combined sapwood area. The north slope is shown in purple and south slope is shown in orange; shading shows +/- 1 standard deviation of the climatologies, reflecting the variability over the time period (month or dry season). The south slope exhibits higher rates of time-integrated sap velocity, a proxy for transpiration, beginning earlier in the day and also experiencing a longer stretch of high sap velocity. Later in the dry season, the north slope experiences faster peak sap velocities, although it still produces less cumulative transpiration. See Figure 4.2.

optimize growth, including type of leaf and distribution of stomata throughout the crown space, different radiation environments, the difference in water demanded is likely to follow from a different relationship to environmental conditions. We explore this aspect in the next chapter.

Chapter 5

Vegetation acclimation detected from model parameters

5.1 Introduction

Plant transpiration is a major conduit for the transfer of water from the land to the atmosphere [45]. The leaf-to-atmosphere link governing this water flux is sensitive to spatially variable environmental conditions (e.g., [55, 38, 2]), indicating a need to zoom in to the fine scale of this variability in order to understand the future evolution of both land surface water fluxes to the atmosphere and ecological change. Microclimates have been found to exert a distinct control on long-term ecosystem vulnerability, separate from evolving macroclimate [22, 21], and yet, the influence microclimatic variations is often omitted in models used to forecast ecosystem vulnerability, due to a lack of data [70, 63].

The urgency of understanding the vulnerability of forest ecosystems to changing climate conditions in arid or Mediterranean climates has been underscored by mass tree die-offs in western North America [4, 92, 28], and worsening wildfire regimes around the world. Yet, the influence of natural microclimatic variations, such as those associated with topographic position, on plant–water relations and physiology is often omitted in models used to forecast ecosystem vulnerability, due to a lack of data [70, 63].

Our aim is to understand how microclimates caused by topographic complexity may feed back into spatial variations in tree physiology and ultimately variations in tree vulnerability to fire or mortality under stressful conditions.

To do this, we examine data from our field study at the University of California's Angelo Coast Range Reserve in Northern California, a site which is now NSF's Eel River Critical Zone Observatory, to develop a statistical analysis of vegetation function. The focus is sap flow measurements from a single evergreen tree species, *Arbutus menziesii*, straddling a microclimate gradient during the dry summer. The hypothesis guiding our study is that occupying disparate microclimates leads to different water use habits even in a single species of tree.

We present here a series of modeling exercises designed to investigate the effect of disparate microclimates on water fluxes from Pacific madrone, which is a deeply rooted, drought-tolerant, broadleaf evergreen tree. The climatic gradient created by differences in solar radiation on adjacent north- and south-facing slopes of a hill is used to explore the impact of variable microclimate on sap velocities, and thus transpiration, in this species of tree. We define microclimate by ambient air temperature and humidity beneath the canopy, incoming solar radiation adjusted for the slope and aspect of the closed canopy, and soil moisture measured at 30 cm.

Our study is inspired by a long history of ecological studies of plants across resource gradients (e.g., [79, 41, 19]), including several at fine scales which consider slope and aspect in particular [64, 51, 39, 76, 3]. The cross-slope microclimate gradient underlying our study is a 'controlled laboratory' to investigate the response of sap velocities to altered temperature (T), vapor pressure deficit (VPD), and geometrically-varied light (I) regimes in particular, as other relevant environmental factors, such as precipitation, cloud cover, underlying lithology, and soil type, are comparable between adjacent hillslopes. Investigation of water dynamics in this setting provides insight into how vegetation–atmosphere water cycle interactions may evolve under future climates with different temperature and VPD regimes, which contributes to more accurate projections of anticipated water fluxes and ultimately ecosystem vulnerability under an altered climate.

In the following sections, we present material previously published in [8], which include our derivation of a transpiration model, our parameterization (with a Markov Chain Monte Carlo process) of this model based on the cross-slope differences in microclimate and sap velocity (direct quantification of these differences described in chapter 4), and a detailed analysis of the implications of resulting parametric differences. We conclude by exploring the implications of cross-slope differences in ecological response parameters for forest resilience in this region under future climates, including a discussion of the limitations of our analysis and proposed next steps.

5.2 Methods

5.2.1 Site description

This study uses data collected at the University of California's Angelo Coast Range Reserve (39.729N, -123.644W), a steeply sloped site hosting a forest composed of mixed broadleaf and needleleaf evergreen trees typical of the Douglas fir Pacific alliance [86]. The installations are described in chapter 2.

For the purpose of examining cross-slope differences in sap velocity, our analysis is focused on the dry months (June–October). This time frame simplifies the relationships between sap velocity and environmental conditions in four ways: 1) we avoided conditions of post-rain leaf wetness, which could result in sunny conditions with low transpiration; 2) we simplified the correlation of 30 cm moisture dynamics with those of deeper moisture layers, which the trees at this site are accessing [69]; 3) we largely avoided cloudy-sky conditions, enabling our simplified light-scaling scheme; and lastly, 4) during a time of continuously declining subsurface moisture availability, we hypothesize that above-ground microclimatic variations may have the largest impact. We focus on Pacific madrone trees (*Arbutus menziesii*) because their prevalence on both slopes at our site allows for the highest possible rate of same-species sampling.

5.2.2 Data inputs

The high-frequency data streams for June–October 2018 include the sensor-averaged microclimate and sap velocities for the north and south slopes, as well as the sensor-averaged soil moisture for the south slope. Figure 4.4 illustrates what the MCMC parameterization process used as inputs. As we lacked *in situ* soil moisture observations for the north slope, the soil moisture data input was identical for both slopes in our set up, though we tested other representations.

Figure 5.1 shows several other soil moisture states that we considered for the north slope.

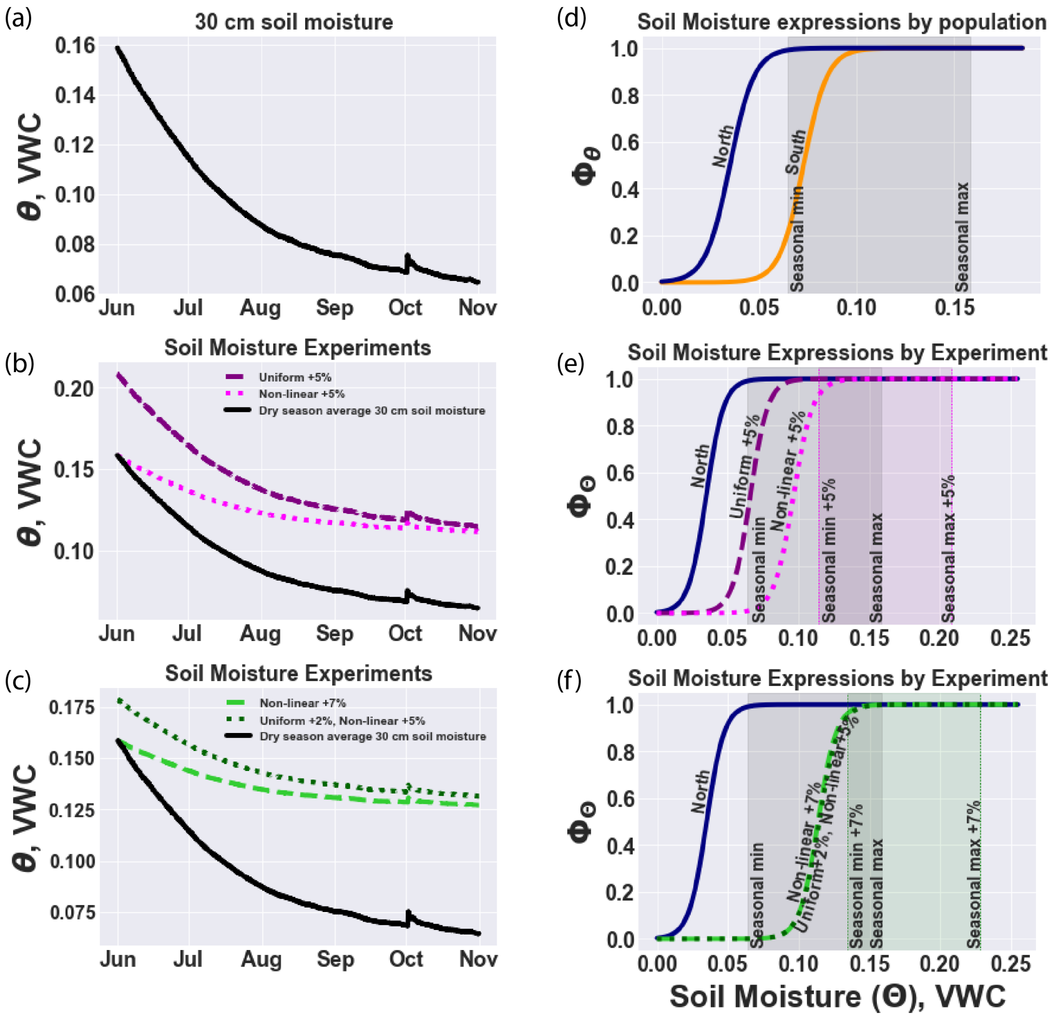

Figure 5.1: Experimental manipulations of the north slope soil moisture time series (left side panels) reveal that under a range of hypothetical conditions, the MCMC parameters fitted for the north slope consistently lead to functional expressions (right side panels) that indicate a lack of soil moisture constraint.

5.2.3 Description of sap velocity model

To quantify the relationship between sap velocity dynamics and environmental drivers for each slope, we derived a model of sap velocity tailored to the measurements available. Our derivation began from the work of [55], who, in order to understand the seasonal dynamics of daily maximum sap velocity across different tree species on the north slope of this site, applied the conceptual framework of the Jarvis model [44], in which the maximum bulk canopy conductance (g_{cmax}) under ideal conditions is modulated by ambient conditions to yield the instantaneous bulk canopy conductance, g_{c}. Furthermore, by assuming total transpiration E, approximated as $E = g_{\mathrm{c}} \times \mathrm{VPD}$, is proportional to the normalized sap velocity v_{n} with a proportionality constant α: $E = \alpha \times v_{\mathrm{n}}$, they obtained the equation:

$$v_{\mathrm{n}} = \frac{g_{\mathrm{cmax}}}{\alpha} \times \mathrm{VPD} \times f_{\mathrm{VPD}}(\mathrm{VPD}) \times f_{\theta}(\theta) \times f_{\mathrm{I}}(I). \tag{5.1}$$

The forms of the functions are taken from literature sources, including [57], [27], and [90]:

$$f_{\mathrm{VPD}}(\mathrm{VPD}) = \frac{1}{1 + \frac{\mathrm{VPD}}{D_0}}, \tag{5.2}$$

$$f_{\theta}(\theta) = \frac{1}{1 + \exp(-\beta(\theta - \theta_0))}, \tag{5.3}$$

$$f_I(I) = \gamma(I - 1000) + 1, \tag{5.4}$$

where D_0, β, θ_0 and γ are parameters determined for each tree species using daily maxima of normalized observed sap velocity, VPD, insolation and soil moisture from February 2009 to October 2011.

Equation 5.1, developed to investigate the seasonality of normalized daily maximum sap velocity across tree species on the same slope (and same microclimate), is not applicable for modeling the diurnal cycle during the dry season, where hysteresis in the response of sap velocity to VPD and insolation is observed [94, 32]. We modified Equation 5.1 by allowing for a lag in the sap velocity response to diurnally cycling VPD and insolation of 1 and 2 hours previous, resulting in Equation 5.5. We chose these time frames based on observed lags in our data (see Figure 4.5). Because we did not see substantive diurnal variations in soil moisture θ in our data, we did not include lagged terms for Φ_θ in Equation 5.5. We further modified the approach by using sensor-averaged rather than normalized sap velocities, which provided the best match with the scale of our environmental data (see Section 4.2.3). Using sensor-averaged rather than normalized sap velocities and splitting the Φ_{VPD} and Φ_I expressions into three led to scaling differences in our parameters compared to [55], and in particular, our initial constant, the analog of g_{cmax}/α, has less relation to a theoretical maximum bulk canopy conductance, so for clarity we rename it ε. The resulting model for sap velocity v_{s} is:

$$v_{\text{s}}(t) = \varepsilon \times \Phi_{\text{VPD}}(\text{VPD}_t, \text{VPD}_{t-1}, \text{VPD}_{t-2}) \times \Phi_\theta(\theta_t) \times \Phi_I(I_t, I_{t-1}, I_{t-2})$$

$$\begin{aligned}
\Phi_{\text{VPD}} &= \frac{\text{VPD}_t}{1+\frac{\text{VPD}_t}{D_0}} \times \frac{\text{VPD}_{t-1}}{1+\frac{\text{VPD}_{t-1}}{D_{-1}}} \times \frac{\text{VPD}_{t-2}}{1+\frac{\text{VPD}_{t-2}}{D_{-2}}} \\
\Phi_\theta &= \frac{1}{1+\exp(-\beta(\theta-\theta_0))} \\
\Phi_I &= (\gamma_0(I_t - 1000)+1) \times (\gamma_{-1}(I_{t-1} - 1000)+1) \\
&\qquad \times (\gamma_{-2}(I_{t-2} - 1000)+1),
\end{aligned} \tag{5.5}$$

where t is time and t_{-1} and t_{-2} denote 1 and 2 hours previous, respectively. This results in additional parameters in Equation 5.5, D_0, D_{-1}, D_{-2}, γ_0, γ_{-1}, and γ_{-2}, in addition to β and θ_0.

5.2.3.1 Estimation of Slope-specific Parameters

We used Hamiltonian Monte Carlo [6], a type of Markov Chain Monte Carlo, and the No-U-Turn Sampler [40] to derive our parameters in Equation 5.5 for each slope. Parameter estimation used the pymc3 package in Python [78]. For each slope, we randomly selected 20% of the data (non-sequentially) and assigned it to a training data set, while reserving the remainder for testing model performance. We repeated this procedure five times, to ensure that parameter estimates did not change substantively depending on the sample assigned to the training data set. We used the same priors (bounded normal distributions bound at zero; see Table 5.1) for each model run, to ensure that emergent parameter differences arise from relations in the data and are not forced from priors. Our final reported parameters are the mean of the parameters arising from each of the five parameterizations for each slope.

Our choice of priors was informed through a combination of literature sources and empirical exploration of the data. The priors for the γ parameters are chosen so that the function Φ_I ranges roughly between 0 and 1 over the range of observed insolation. The prior for β is the most restrictive, and is chosen such that both slopes will fit into a tightly curved sigmoid. The south slope data set predictably fits a tightly curved sigmoid even with an uninformative prior, but the north slope data set, appearing to be unconstrained by soil moisture, has the tendency to degenerate into a flat line (i.e., small β, arbitrary θ_0) if not constrained by the prior. Due to the multiplicative formulation of the models, constraining the prior for β in this manner enhances the clarity of direct comparisons made between ε and D parameters between the final north and south slope models, but it does not impact model accuracy or affect the explanatory power of each individual expression of the model. The prior for θ_0 is chosen based on an empirically-informed guess at the critical soil moisture threshold that begins to constrain sap velocities. The priors for the D parameters are chosen such that Φ_{VPD} ranges roughly between 0 and VPD_{max}. The prior for ε is chosen to be of the correct magnitude to scale the other portions of the equation to a hypothetical maximum sap velocity.

The posterior estimates for all D parameters deviate from our prior D by roughly a factor of ten. This is compensated by the growth of ε away from our prior guess. Because Φ_θ and Φ_I vary between 0 and 1, the scaling of modeled sap velocity depends on the product of Φ_{VPD} and ε, which is responsible for the inverse relation in their respective deviations from our priors. Embedded into our priors for ε and D is a hypothesis about the nonlinear relationship between sap velocity and VPD. Smaller D parameters would increase the curvature of Φ_{VPD}, and decrease the magnitude of the function overall. The posteriors of Φ_{VPD}'s D parameters and ε imply that the effect of VPD on sap velocities seen in our observations is less linear and “saturates" more quickly than our prior parameters would indicate. In essence, the priors were performing as intended: namely, we had included an adequate amount of uncertainty into them, such that the MCMC process could still arrive at an optimal solution.

We determined this based on the strong performance of the resulting models, and also based on the types of errors the models contain. The very weak correlations of the error term with VPD (see section 3.3.1) further support the parameters estimated by the MCMC process.

5.3 Results & Discussion

5.3.1 Model Parameters

The probability density distributions of the Equation 5.5 parameters estimated for the north and south slopes are shown in Figure 5.2. The means and standard deviations of the priors and posteriors of the parameters are shown in Table 5.1.

Table 5.1: Priors for our MCMC parameterization, and the resulting posteriors. All runs began with identical priors. Posterior means and standard deviations are derived from five separate runs, each using a randomly selected 20% of datapoints.

MCMC parameters				
	Prior mean	Prior SD	Posterior mean	Posterior SD
South Slope:				
ε	6	60	900	26.0
D_0	3.0	1.0	0.380	1.88 E−2
D_{-1}	3.0	1.0	0.330	1.92 E−2
D_{-2}	3.0	1.0	0.223	9.61 E−3
β	160	6	163	2.32
θ_0	0.07	0.01	7.28 E−2	8.59 E−5
γ	6.0 E−4	2.0 E−4	6.83 E−7	6.81 E−7
γ_{-1}	6.0 E−4	2.0 E−4	8.30 E−4	2.89 E−6
γ_{-2}	6.0 E−4	2.0 E−4	1.20 E−6	1.20 E−6
North Slope:				
ε	6	60	779	30.5

D_0	3.0	1.0	0.216	1.42 E−2
D_{-1}	3.0	1.0	0.344	2.43 E−2
D_{-2}	3.0	1.0	0.801	3.02 E−2
β	160	8	163	5.94
θ_0	0.07	0.01	3.08 E−2	3.99 E−3
γ	6.0 E−4	2.0 E−4	4.30E−4	1.00E−5
γ_{-1}	6.0 E−4	2.0 E−4	6.08 E−4	1.43 E−5
γ_{-2}	6.0 E−4	2.0 E−4	5.05 E−4	1.76 E−5
Soil Moisture Experiment: **Uniform +2%, Non-linear +5%**				
ε	6	60	780	30.4
D_0	3.0	1.0	0.215	1.41 E−2
D_{-1}	3.0	1.0	0.344	2.42 E−2
D_{-2}	3.0	1.0	0.800	3.02 E−2
β	160	6	160	5.98
θ_0	0.07	0.01	6.94 E−2	9.62 E−3
γ	6.0 E−4	2.0 E−4	4.30E−4	1.00E−5
γ_{-1}	6.0 E−4	2.0 E−4	6.08 E−4	1.44 E−5
γ_{-2}	6.0 E−4	2.0 E−4	5.07 E−4	1.76 E−5

The resulting parameters for each slope show key differences in response to environmental drivers. With the VPD parameters D_0, D_{-1} and D_{-2}, a larger parameter value points to a greater sap velocity sensitivity to the variable (see Equation 5.5). The south slope has D_0, D_{-1} and D_{-2} values of 0.38, 0.33, 0.22, respectively, suggesting that south-slope sap velocities are most sensitive to instantaneous VPD, but also to VPD from 2 hours prior, though lagged VPD plays a slightly smaller role. The corresponding values for the north slope are 0.22, 0.34 and 0.80, suggesting that on the north slope VPD_{t-2} has the largest influence on sap velocities.

For insolation, the γ_0 and γ_{-2} for the south slope are near zero, suggesting that sap velocities there respond mainly to insolation of the past hour (I_{t-1}). For the north slope, the results suggest that sap velocities are sensitive to contemporaneous insolation as well as insolation of the past two hours, as γ_0,

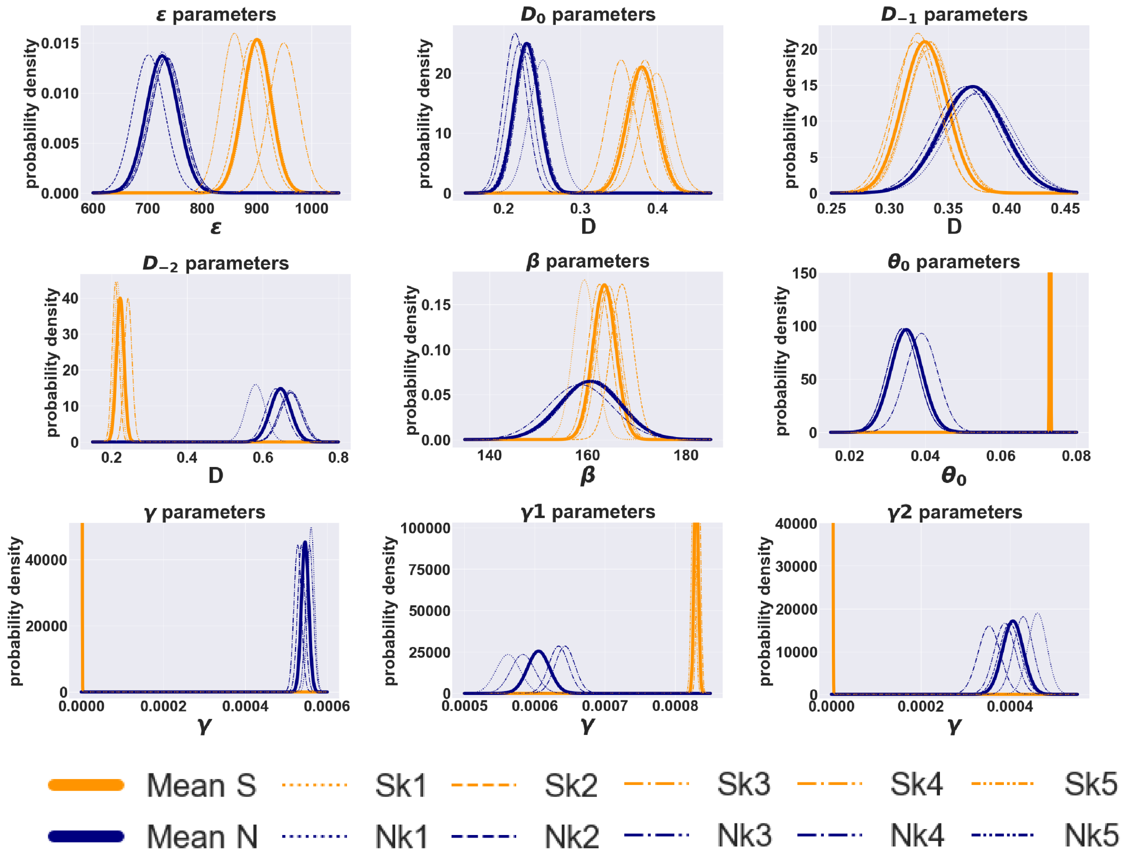

Figure 5.2: Posterior distributions of fitted model parameters for the north slope (blue) and south slope (orange). Results from each of the five randomly-selected training datasets are shown as dotted lines, and the mean as a bold line. Different subsets of data (k1-k5) used to parameterize the model result in very little difference in the fitted parameters, which is demonstrated in the narrow spread among the thin dotted lines.

γ_{-1} and γ_{-2} have comparable values.

For soil moisture, β controls the slope of the sigmoid, and θ_0 controls the midpoint. When soil moisture data input is identical for both slopes, β is similar between the two slopes, while θ_0 for the north slope is lower than that of the south slope by a factor of two. The partial function Φ_θ (see Figure S2, panel d) shows that while soil moisture is a strongly limiting factor on south-slope sap velocities below $\sim$10%, it causes no such limitation for north-slope sap velocities. Because soil moisture creates no constraint on sap velocities in the north-slope model, there is less certainty in the exact parameter values, as seen in the larger spread of the north-slope parameters β and θ_0 compared to the south slope (Figure 5.2).

5.3.1.1 Parameter sensitivity to north-slope soil moisture scenarios

As mentioned in Section 4.2.3, we lack surface soil moisture observations on the north slope. This missing data leaves the true values of β and θ_0 uncertain on the north slope. Because of the multiplicative model formulation, differences in these parameters and the value of the Φ_θ function could, in turn, impact the values of the other expressions and parameters in Equation 5.5, rendering the entire north-slope sap velocity response to microclimate uncertain. Our field experience and our sap velocity data streams show that north-slope soils are as wet or wetter than those of the south slope, presumably due to unequal evapotranspiration demand. Therefore, the north-slope soil moisture scenarios we explored in our sensitivity experiments began with the south-slope data stream and increased the soil moisture in both uniform and non-uniform ways. The scenarios were as follows: 1) we added a uniform 5% increase to observed south-slope soil moisture; 2) we adjusted the rate of soil moisture decline to half of the rate observed on the south slope, which amounted to a +5% difference in soil moisture by the end of the dry season; 3) we adjusted the rate of soil moisture decline to one third of the rate observed on the south slope, which amounted to a +7% difference in soil moisture by the end of the dry season; and lastly, 4) we added a uniform 2% increase to observed soil moisture, and then additionally adjusted the rate of soil moisture decline to half of the observed rate, which amounted to a +7% difference in soil moisture by the end of the dry season. We then reran the north-slope MCMC parameterization process with these alternative soil moisture states, and compared them with a standard run in which we matched soil moisture for both slopes to the area-averaged south-slope moisture state.

We found that between the standard and sensitivity experiment parameterizations, none of the final parameters changed substantively except θ_0 (Table S2). The changes in θ_0 that resulted do not change the shape of Φ_θ, but rather shift it along the θ-axis, tracking the new (higher) seasonal minimum implied by the alternative moisture scenarios (see Figure S2). The function Φ_θ did not decline below a value of 1 throughout the seasonal range of moisture hypothesized in each scenario. Thus, we conclude that, in our model formulation, the relations among the north-slope data streams indicate no sap velocity constraint by soil moisture, and that this conclusion is not sensitive to a plausible range of soil moisture states for the north slope.

5.3.2 Model performance

With slope-specific parameters in combination with slope-specific microclimate data streams, we computed model sap velocities for north and south slopes. From our final parameter distributions for each slope, we sampled 10,000 subsets of parameters, which, combined with the environmental data streams, generated an ensemble of modeled sap velocity time series consistent with the uncertainty in the model parameters for each slope. These ensembles were then used to generate the modeled sap velocity climatologies and modeled daily integrals reported in Figures 5.3 and 5.4.

To assess model performance, we used root mean squared error (RMSE), a scale-dependent measure, as well as normalized root mean squared error (nRMSE), a scale-independent measure:

$$\mathrm{RMSE} = \Big(\sum_{n=1}^{N_{\mathrm{obs}}} \frac{(\widehat{v_{\mathrm{s},n}} - v_{\mathrm{obs},n})^2}{N_{\mathrm{obs}}}\Big)^{1/2}, \tag{5.6}$$

$$\mathrm{nRMSE} = \frac{\mathrm{RMSE}}{(v_{\mathrm{obs,\,max}} - v_{\mathrm{obs,\,min}})}; \tag{5.7}$$

$\widehat{v_{\mathrm{s},n}}$ and $v_{\mathrm{obs},n}$ are the modeled and observed sap velocities, respectively.

The modeled sap velocities compare well with those observed. The model captures 88% and 89% of the June–September daily integrated sap velocity on the north and south slopes, respectively. The performance of the daily integrals deteriorates to 77% for both slopes when October is included. The reasons for this are addressed in Section 5.3.2.1.

A comparison of the mean diurnal cycle of the sap velocities and their dry season integrals is shown in Figure 5.4. The nRMSE is 4% and 5% for the north and south slopes, respectively, and increases to 5% and 6% when data for only

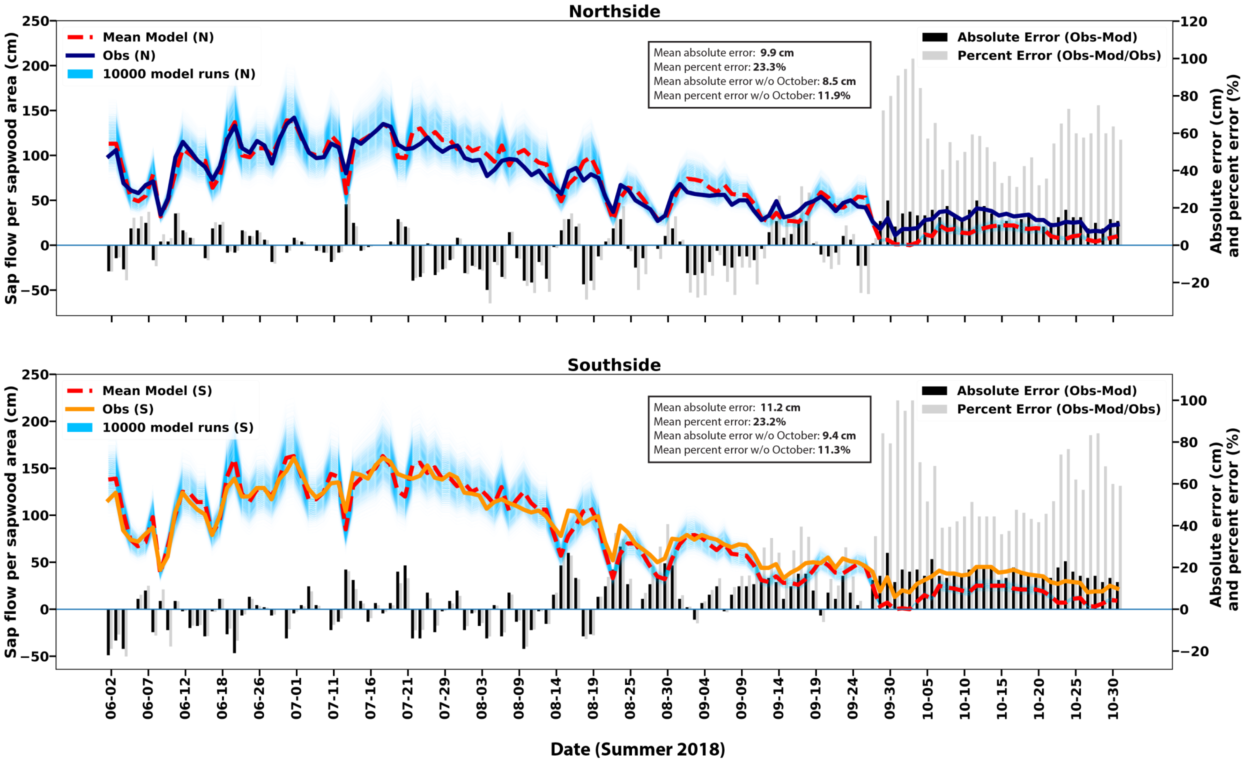

Figure 5.3: See next page for caption.

7am to 10pm are included (i.e., the dynamic portion of the day). The models capture 75% of the cross-slope difference in seasonal integrated sap velocities.

In summary, Equation 5.5 with the slope-specific parameters captures the main features of the observations.

5.3.2.1 Examination of residuals & limitations of analysis

The month of October stands out as a period of systematic error in Figure 5.3. There are several reasons. Firstly, the representation in a rough terrain of sunlight on the slopes scaled from a flat meadow observation becomes less accurate as the solar arc becomes lower in the sky (i.e., closer to the winter solstice). This is because the diffuse fraction of radiation becomes significant at low sun angles, when shading from neighboring hills, especially in early morning and late afternoon, plays an important role. In particular, the hill-shading received by our meadow-based light sensor begins substantially earlier in the

Figure 5.3: (on previous page) Daily integrated sap velocity yields a daily distance that water moves up the tree trunks over the combined sapwood area of the study population for each slope, which serves as a proxy for daily transpiration. Here we plot modeled (light blue lines with red dashed line representing the mean model run) and observed (orange line for the south and dark purple line for the north) daily integrated sap velocity for each slope, with the bars underneath representing both the absolute error in the model (black bars, units of cm) and the percentage error (light grey bars, unitless). The spread among the model runs is a visual indication of model uncertainty arising from spread in the parameter estimates. Error is computed relative to the magnitude of the observations, with positive errors indicating a model underestimate and negative errors indicating a model overestimate. The month of October is greatly underestimated due to seasonal shading of the light sensor positioned in the meadow, which is not representative of the tree environment. For the north slope, the model is able to capture 77% of dry season integrated sap velocity, and 88% of June–September integrated sap velocity. For the south slope, the performance is similar, with 77% of dry season integrated sap velocity and 89% of June–September integrated sap velocity represented.

day, in the late dry season, than the shading experienced by the trees under observation, which are positioned at a higher altitude. These factors account for the model predictions of sap velocity being artificially low compared to observations, as they are based on 1) a solar day in the low meadow that is 1-2 hours shorter than the trees on the slopes experience, and 2) insolation scaling appropriate for direct-beam insolation only, even though the fraction of diffuse radiation is potentially high or unequal between the slopes due to shading from neighboring hills on late October afternoons. Secondly, we note that October began with a rain storm which was the only substantive moisture input during the period under observation. This rain event likely altered the relationship between surface and deep moisture reserves compared to the rest of the dry season, confounding the relationship between our 30-cm soil moisture data and the deeper root zone moisture available in the month of October.

Apart from the month of October, the errors seem randomly distributed.

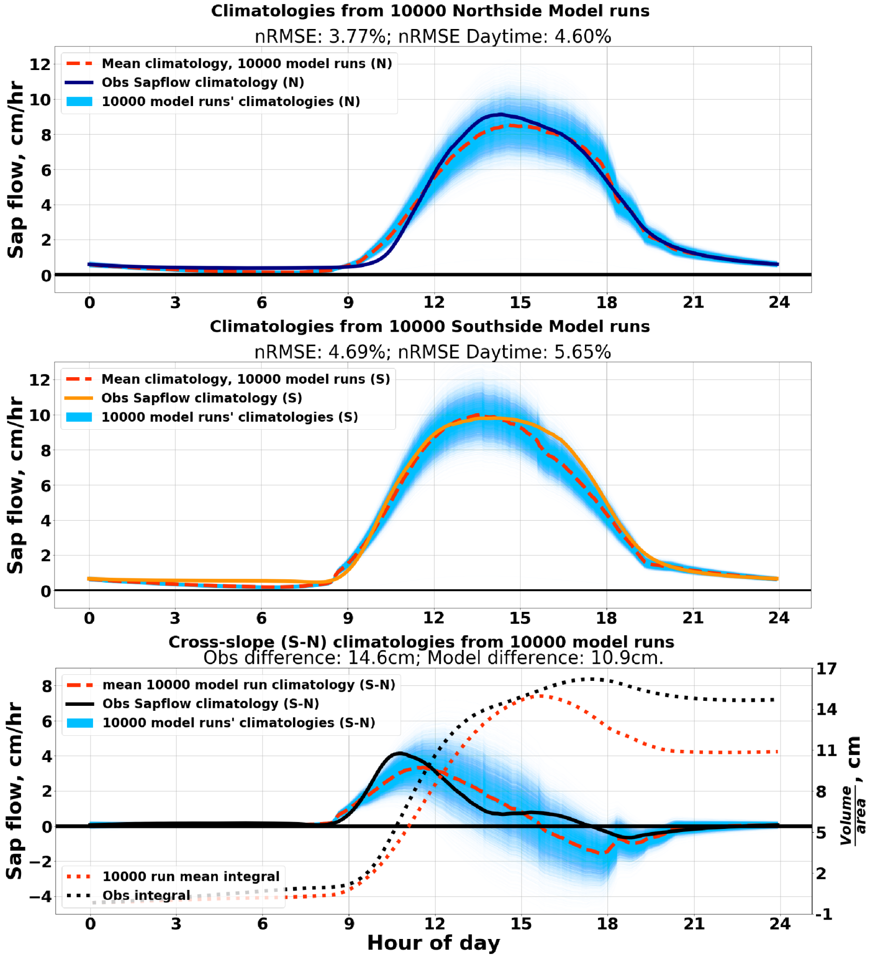

Figure 5.4: Performance assessment of models relative to the dry season average diurnal cycle. Dry season climatologies of 10,000 model runs are in pale blue, with the mean in red, and observed sap velocity in orange for the south and dark purple for the north. The spread among the 10,000 model runs is a visual indication of model uncertainty arising from spread in the parameter estimates. The normalized root mean square error (nRMSE) of the model comparison to observations is computed relative to the mean of the model runs, and is roughly 4% and 5% for the north and south slopes respectively (top two panels); if error is computed only over the active portion of the diurnal cycle (7am-10pm), this rises to 5% and 6% nRMSE for the north and south models respectively. The models are able to capture 75% of the observed difference in time-integrated sap velocity between the slopes (bottom panel).

We looked for, but did not find, correlations with wind speeds both in the time series and integrated over days. However, we can identify loose correlations of the residuals with daily integrated VPD. This suggests that there is a slight bias in our model towards overestimating sap velocity on exceptionally dry days, and underestimating it on more humid days.

5.3.3 Sensitivities of Sap Velocities to Microclimate

At the heart of our analysis is the question of whether cross-slope differences in sap velocity are proportional to the cross-slope differences in microclimate, or whether population-level differences in physiological function also play a role. Though the individual parameter differences in our sap velocity model suggest population-level differences in water usage sensitivity to environmental drivers, we sought a more intuitive way to understand these parameter differences in aggregate. To understand the disparate sensitivities of sap velocity to microclimate between these two populations, we carried out two sets of experiments. The first involved supplying the same diurnal cycle of VPD and insolation for both slopes and examining each functional expression of the model separately. In the second set of experiments, we performed a series of ‘climate swaps’ in which the model for one slope was given the total microclimate, or VPD and insolation alone, of the other. These are described below.

5.3.3.1 Model Experiment 1: same microclimate

In the first set of experiments, we computed mean diurnal cycles of VPD and insolation for the south environment in July, and used these mean cycles as inputs to Φ_{VPD} and Φ_I for both slopes (see Equation 5.5). Figure 5.5 shows the hysteresis loops in the sap velocity responses. For the same VPD diurnal cycle, the north-slope model's Φ_{VPD} attributes more sap velocity amplitude variations to variations in VPD than does the north slope model. Also, at every value of VPD, the north-slope model has a larger sap velocity response than the south-slope model. This shows that the north-slope model has both a higher baseline response to VPD as well as a higher proportional response to increases in VPD than the south-slope model.

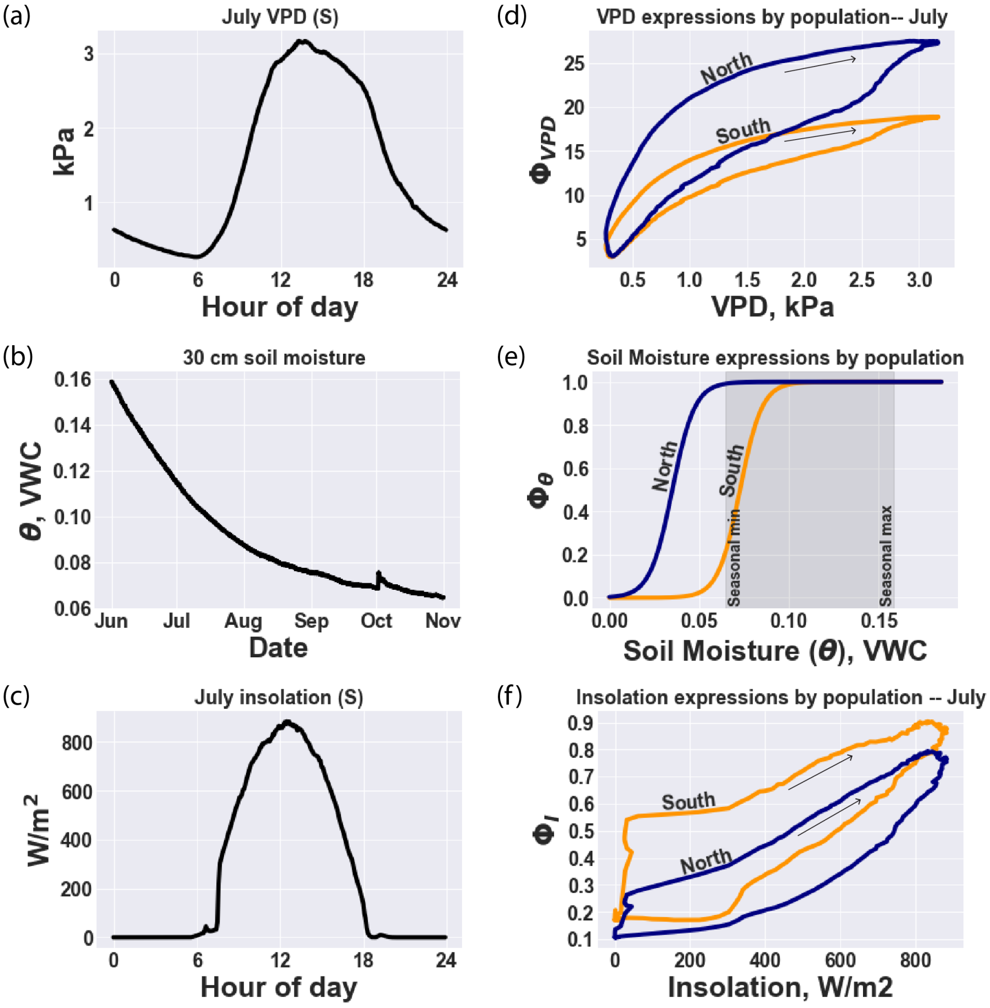

Figure 5.5: Partial expression plots of Equation 5.5 show differing sensitivity to environmental drivers among the two populations (right side panels), when fed identical data streams (left side panels). The north slope model is more sensitive to VPD, and less sensitive to soil moisture and insolation, indicating that the trees on the north slope do not feel additional transpiration constraint from drying soils over the course of the dry season, beyond that imposed by the light limitation.

The south slope Φ_I has higher values than the north slope over the range of observed sunlight, and covers a slightly larger range on the y-axis. This implies that modeled sap velocity on the south slope has a higher baseline response to sunlight, and a slightly more sensitive response to increases in sunlight.

Lastly, the south slope's soil moisture function shows soil moisture to be a limiting factor on sap velocities, while conversely the north slope shows no moisture constraint, within the range of observed soil moisture over the whole season.

Taken together, the model results indicate population-level differences in response to environmental drivers of transpiration. This is explored further in Section 5.3.4.

5.3.3.2 Model Experiment 2: Influence of parameters vs microclimate

In the second series of experiments, we exchanged some or all of the experienced microclimate between the models for each slope, as a way to observe the differences in environmental responses between the two models. This experiment is visually summarized in Figure 10.

The north-slope model substantially overestimates sap velocity in the south-slope microclimate, and the south-slope model underestimates sap velocity in the north-slope microclimate. Further, exchanging VPD environment while maintaining the native light environment makes very little difference; in contrast, exchanging the solar radiation environment while maintaining the native VPD environment makes a large difference to modeled sap velocities. Lastly, artificially increasing soil moisture increases the sap velocities on the south slope, but not the north slope.

The individual responses to environmental drivers, Φ_{VPD}, Φ_θ, and Φ_I (Figure 5.5) show that the overestimation of sap velocities by the north-slope model in the south-slope microclimate is not associated with a stronger response to light from north-slope trees, but instead with firstly a lack of moisture limitation on sap velocities, and secondly with a stronger response to VPD. Once the north-slope model is freed from its light-limited environment by using south-slope insolation, the added vigor of its VPD response compared to the south-slope model becomes clear.

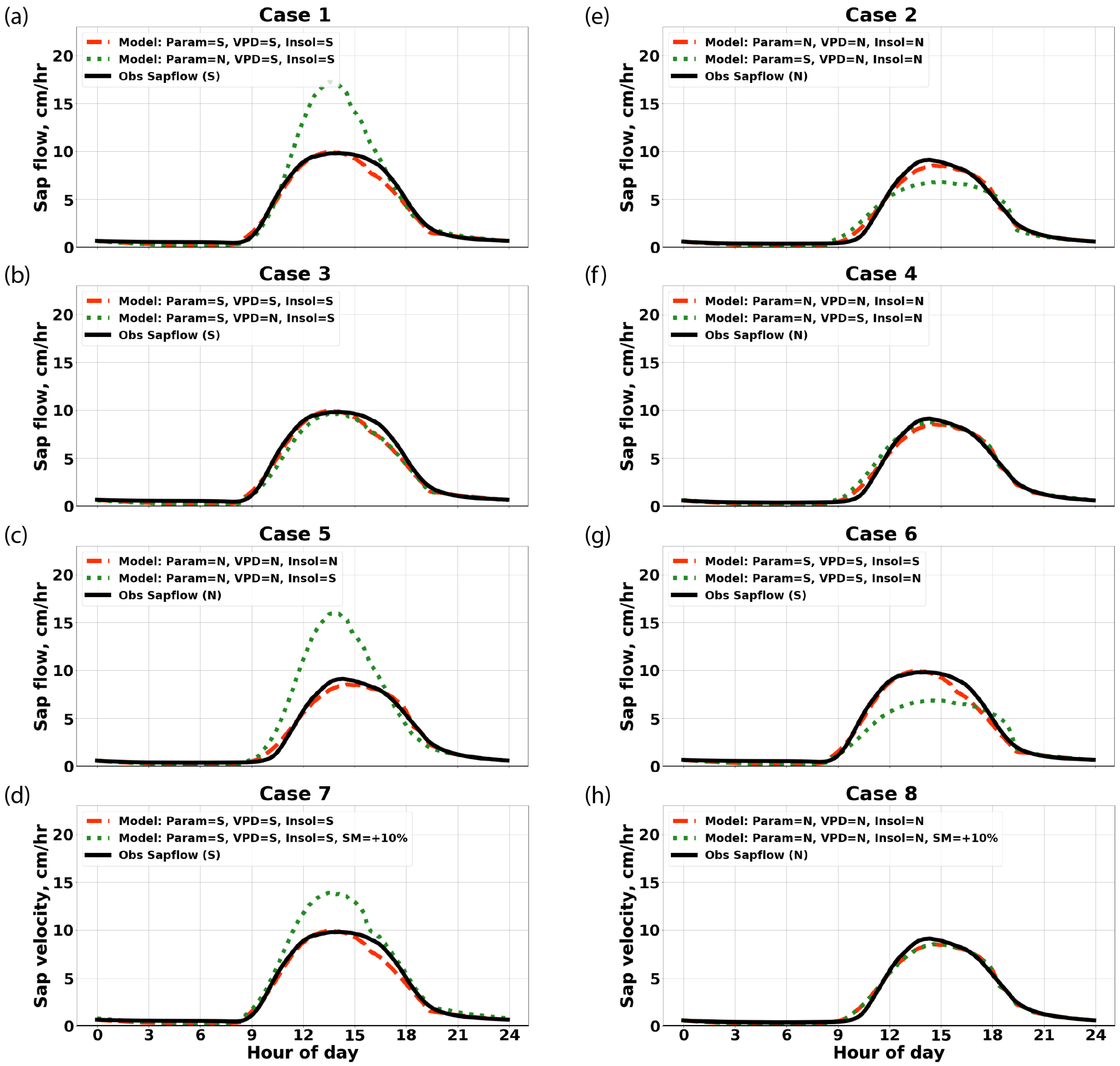

Figure 5.6: (See next page for caption.)

5.3.4 Interpretation of sap velocity model results

The divergent parameterizations indicate different physiological responses to environment between the two slopes, after controlling for inhabited microclimate. None of the parameters in our model is a direct metric of a particular physiological property of the trees, but they do represent an aggregation of

Figure 5.10: (Figure on previous page) Using the slope-specific models in the opposite slope's microclimate shows the differences in response generated by the two parameterizations to the same microclimate. Case 1 shows that the north model in a south microclimate (dotted green line) has a more vigorous response than both the south model (dashed red line) and the observations (solid black line) in the same microclimate, while conversely Case 2 shows that the south model in a north microclimate (dotted green line) underestimates both the north model (dashed red line) and observations (solid black line) in the north microclimate. Cases 3-8 break down the sensitivity by examining the impact of exchanging only one environmental variable at a time. While exchanging only the VPD portion of the microclimate between the two slopes makes almost no difference to the sap velocities estimated by each model (compare the dashed red and dotted green lines in Cases 3 and 4), exchanging the solar radiation environment makes a large difference (compare the dashed red and dotted green lines in Cases 5 and 6). Furthermore, reiterating Figure 5.5 panel (e), Cases 7 and 8 show that increased soil moisture increases predicted sap velocities in the south model, but not in the north model. The estimation by the north model of faster sap velocities than the south model in the south microclimate (Case 1) is due in roughly equal measure to the north model's lack of soil moisture constraint and more vigorous response to VPD. The radiation exchange (as seen in isolation in Cases 5 and 6) appears to produce most of this result because it frees the north slope model from serious light limitation.

functional or "behavioral" differences, integrated across all mechanisms that influence sap velocity response to ambient environment [44, 57]. Extrapolations of disparate physiological properties between the two tree populations from the differences in the models' parameters are speculative, but we explore these speculations to begin a discussion about the degree and kind of acclimation that may exist between trees on differing slope aspects. We consider the differences in each partial function Φ in turn.

VPD: Comparison of Φ_{VPD} in each model indicates that north-slope madrones are more sensitive to shifts in VPD than their south-slope counterparts

(Figure 5.5). This is corroborated by several lines of reasoning. Firstly, because of the stark differences in light environment between the two slopes of the hill, we expect that the relative abundances of sun-adapted and shade-adapted leaves differ in the overall composition of the madrone canopies representing each slope's population, with the north slope presumed to have more shade-adapted leaves than the south slope. There is a substantial body of literature describing the physiological differences between sun-adapted and shade-adapted leaves [10, 52], but because these differences are usually described in terms of carbon assimilation rather than water use, relating them to differences in transpiration dynamics between the two populations is challenging. To do this we would need information about relative water use efficiencies. This ties in with the second likely difference between the populations: differing canopy architectures along the lines of what is typical of sun-rich vs. shade-rich populations likely lead to differing light exposure regimes, which in turn could impact water use efficiencies on a population level. If, for instance, the proportion of leaf area accessing direct sunlight as opposed to indirect light, or even sunflecks, is less on the north slope, the north-slope transpiration dynamics could be expected to be based on lower water use efficiencies, due to differing strategies of stomatal regulation [49, 91]. Woody vegetation using sunflecks as a light source have been shown to leave stomata open during moments of low light in order to assimilate the most carbon when leaves are illuminated [82, 72, 50]. Thus, such differences in canopy architecture could result in tighter coupling between sap velocity and VPD in north-slope canopies, due to the likely prevalence of exposed stomata on leaves that do not continuously experience the top-of-canopy sunlight dynamics. While the impact of differing proportions of sun-adapted vs shade-adapted leaves is obscured by an inability to resolve the exact mechanisms involved, we do suspect that this also plays a role in shaping the differences we observe. We thus speculate that, due to both lower light levels and disrupted exposure to what light there is, north-slope trees are comparatively profligate water users even in the midst of the dry summer, preferring to maximize carbon assimilation rather than conserve water.

Soil Moisture: Φ_θ indicates that north-slope madrones are not water limited over the dry season. In our model, artificially increasing soil moisture for the north slope (i.e., 'watering' the trees) does not lead to increased sap velocity (see Figure 5.6, panel h). Nor does artificially increasing the soil moisture feeding into the MCMC algorithm alter the resulting north-slope parameters in meaningful ways (Figure S2). We hypothesize that this is because there is greater plant-available moisture on the north slope. The north slope has a deep water table (20 m) and a thick layer of weathered bedrock, and it has been shown to store around 30% of subsurface moisture in the vadose zone [74, 87]. While there is evidence that trees on both slopes use this deep 'rock moisture' in the vadose zone for part of the dry season [68], we have less data about the subsurface structure on the south slope, and data on respective rooting depths between the two populations is inconclusive [68]. However, the stronger sunlight on the south slope leads to higher evaporation, and the sap velocity data shows that the south slope trees cumulatively extract more water. Even if the subsurface structures and rooting depths were similar, there would be less soil moisture availability on the south slope. Also, the north-slope madrones grow in closer proximity to Douglas firs, which are known to exhibit hydraulic redistribution [15, 14], further contributing to increased moisture availability in the north-slope rooting zone.

Insolation: Φ_I indicates that south slope madrones have moderately higher sensitivity to insolation, and a larger response at every level of sunlight than the north-slope function (see Figure 5.5, panel c). The higher sensitivity in the insolation response on the south slope could be explained by factors similar to those influencing VPD response, namely a higher fraction of leaves exposed to direct light, leading to stomatal regulation strategies that are more in phase with changes in light than those on the north slope. The upwards shift in the magnitude of the response could be explained by higher proportions of sun-adapted leaves in the south-slope trees, which, due to their enhanced stomatal area [10], could have higher rates of water use at every level of light intensity. To summarize the complementary hypotheses around stomatal area embedded in our interpretations of Φ_{VPD} and Φ_I, we hypothesize that due to speculative population differences in tree architecture, stomatal area, and stomatal regulating behavior (made possible by below-ground differences in water availability), 1) the north-slope trees have a larger area of stomata exposed under conditions that combine lower light and higher VPD than their south-slope counterparts, who, being moisture limited, close their stomata under these conditions; and 2) south-slope trees have a larger area of stomata exposed under conditions that combine higher light and lower VPD, which do not occur on the north slope.

5.4 Conclusions

It is known that different species of vegetation exhibit a wide range of responses to ambient environment. Here, we show that even within a single species, substantial variation in environmental response can exist, which in turn may vary the functional role that species plays in biogeochemical cycles, and future vulnerability to a range of stressors. In particular, 1) There are substantive microclimate differences between slopes; 2) Population-level sap velocity differences between tree populations inhabiting the north and south slopes indicate substantive transpiration differences between slopes; 3) A sap velocity model parameterized only with ambient microclimatic conditions captures sap velocity for our site well; and 4) The parameter differences in our sap velocity model represent different responses to ambient environment, and imply functional differences in tree physiology, between the two populations. This is suggestive of acclimation to inhabited microclimate.

Our results strongly hint at acclimation in leaf and canopy structure and differing stomatal regulation strategies (as in [88]) between the two populations of trees. We suggest that north-slope trees, limited by sunlight rather than soil moisture, have developed their canopies and stomatal regulation strategies to optimize for light capture while spending water more profligately than their south-slope counterparts. Through this optimization, the north slope may be presumed to have different rates of carbon fixation per area of leaf and unit water transpired. This has implications for understanding water and carbon fluxes from forests today, and also for anticipating population-level profiles of vulnerability to future conditions.

Climate change is expected to alter current regimes of temperature (increase, [77]), VPD (increase, [36]), precipitation (slight increase, although with decreased water availability, [77, 93]), and cloudiness (unknown direction of change, [93]) over California. All three of these changes impact the environmental covariates in this model. The model results suggest that the south slope trees become severely water limited by the end of the dry season, and thus further water limitation may either limit their growing season, or create conditions that limit their performance. In contrast, on the north slope, the trees do not appear to be water limited. However, it is unclear whether this makes them more resilient to a hotter or drier future. In our interpretation of parameter differences, north-slope trees likely rely on much higher rates of water usage in order to assimilate carbon. If water becomes a limiting resource in the north-slope microclimate in the future, and VPD levels continue to increase, these north-slope trees may be closer to crisis, choosing between cavitation or carbon starvation, than the south-slope trees would be under a more limited growing season [88, 36].

More measurements are needed to elucidate specific mechanisms underlying the parameter differences we have found. Measurements of photosynthesis/gas exchange on the leaf level, or chemical analyses of leaf tissues including C:N ratios or isotopic composition, could help shed light on physiological differences in leaves between populations. These measurements were not practical in our study given our lack of canopy access, but more measurements on these trees, or parallel investigations in a greenhouse, could be useful as a future study.

Chapter 6

Explorations with the FATES vegetation demography model

6.1 Introduction

Solar radiation differences generate different microclimates across adjacent north- and south-facing slopes in the mid-latitudes, which is one mechanism by which inhabited topography impacts plant function. My high-frequency measurements at the Angelo Coast Range Reserve in northern California's North Coast Range documented the different microclimates and co-varying tree water use across a hill slope divide during a dry Mediterranean summer. These measurements showed that transpiration of a single tree species is higher on the drier, sunnier south-facing slope [8]. Analysis with an environmental response model revealed that these transpiration differences result from different sensitivities of their water use to environmental conditions. We interpreted these differences in how the trees of each slope were responding to their microclimates to be a signature of long-term (1-10 year) acclimation to the microclimate, which is an under-observed time scale of vegetation functional plasticity.

The environmental sensitivities in water use that differ between the two populations of trees include the responses to vapor pressure deficit (VPD), sunlight, and soil moisture. Given the unquantifiable differences in average total root zone moisture between the two populations, we concluded that the different sensitivities to soil moisture indicated in the environmental response model are best understood as indicating different transpiration-limiting conditions rather than different vegetation tolerances. Specifically, we suggest that less-abundant sunlight limits the rate of transpiration on the north slope, which, due to its geometric orientation, receives both less-intense direct-beam radiation and shorter day lengths than neighboring flat regions or south-facing slopes, and that this causes the north-slope tree populations to avoid conditions of soil moisture limitation. We suggest that the south slope population, experiencing abundant sunlight, is instead limited by soil moisture. We further hypothesized that the differing responses to VPD and sunlight seen in the two populations were generated by differences in canopy structure, including different quantities and distributions of sun and shade leaves, that developed in response to the populations' respective microclimates.

To explore what kinds of acclimation might be taking place, we carried out a sensitivity experiment focused on sunlight variation in a model with a rich vegetation parameter space, the Functionally Assembled Terrestrial Ecosystem Simulator (FATES). FATES is a terrestrial ecosystem model that simulates growth and competitive processes of plants to predict resulting functional differences in vegetation structure. FATES renders vegetation by size class, vertical canopy position, and sun- and shade-leaf fraction, making it a suitable test-bed for our hypotheses about long-term acclimation in canopy structures.

This chapter describes the model context and forcing data, compares the forcing data with *in situ* data from Rivendell, and reports on the results of the light-sensitivity experiment. We examine the forest composition, structure, water flux amount, and carbon- and water-use efficiencies resulting from the experimental runs, wherein we varied sunlight intensity. We draw comparisons with field data where possible, but acknowledge that further measurements are needed to constrain these comparisons, particularly in vegetation water fluxes.

6.2 Tools

6.2.1 FATES

FATES [30] is vegetation-focused model that can be run as a sub-module of the Community Land Model (CLM), which is the land surface component of NCAR's Community Earth System Model (CESM). FATES is based on the Ecosystem Demography concept, in which a traditional bulk canopy (i.e., big leaf, or two big leaves) model representation of vegetation is replaced with vegetation units structured with distinct size and age classes across plant functional types (PFTs). With these components, FATES aims to simulate economic and competitive processes approximating individual plant dynamics at the stand level. Notable past research with FATES focused on tropical forest ecosystems (e.g., the NGEE-tropics collaboration, https://ngee-tropics.lbl.gov/). Because parameterizations of vegetation processes can vary by species and biome, a past research focus on the tropics has made FATES especially suited to simulating those ecosystems. Mediterranean forest processes within FATES have been relatively less studied.

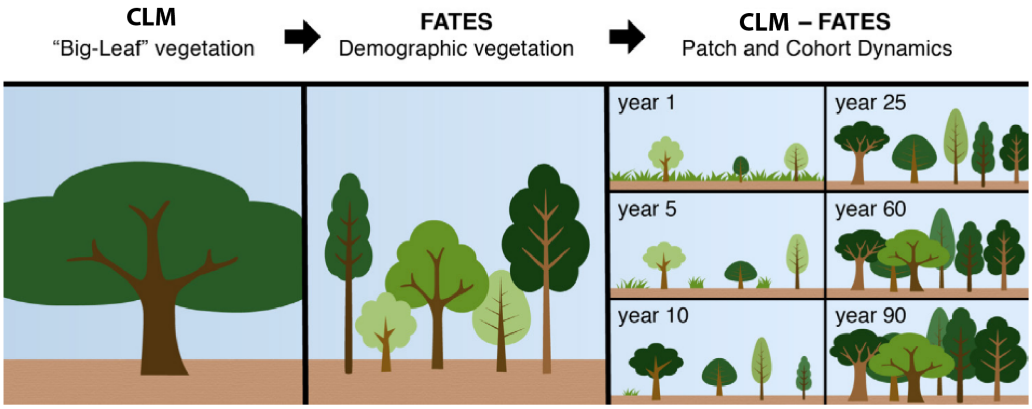

Figure 6.1: A comparison of complexity in model vegetation schemes, highlighting the added realism in forest structure rendered by FATES. Figure reproduced from US Department of Energy FATES Technical Highlight [9]

A challenge of working with process complexity in a model like FATES, which is focused on a system whose parameterizations are still a matter of active research, lies in interpreting results. Given that the encoded processes and their parameterizations are an approximation of certain processes within Earth's forests, FATES's forests can be thought of as forests on an 'alien planet' which resembles Earth in some useful ways, but not in every way. Determining whether phenomena of the 'alien planet' are relevant to forests on Earth is aided by the different modes in which FATES can be run. To tease apart the impacts of multiple interacting processes operating at different timescales, FATES can be run in modes that emphasize either fast vegetation processes or slow vegetation processes, by holding the other set artificially constant. Intercomparison among sets of runs with different settings can demonstrate which processes or sensitivities are governing the observed dynamics on the ‘alien planet’. FATES also has modes to interface directly with satellite observations, which can replace the model’s computation of evolving stand structure. In this mode, the model’s fast processes are anchored to real-world forest extents and stand structures, which change over time as the observations dictate.

In the exploratory research described in this chapter, we are running FATES in a default mode, with all processes operating. The forest structure is grown from bare earth, and not informed by satellite data. This mode is suitable for initial exploration of model dynamics, but does not provide results that fully address our research questions aimed at teasing out the mechanisms behind acclimation to microclimates.

6.2.1.1 Model Grid representation of forest

FATES operates within CLM. CLM’s processes begin with a gridcell, which is separated into different landunits characterized by a terrain type (e.g., lake, urban, crops, natural vegetation), which themselves can be broken into columns which can contain multiple functional units, such as soil or multiple plant functional types (PFTs). A FATES site starts with a CLM column that has vegetation, and further resolves that columns’ functional units (e.g., one particular PFT) into patches based on vegetation age. These patches, which are not spatially distributed, are then separated into cohorts based on the vegetation’s vertical position in the stand. FATES thus adds information about age classes and size classes, which offers greater resolution in simulating competition for resources for growth. Tree canopies follow the perfect plasticity approximation, and fully fill all gaps. This means that the top canopy layer fully intercepts incoming light, and the trees in the lower canopy layer (understory) all share an identically reduced light environment. Individual plants, and their associated biomass, can transfer whether they belong to the higher-light upper canopy layer or the lower-light understory layer through ‘promotion’ and ‘demotion’ as they grow taller or get crowded out by other individuals.

6.2.1.2 FATES PFTs and parameters:

FATES contains 12 distinct plant functional types (PFTs), including 6 types of tree, 3 types of shrub, and 3 types of grass. To approximate the forest composition of the north coast range in California, we ran our simulations with only three PFTs, all trees: extra-tropical broadleaf evergreen (BE), broadleaf cold-deciduous (BD), and extra-tropical needleleaf evergreen (NE) trees.

FATES's processes interface with 222 parameters. Some of these characterize the whole grid cell (e.g., soil salinity, or flags to indicate which processes are allowed to run). Others, such as an allometrically determined fraction of woody biomass that a plant keeps above ground vs. below ground, are specific to each PFT. Some of the parameters are unique to processes that exist in subroutines that can be toggled on and off, such as a mode with added hydraulic resolution (FATES-hydro), or a mode which simulates wildfire disturbance (FATES-spitfire).

Among the parameters which differentiate the PFTs, many have common values among the three PFTs used in our model runs, and only $\sim$20 parameters actually contained different values across these three types of tree. Of these differing parameters, the four that are likely to be the most important in differentiating competitive function among the three PFTs in our runs are leaf longevity, the maximum rate of carboxylation by rubisco ($V_{c,max}$), specific leaf area, and the slope parameter of the Medlyn stomatal conductance model (stomatal slope) [62, 30].

6.2.2 NLDAS-2 forcing data

The North American Land Data Assimilation System Phase 2 (NLDAS-2) [66] forcing data is a set of observation-based historical climate data, structured to match what climate models need as inputs to initialize their processes. The data set is derived from multiple observation sources, including satellite, land-based, and airborne measurements, with gaps in coverage interpolated by models. Its coverage extends over the contiguous united states at a spatial resolution of 1/8th degree, with hourly observations extending from 1979 to the present.

In our model runs, we used NLDAS-2 data extending from 1980 to 2018.

Because the year 2018 overlaps with the time period of ground-based observations in many of the same variables available from the Angelo Coast Range Reserve, we did a comparison to determine how well the NLDAS-2 data characterize the climate of our field site. We focused on the non-rainy month of June. Figure 6.2 shows the comparison.

The higher peaks of solar radiation and lower amplitude of daily temperature oscillation seen in the NLDAS-2 data may be characteristic of conditions higher in the atmosphere than our *in situ* measurement site, as higher elevation could indicate a lower atmospheric optical depth (accounting for higher radiation peaks), and greater distance from the earth's surface would reduce temperature fluctuation. Over the spatial resolution of NLDAS-2 data, the altitude variation around our hilly field site is substantial, so altitude-based differences between our *in situ* observations and an average representation of conditions for the whole region are plausible. It is less clear why the *in situ* humidity conditions stand out as noisier in our *in situ* observations, with a consistent mid-day dip in water vapor partial pressure. The NLDAS-2 data still appear to agree with the regional weather patterns recorded in the *in situ* data.

Whether this set of forcing data exactly matches what the vegetation at Angelo experience is not relevant to most of the work documented here, but could be relevant to interpreting our comparison of transpiration fluxes in the model forest in integration year 174 (receiving NLDAS-2 forcing from year 2018) and at our field site in 2018. To that end, we highlight that the combined differences in temperature and humidity result in substantive differences in VPD conditions between the NLDAS-2 data set and our field observations. The higher overnight VPD in NLDAS-2 could generate un-physical overnight vegetation water loss (>0.5 kPa VPD at night is considered to violate the assumption of zero-flow sap velocity conditions), while the lower evaporative demand in the daytime would underestimate vegetation water loss.

6.3 Light response experiment

Our first exploratory step involved a thought experiment to determine the sensitivity of vegetation stand structure, and hence water and carbon fluxes,

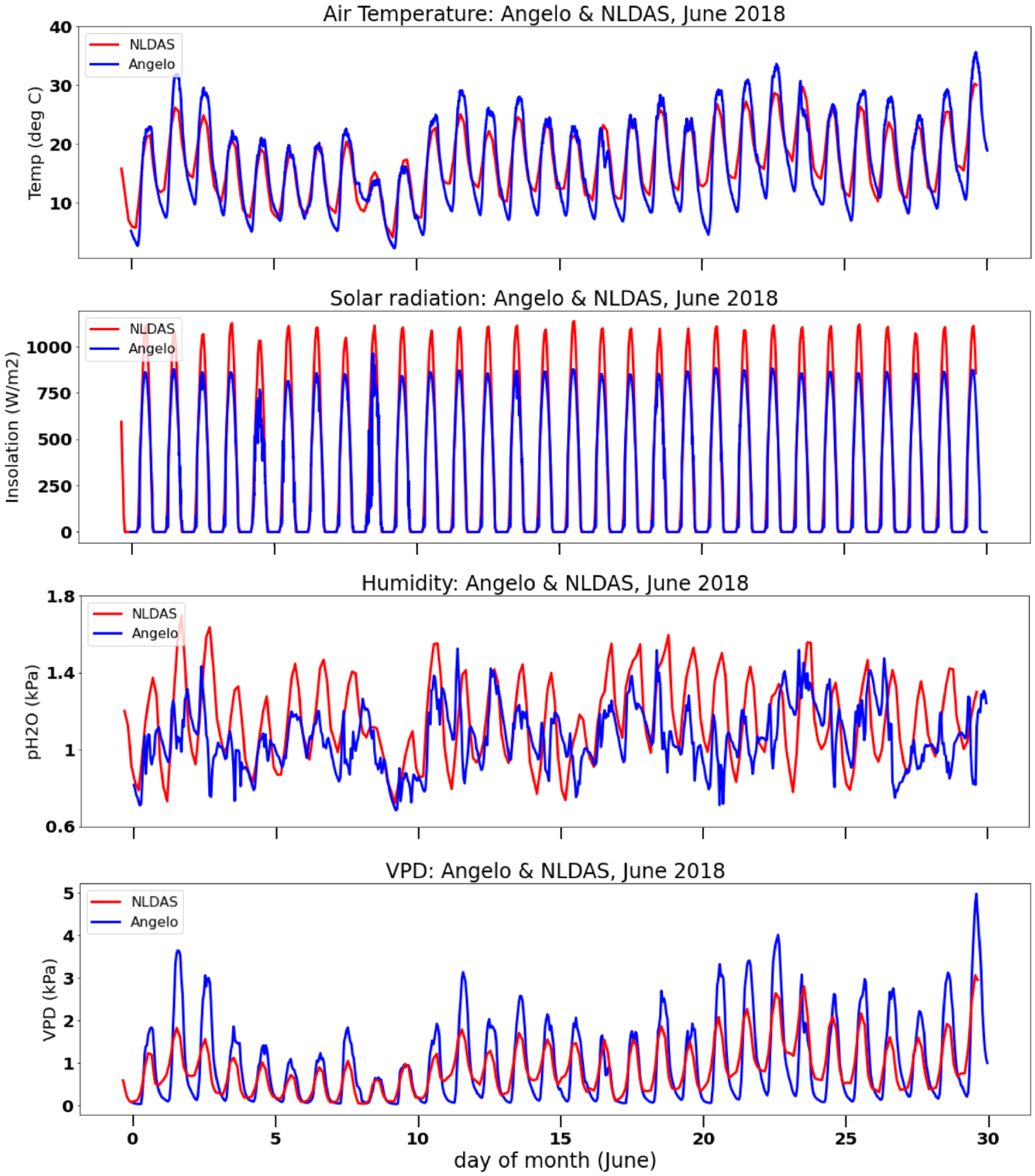

Figure 6.2: NLDAS data matches well with the ground-based observations at Angelo Coast Range Reserve during the month of June 2018.

to light gradients alone.

6.3.1 Methods

To carry out the light response sensitivity experiments, we selected the four NLDAS-2 grid points nearest to Angelo Coast Range Reserve (39.729°N, 123.644°W). These four points create a region 13.9 km (latitudinal distance) by 10.7 km (longitudinal distance), with our observational site roughly in the center. At each grid point, FATES simulated forest growth under three variations of solar forcing: the Standard case uses default NLDAS-2 solar radiation. The other two solar forcing cases multiply the Standard radiation by a factor derived from the ratio of clear-sky direct-beam light intensity for the geometry of the North and South slopes to that of a flat meadow (cf Figure 4.3 in chapter 4). This follows the procedure described in chapter 4.2.3.1. This produced simulated north- and south-slope radiation environments, which are substantially different year round (see figure 6.3). Because sunlight was the only aspect of the forcing that we perturbed, all other variables (e.g., air temperature, humidity, rain) at each grid point are the NLDAS-2 values, and are identical across the three different cases of solar forcing. Surface features, such as topography and soil texture and hydrological properties, derive from several sources documented in [5] and are also identical across the runs. Water quantity and distribution in the soils evolves in response to vegetation.

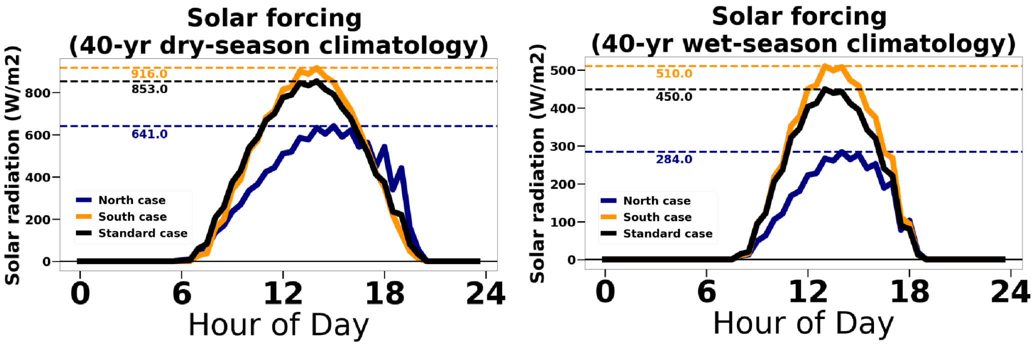

Figure 6.3: NLDAS-2 solar forcing was scaled to mimic the differences in direct-beam radiation received by the north and south slope field sites at Rivendell. Here, the differences between the cases are summarized as climatologies over 5 dry months (June-October) or 5 wet months (November-March).

The initial PFT distribution was the same for all four grid points, with three competing PFTs typical of mixed broadleaf-needleleaf evergreen forests of northern California's North Coast Range: broadleaf evergreen (BE), needleleaf evergreen (NE), and broadleaf deciduous (BD) trees. In total, we had 12 model runs (4 grid points x 3 cases of solar forcing). Each was run for 201 years, cycling 1980-2018 NLDAS data every 38 years, and allowing vegetation to grow from bare earth. To allow the resulting forest stands time to mature and reach near-steady-state, our analysis focuses on the last 40 years of the integrations.

All data explorations were done in python 3.8.5.

6.3.2 Results

6.3.2.1 Forest composition

Figure 6.4 shows that in all three cases, the BE PFT out-competed the NE and BD PFTs. These functional types coexist readily in northern Californian forests. We wondered if we would see NE trees have an advantage in the North case, given the prevalence of these trees on Rivendell's north slope and the scarcity on the south slope. Indeed, the NE trees are slightly more prevalent in the North case compared to the Standard or South cases, but are still largely out-competed by the BE trees. Ultimately, the simulations wound up producing near-exact PFT distributions, with BE trees comprising 99% of the South and Standard cases, and 98% of the North case.

Above-ground biomass (AGB) has identical dynamics to the summed-PFT biomass, but is slightly less, as the PFT biomass includes living below-ground biomass in its pools. The total AGB in the Standard solar case was slightly higher than in either of the two cases with perturbed solar radiation. In the final simulation year, the North case AGB is 91% of the Standard case, and the South case AGB is 97% of the Standard case.

FATES additionally breaks the AGB term into size classes defined by trunk diameter. Figure 6.5 shows that throughout the simulation, all cases have similar amounts of biomass in the smallest diameter (< 5cm) category. North case biomass lags behind South and Standard case biomass for medium-sized trees with stem diameters between 5 and 40 cm, and then for large trees with stem diameters between 40 and 100 cm all cases show oscillations in biomass over

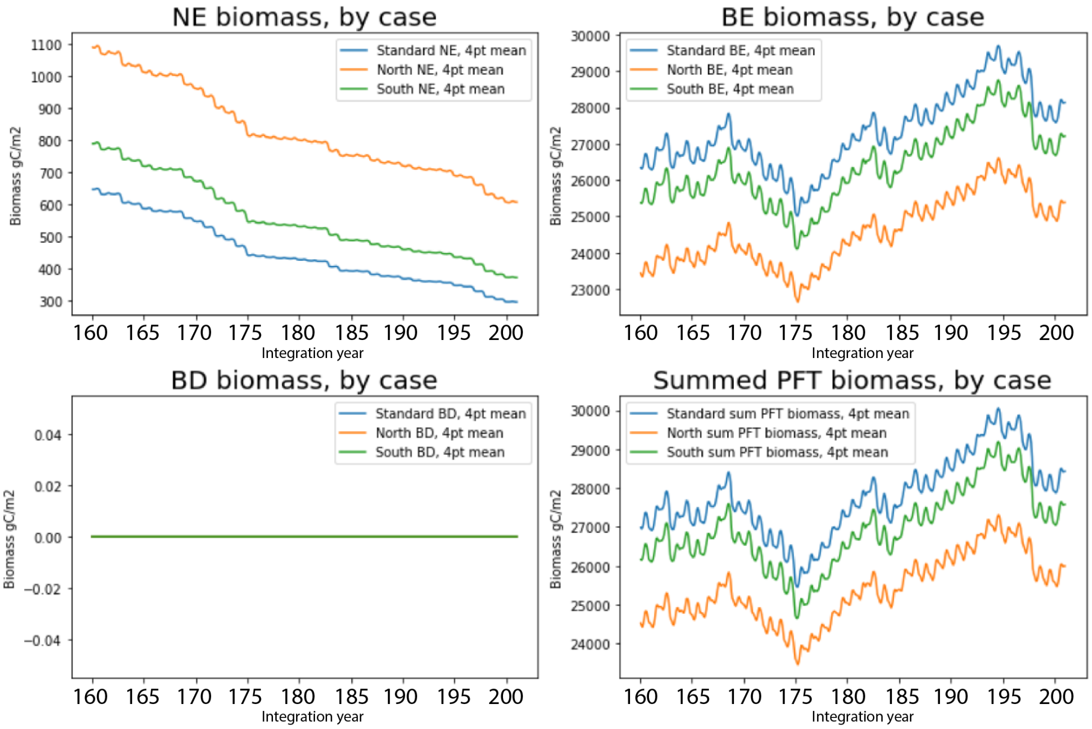

Figure 6.4: Total biomass for each plant functional type, averaged across the four simulation grid cells. Broadleaf deciduous (BD) trees had no biomass during this point in simulation, and needleleaf evergreen (NE) trees represented <2-3% of total biomass by the final year in each case. Total biomass is thus dominated by broad-leaved evergreen (BE) trees. The total biomass plotted here includes both above- and below-ground pools.

similar ranges of magnitude. The category that mainly drives the differences in AGB between the cases is the largest size class, containing trees with stems greater than 100 cm in diameter. In this category, the North case has less biomass than the South case, which has less biomass than the Standard case.

Figure 6.6 drives home the relative weight of the largest trees in determining the biomass differences by showing the relative biomass amounts in the final simulation year. Overall, the North and South cases both contain 15% of biomass in vegetation with stem diameters under 20 cm, 37% of biomass in vegetation with stem diameters between 20 and 100 cm, and 48% biomass in large trees with trunks greater than 1 m in diameter. The Standard case has a subtly different distribution with 15% of biomass in vegetation with stem diameters under 20 cm, 35% of its biomass in vegetation with stem diameters between 20 and 100 cm, and 50% of its biomass as large trees with trunks greater than 1 m in diameter.

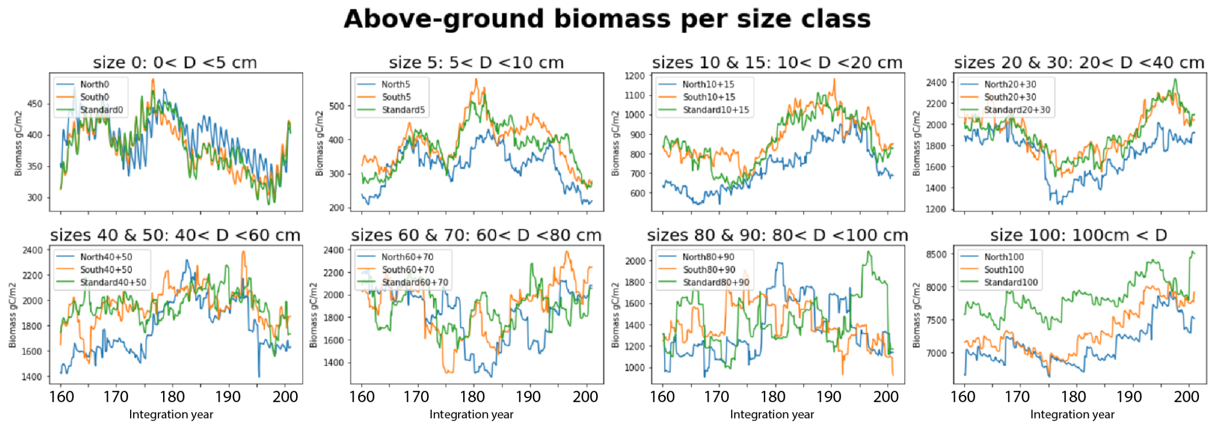

Figure 6.5: Above-ground biomass per size class, averaged across the four simulation grid cells, plotted for each case for the last 40 years.

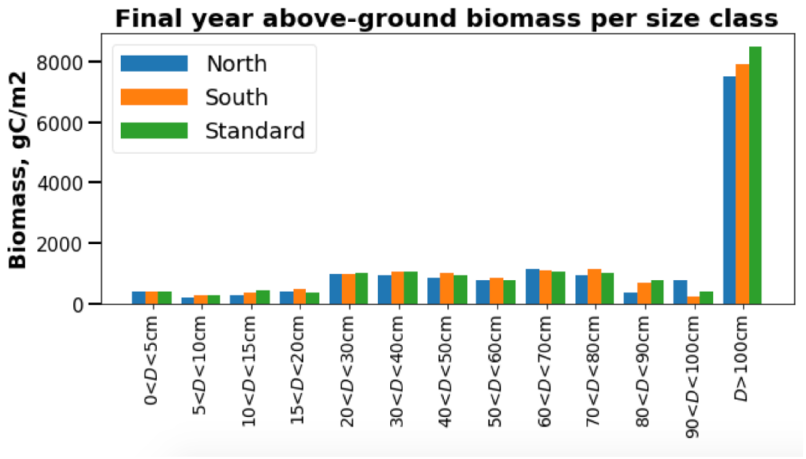

Figure 6.6: Above-ground biomass per size class, averaged across the four simulation grid cells, plotted for the ending year of the simulation in each case.

The forest stand evolves from competitive processes that hinge on a balance of recruitment and diverse sources of mortality. In our simulations, trees only died from carbon starvation, from “impact" disturbance (i.e., being blown over or otherwise crushed), or from a steady rate of background mortality not attributed to any particular cause (set at 1.4% for BE trees). Trees may also die of hydraulic, frost, fire, logging, or senescence mortality, but these did not occur in any of the cases. Figure 6.7 shows the annual cycles of mortality across the cases and size classes. The higher rates and longer seasonal duration of carbon starvation in the smaller size classes of the North case are consistent with a dimmer overall light environment. The fact that the largest size classes have lower rates of winter-time carbon starvation suggests that more of these large trees are canopy trees in the North case. This is also supported by the distribution of impact mortality, which only affects understory trees. The higher rates of impact mortality in the South and Standard cases suggests a denser population of understory trees in these cases. Despite equivalent size class distributions of biomass between North and South cases, the North case may have acclimated to the lower light regime by thinning the understory and concentrating its biomass in canopy trees. Future investigations of how the fraction of understory vs canopy trees evolved in each case will help elucidate the causes behind these different rates of mortality.

The total quantity of basal area that evolved in the model ($\sim$60 m^2/ha) seems to represent a reasonable match with the Angelo Reserve forest based on our field experience. Unfortunately, basal area was not a variable we explicitly measured during our field campaign, in part because plans for further measurements in Spring 2020 were disrupted by the COVID pandemic. This spatial density of basal area represents $\sim$4.8 trees 40 cm in diameter over a 10 x 10 m area, if all basal area were accounted for by this size class alone. Figure 6.8 shows a schematic of basal area as if it were all occurring in trees with diameter 40 cm, and contrasts this with a photograph of trees under observation in the forest which are each $\sim$30-40 cm in diameter. Our field experience (and photographs, e.g., figure 6.8) suggests that the size class distribution may overemphasize small and large trees and under-emphasize medium-sized trees, but lacking observations of size class distribution at our site, we cannot be more specific.

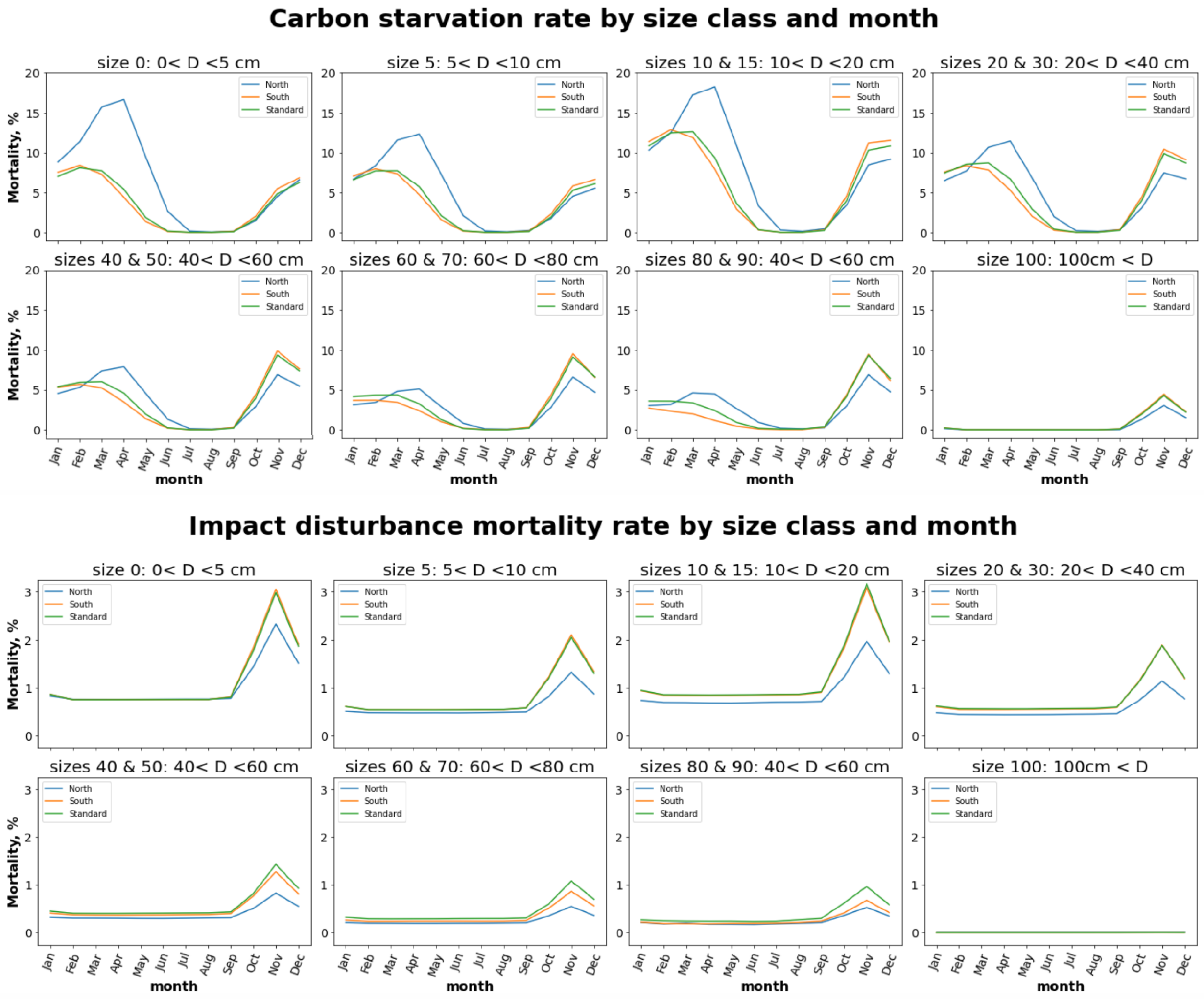

Figure 6.7: Carbon starvation and impact mortality were the two chief causes of mortality across all three cases. The 40-yr average annual cycles plotted here show the variation in mortality between the cases and size classes, across the months of the year.

6.3.2.2 Contrast with sap flow observations

The transpiration variable reported by FATES is not directly comparable to the sap flow observations in the field. To undertake a comparison between the sap flow observations described in chapters 2, 3 and 4 and FATES' transpiration variable, shifts of scale resting on loosely constrained assumptions must be made. We explore this to the extent that our field observations permit, and

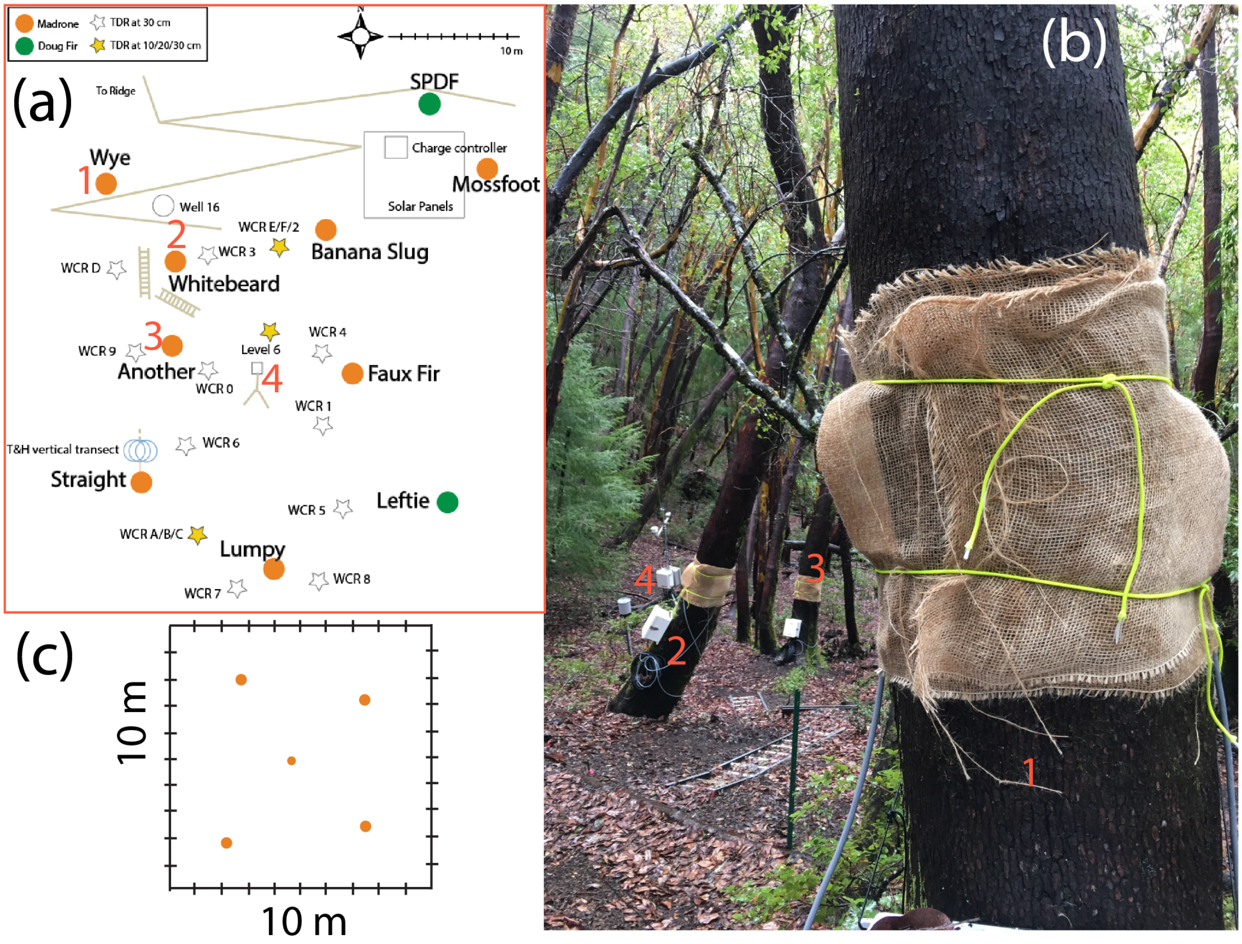

Figure 6.8: Lacking measurements of basal area, we reviewed photographs to understand whether the model's estimate of basal area was roughly representative for our field site. A map showing the relative distances between the trees (trunk sizes exaggerated) on the south slope of the Rivendell field site (panel a) helps to contextualize the photograph of south slope installations in panel (b). Tree 'Wye' (feature 1) is 8 m from tree 'Whitebeard' (feature 2), 13 m from tree 'Another', and 20 m from the Level 6 weather station (feature 4). The trunks are 30-40 cm in diameter, hosting white enclosures that are 20 x 25 cm. Panel (c) shows a schematic of the basal area reported by the model as if it were all represented by 35-40 cm diameter trees.

highlight where further observations would enable a better comparison.

Figure 6.9 demonstrates the steps and assumptions necessary to derive a sap velocity from FATES transpiration. FATES reports canopy transpiration over the whole grid cell (figure 6.9, top row). Limiting this to the basal area reported by FATES transforms this into an average sap velocity, if all the basal area were sapflow (figure 6.9, second row). From this point on, the velocity can be scaled to a nearly arbitrary extent based on assumptions of sapwood area (figure 6.9, third row) or the radial profile of sap flux density (figure 6.9, bottom row).

Because our sap velocity observations in Rivendell madrone trees (sized 36-72 cm in diameter) included measurements at two radial depths (15 mm and 70 mm), we can constrain hypotheses of the sapwood area and radial profile to a limited extent. Comparison of outer to inner junction flows across individuals reveals that trees exhibit a circumferentially variable depth of actively flowing sapwood. At some installation sites, the inner junction is approximately non-flowing, while at others, inner junction flows are as large as those reported at the outer junction. In most cases, inner junction flows were substantially lower than outer junction flows, and inner junction flows that are larger than outer junction flows did not occur in madrone trees. Figure 6.10 shows that, in the whole-site average, the average daily cycle over summer 2018 has 70 mm flows reaching up to 35% of that observed at 15 mm, at the moment of maximum daily flow. From this we can hypothesize that, if the velocity is linearly declining between 15 mm and 70 mm, zero flows would be reached at 100 mm, on average. This is illustrated in our sapwood area hypothesis in figure 6.9. We can also hypothesize that 15 mm velocities could be approximately double an equivalent rate of flow that was equal over the entire sapwood area. This is illustrated in the hypothesis of radial distribution of sap flux density in figure 6.9.

Figure 6.11 shows that, under the hypotheses of sapwood area and radial distribution of sap flux density, the peak magnitude of FATES transpiration reinterpreted as sap velocity matches well with the peak magnitude of our field observations. The peak 'sap velocity' in the average summer daily cycle reported by FATES is 7 cm/hr, while the peak sap velocity in the average summer daily cycle observed at Rivendell is 10 cm/hr.

We repeat the caveat from chapter 2 that the unquantified differences in the thermal properties of wood at the two radial depths renders quantitative comparisons of sap velocity magnitudes between the two depths uncertain,

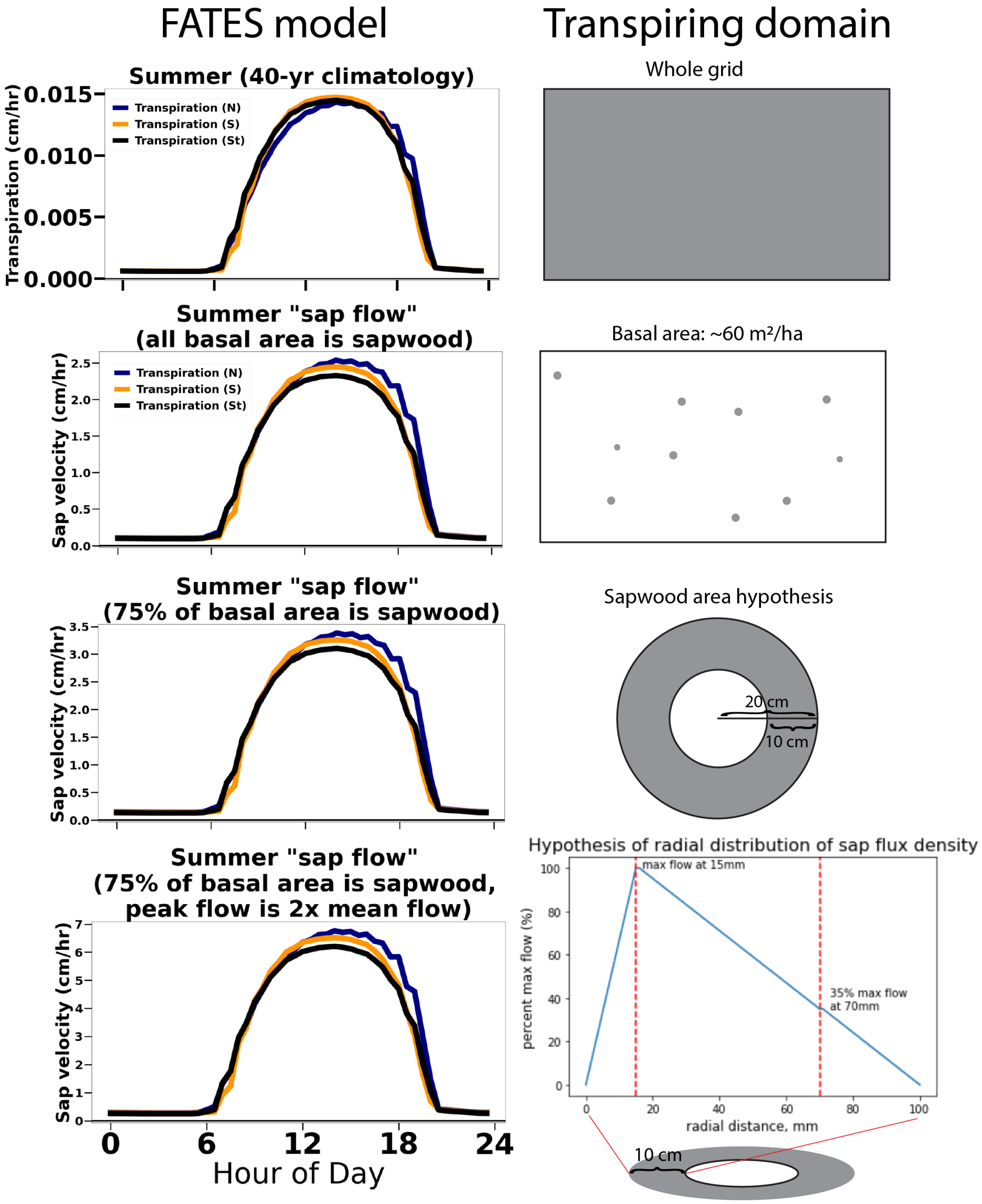

Figure 6.9: An illustration of the assumptions feeding into a derivation of sapflow from FATES canopy transpiration. At left, curves in the top and second row plots evolve due to differences in basal area among cases, but differences among rows 2-4 exist only in the scale of the y-axis, as the assumptions evolve.

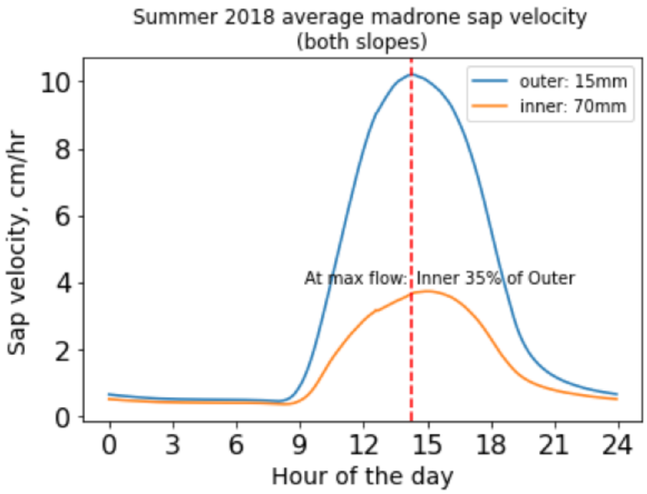

Figure 6.10: Averaging velocities from all sensors in madrone trees (both north and south slopes) shows the seasonal average daily cycle for summer 2018. At the moment of maximum sap velocity, the inner junction velocity is about 35% of the outer junction velocity.

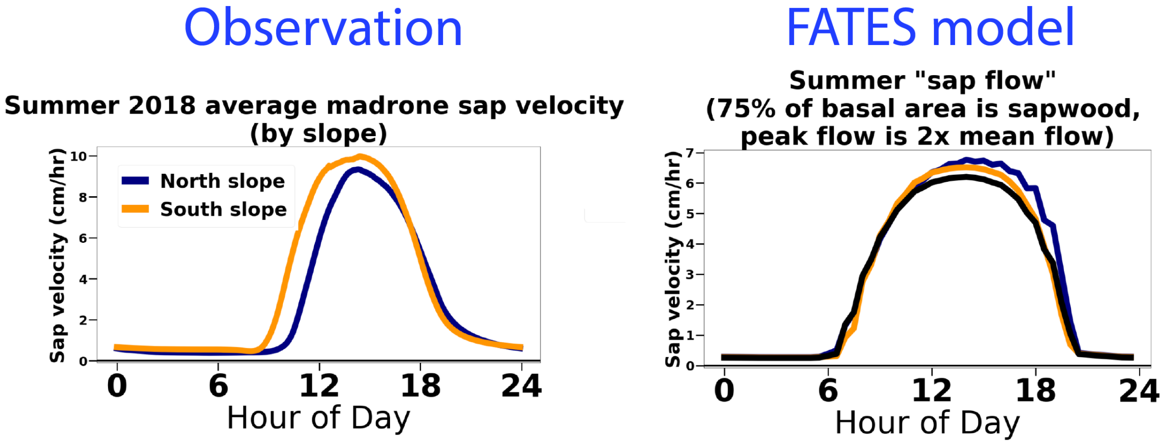

Figure 6.11: A comparison between re-scaled FATES transpiration and sap velocity observations shows good agreement in peak velocities. The FATES climatology is computed over 40 years of model output, while the Rivendell climatology is only for a single summer.

when using identical parameters for the Granier equation. Tree cores that measured fresh wood heat capacity by radial depth would be useful in bolstering a quantitative comparison of flow rates at these two depths. Tree cores could also further constrain the proportion of basal area which is sapwood.

To compare the seasonal timing of sap velocity, we focus on model integration year 174, which received NLDAS-2 forcing data from 2018, and compare this to our field observations. The field observations of sap velocity only begin in June of 2018, although the timeseries begins earlier. Figure 6.12 shows the comparison.

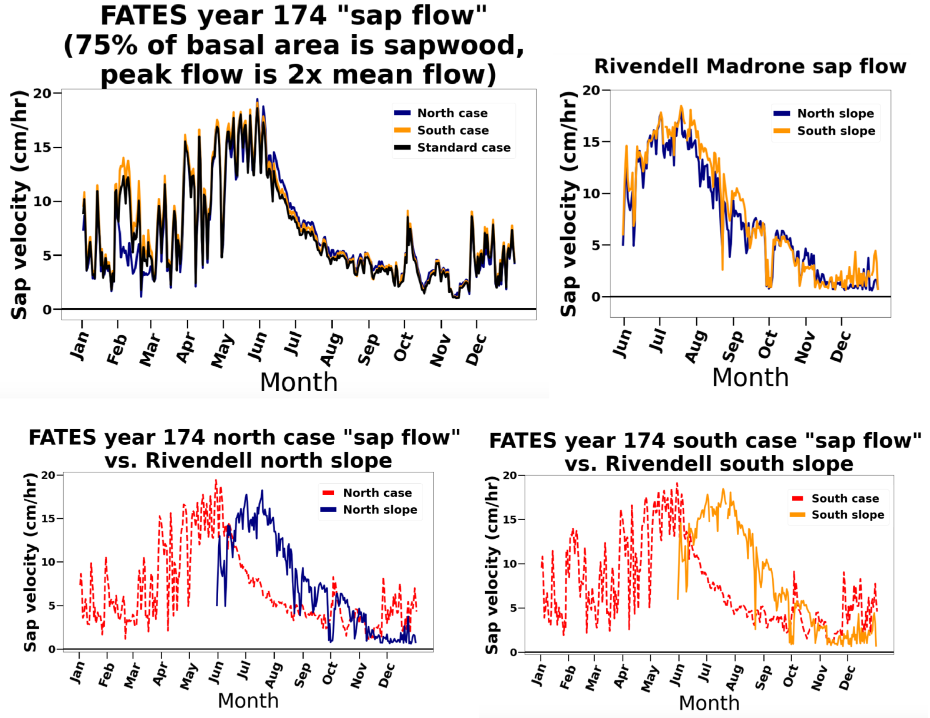

Figure 6.12: A comparison between re-scaled FATES transpiration for integration year 174, which received NLDAS-2 forcing from 2018, and Rivendell sap velocity observations from 2018, shows the different seasonal timing of sap velocity decline.

The comparison shows that FATES vegetation has an earlier seasonal peak in sap velocity by about 1.5 months and a steeper decline in daily maxima, followed by larger daily maximum sap velocities over the winter. For context, in figure 6.13 we also show the comparison in soil moisture conditions between the model and Rivendell over the same time period. The quantity and distribution of soil moisture are near-identical across all runs, so we report only the Standard case. The soils in the ‘alien forest’ are notably wetter over the summer and have an overall less extreme seasonal cycle, but show a good match in seasonal timing of moisture decline.

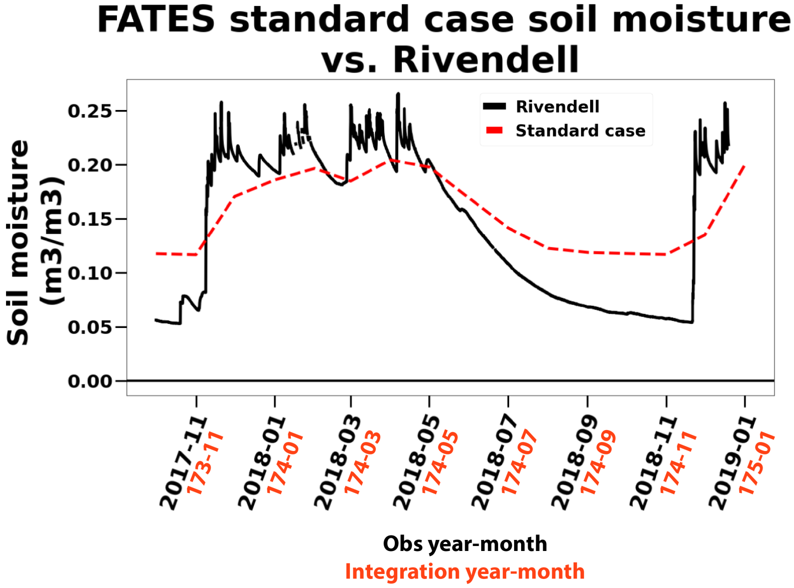

Figure 6.13: FATES soil moisture (reported monthly), averaged between 26 cm and 40 cm depths, from November of integration year 173 through the end of integration year 174 is shown in dotted red. These integration years correspond to NLDAS-2 forcing from 2017-2018. Rivendell soil moisture (15-min frequency) from 30 cm depth over the same time period is shown in black.

The seasonal offset in 6.12 may be indicating a different interaction with subsurface moisture, potentially arising from either representations of water supply, vegetation access to water supply (i.e. rooting depths), or vegetation sensitivity to water supply. Alternatively, it may arise from phenological aspects that are uncaptured by FATES BE trees. Madrone trees were chosen for our field study in part because of their unusually late transpiration peak, which may be in part caused by their phenological cycle of leaf turnover (leaf lifespan 14 months). We did not measure LAI in the field, but we infer from the phenology that LAI evolves seasonally and is maximized in the midsummer months when the new leaves are flushed and the old leaves beginning to drop. Future investigations will explore these aspects.

Figure 6.14: Madrone trees are evergreen, but nonetheless drop their leaves each year. Old and new leaves coexist in their canopies during the early summer months. Though at Rivendell the madrones dropped most of the previous year's leaves by the autumn, there is variation in leaf life span. This photograph showing both old and new leaves in madrone, alongside flowering, was taken in March 2020 at Friday Harbor (photo credit: Inez Fung).

In sum, the 'alien forest' of FATES BE trees has a comparable basal area as a BE-dominated region of our Earth forest (i.e., Rivendell's madrone-dominated south slope, seen in figure 6.8); it may transpire water at a comparable rate, sensitive to assumptions about sapwood area and radial sap flux distribution; and it has different seasonality of transpiration, despite having a similar seasonality of soil moisture decline. Figure 6.11 highlights that the model's summertime results do not, in the presence of comparable light differences alone, show the same degree of transpiration offset between the north and south cases as the observations show between the north and south slopes.

6.3.2.3 Transpiration sensitivity

Figure 6.15 shows that, during the dry summer season months, there is surprisingly little to no difference in daily integrated transpiration between the North and South solar radiation cases. This is contextualized by differences between the two cases in peak radiation received ($\sim$30% higher in the South case) and amount of biomass in the forest stands ($\sim$6% higher in the South case). The South case has a diurnal cycle of transpiration shifted slightly earlier than the

North case, as would be expected by the later sunrise and sunset in the North case (see figure 6.3). However, both the North and South cases show lower transpiration than the Standard case. In sum, despite being exposed to dimmer light and having less biomass, the North case forest stand is equally active over the summer.

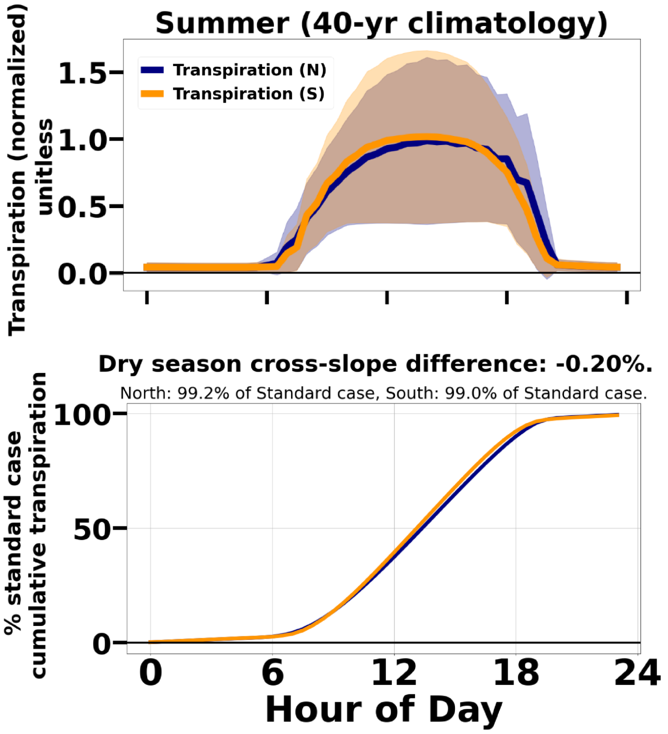

Figure 6.15: Over the dry summer, there was essentially no difference in transpiration between the two light environments.

Figure 6.16 shows substantial differences in transpiration in the wet winter. The markedly lower amount of solar radiation received during the winter at this latitude (39.7°N) likely placed all solar radiation cases into a light-limited transpiration regime, contrasting with the summertime results which suggested that light limitation was absent in all cases.

6.3.2.4 GPP differences

Figure 6.17 shows that dry season GPP is ∼5% higher in the North case than the South case, despite the comparatively lesser biomass (∼6% lower than the

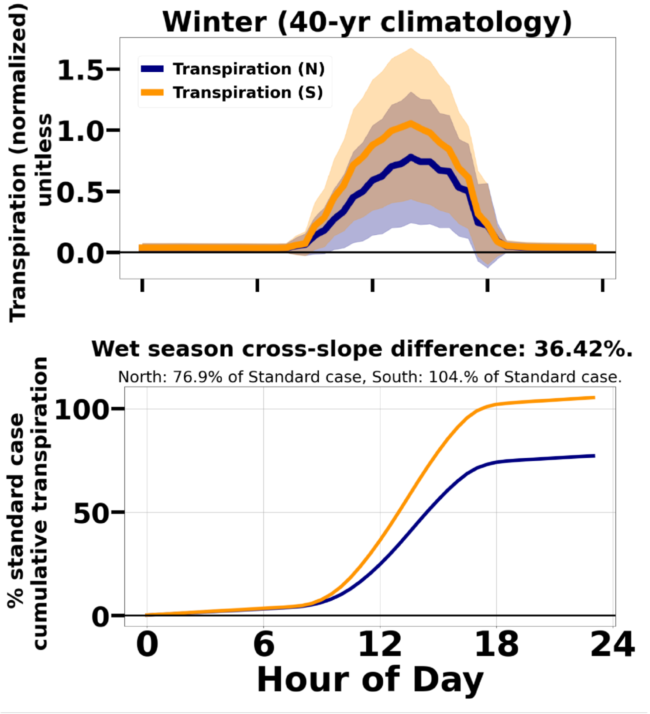

Figure 6.16: Over the rainy winter, transpiration on the sunnier south-facing slope was roughly 36% higher, suggesting that the model forest was experiencing light-limited transpiration conditions.

South case). Mirroring the transpiration results, figure 6.18 shows that winter GPP is lower under North case conditions, although the differences among the cases are less pronounced in GPP than in transpiration.

6.3.2.5 Leaf differences

Given that the differences in transpiration and GPP among the cases do not track with differences in biomass amount, we examined leaf distribution differences as well. Figure 6.19 shows that differences in Leaf Area Index (LAI) among the three cases matches the direction of differences in above ground biomass, but they are smaller than the differences in biomass. The North case has 91% of the Standard case biomass but 93% of the LAI; similarly, the South case has 97% of the Standard case biomass but 99% of the LAI. The sun leaf fraction was relatively invariant among the three cases, despite the stark dif-

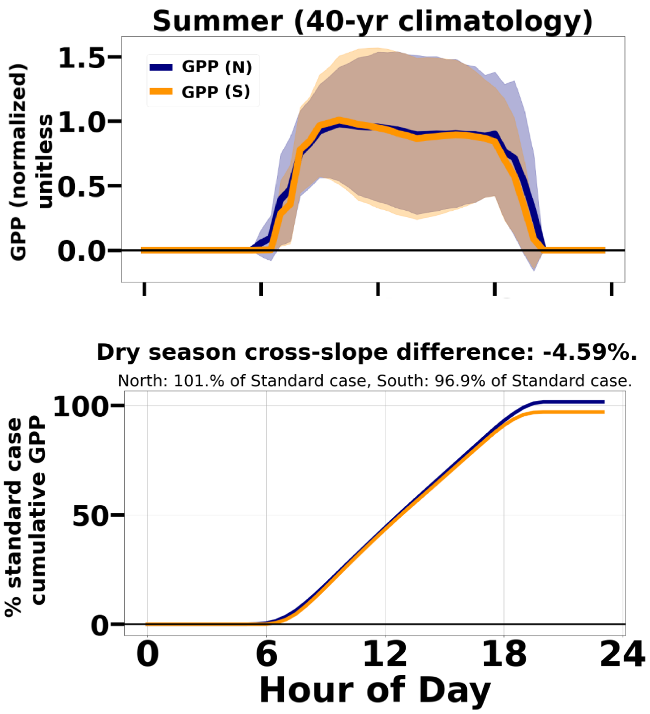

Figure 6.17: Over the dry summer, GPP in the dimmer North case was ∼5% higher than the South case. The North case GPP also narrowly exceeds the Standard case GPP, which is surprising in light of the fact that the Standard case has ∼9% greater biomass than the North case.

ferences in solar radiation. Sun leaf fraction was, in fact, lower in the South case (7.9%) than in the North case (8.3%), with the Standard case falling in between (8.0%). This could be consistent with the hypothesis put forth in section 6.3.2.1 that the North case has equivalent canopy biomass (and LAI), but lesser understory biomass (and LAI).

6.3.2.6 Plasticity in light- and water-use efficiency:

Figure 6.20 highlights the different light- and water-use efficiencies that emerge between the North and South cases, and also seasonally. The North case achieves a light-use efficiency nearly 60% higher than the Standard and South cases from 10am-noon during the summer, and 40% higher over the winter. The water-use efficiency differences show a smaller-scale version of the same

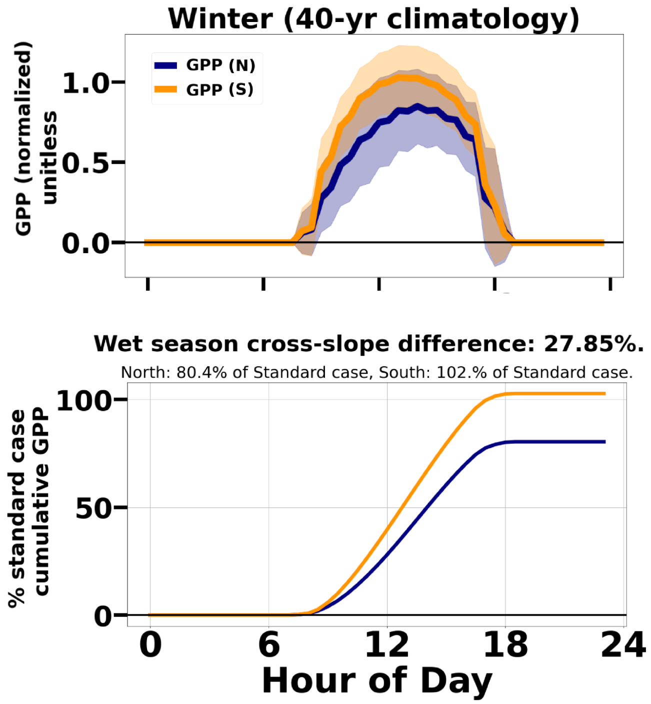

Figure 6.18: Over the rainy winter, GPP in the dimmer North case is 28% lower than that in the South case.

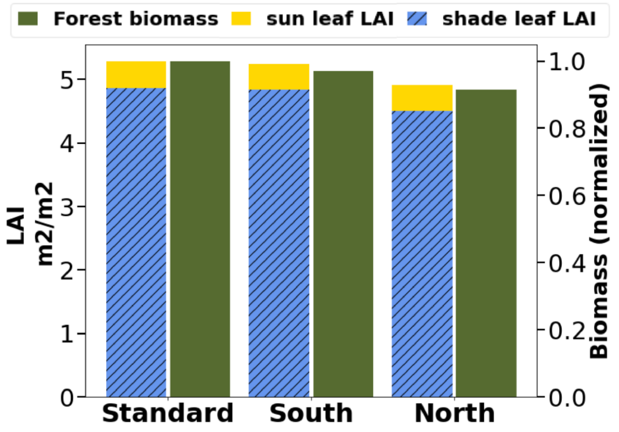

Figure 6.19: LAI is highest in the Standard case and lowest in the North case, roughly agreeing with differences in biomass among the cases.

pattern, with water-use efficiency 6% higher in the North case over the summer, and 10% higher over the winter.

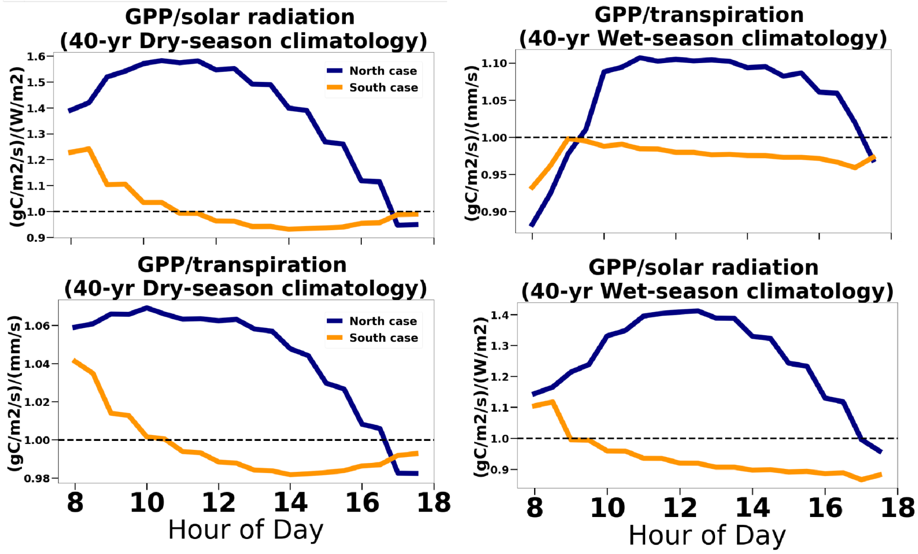
GPP/solar radiation (40-yr Dry-season climatology)

GPP/transpiration (40-yr Wet-season climatology)

GPP/transpiration (40-yr Dry-season climatology)

GPP/solar radiation (40-yr Wet-season climatology)

Figure 6.20: Light- and water-use efficiencies are computed for the North and South cases, and then scaled to the Standard case to highlight the impact of the different light regimes. The North case exhibits higher light-use and water-use efficiencies, both in summer and winter.

6.3.3 Discussion & future directions

These results demonstrate the thresholds of light limitation shaping the forest. In stands of identical plant functional types (extra-tropical broadleaf evergreen trees) with similar, though not identical, standing biomass and leaf area, lower transpiration and GPP is only associated with the dimmer light regime under a certain threshold. This threshold is triggered over the wintertime, but not the summertime. In fact, under the parameters of model vegetation, the summertime growth conditions in the dimmer North case appear favored in broadleaf evergreen trees. As VPD and soil moisture conditions are the same among all simulations, the results suggest that model vegetation is not energy/light limited even under relatively dim North slope summertime conditions.

It remains to be explored why the North case, with lower biomass and lower LAI, would both fix more carbon and release more water than the South or Standard cases. Speculatively, we hypothesize that the differences in transpiration, GPP, light-use efficiency, and water-use efficiency are caused by evolved differences in stand structure among the cases– the slow processes of FATES. Perhaps a denser understory evolved in the brighter South and Standard cases, and the additional competition for resources was detrimental to the performance of the canopy trees. Additional model runs holding either fast or slow processes constant could expand the scope of the thought experiment, the beginning stages of which are outlined in this chapter, to confirm or disprove this. For instance, if the differences are driven by the reactions of fast processes to the differences in light conditions between the cases, that may imply that the South case is too bright, and has triggered photolimitation or a similar growth restriction. If this is instead driven by the slow process of differently evolving stand structure, it may be demonstrating that even subtly-different distributions of biomass throughout the various size classes and canopy layers between the two cases can lead to substantive functional differences emerging at the stand level, even under identical functional parameters. In particular, if slow processes explain the the higher water-use efficiency and light-use efficiency seen in North case, this suggests a high sensitivity of these properties to variation in leaf area and stand structure (size class distribution), even with the same parameters describing the stomatal function of individuals. This may indicate that more complex and hence accurate representations of forest structure, for instance including the possibility of emergent tall trees whose crowns do not touch in an overstory layer over a closed canopy of smaller trees, would enable more accurate depictions of a forest's environmental sensitivities, carbon and water fluxes.

6.3.4 Conclusions

The model vegetation response to light differences in FATES demonstrates several capabilities of the model, and refines our future questions. We see that once light limitation is triggered in the wintertime, there are commensurate declines in water usage in the dimmer environment. We also observed that the model shows consistently higher light- and water-use efficiency in the dimmer tree population, both in summer and in winter. This runs counter to the speculative interpretations of the analysis in 5, which suggested that the dimmer population's water-use dynamics could be explained in part by lower water use efficiencies. Future investigations will explore mechanistic explanations for the differences among the solar forcing cases, which will, in turn, provide further basis for our interpretations of mechanisms at play in the field observations.

Bibliography

[1] Elizabeth A. Ainsworth and Stephen P. Long. “What have we learned from 15 years of free-air CO2 enrichment (FACE)? A meta-analytic review of the responses of photosynthesis, canopy properties and plant production to rising CO2”. In: *New Phytologist* 165.2 (2005), pp. 351–372. DOI: `https://doi.org/10.1111/j.1469-8137.2004.01224.x`. URL: `https://nph.onlinelibrary.wiley.com/doi/abs/10.1111/j.1469-8137.2004.01224.x`.

[2] C. Amitrano et al. “Vapour pressure deficit: The hidden driver behind plant morphofunctional traits in controlled environments”. In: *Annals of Applied Biology* 175.3 (2019), pp. 313–325.

[3] J. J. Armesto and J. A. Martinez. “Relations Between Vegetation Structure and Slope Aspect in the Mediterranean Region of Chile”. In: *Journal of Ecology* 66.3 (1978), pp. 881–889.

[4] Gregory P. Asner et al. “Progressive forest canopy water loss during the 2012–2015 California drought”. In: *Proceedings of the National Academy of Sciences* 113.2 (2016), E249–E255. DOI: `10.1073/pnas.1523397113`.

[5] University Center for Atmospheric Research (UCAR). *CLM5.0 Technical Note*. 2020. URL: `https://escomp.github.io/ctsm-docs/versions/release-clm5.0/html/tech_note/index.html`.

[6] M. Betancourt. “A conceptual introduction to Hamiltonian Monte Carlo”. In: *arXiv preprint arXiv:1701.02434* (2017).

[7] T. E. Bilir. “Data and Software accompanying "Slope-aspect induced climate differences influence how water is exchanged between the land and atmosphere"”. In: (2020). DOI: `10.5281/zenodo.3996308`. URL: `https://doi.org/10.5281/zenodo.3996308`.

[8] T. Eren Bilir, Inez Fung, and Todd E. Dawson. "Slope-Aspect Induced Climate Differences Influence How Water Is Exchanged Between the Land and Atmosphere". In: *Journal of Geophysical Research: Biogeosciences* 126.5 (2021), e2020JG006027. DOI: https://doi.org/10.1029/2020JG006027. URL: https://agupubs.onlinelibrary.wiley.com/doi/abs/10.1029/2020JG006027.

[9] DOE Office of biological and environmental research. *FATES: THE E3SM FUNCTIONALLY-ASSEMBLED TERRESTRIAL ECOSYSTEM SIMULATOR*. 2019. URL: https://e3sm.org/wp-content/uploads/2019/01/FATES_Highlight_01-30-18b.pdf.

[10] N. K. Boardman. "Comparative photosynthesis of sun and shade plants". In: *Annual review of plant physiology* 28.1 (1977), pp. 355–377.

[11] D. Bolton. "The computation of equivalent potential temperature". In: *Monthly weather review* 108.7 (1980), pp. 1046–1053.

[12] Erin S. Brooks, Jan Boll, and Paul A. McDaniel. "A hillslope-scale experiment to measure lateral saturated hydraulic conductivity". In: *Water Resources Research* 40.4 (2004). DOI: https://doi.org/10.1029/2003WR002858. URL: https://agupubs.onlinelibrary.wiley.com/doi/abs/10.1029/2003WR002858.

[13] J Renee Brooks et al. "Hydraulic redistribution in a Douglas-fir forest: Lessons from system manipulations". In: *Plant, cell environment* 29 (Feb. 2006), pp. 138–50. DOI: 10.1111/j.1365-3040.2005.01409.x.

[14] J. R. Brooks et al. "Hydraulic redistribution in a Douglas-fir forest: lessons from system manipulations". In: *Plant, Cell & Environment* 29.1 (2006), pp. 138–150.

[15] J. R. Brooks et al. "Hydraulic redistribution of soil water during summer drought in two contrasting Pacific Northwest coniferous forests". In: *Tree physiology* 22.15-16 (2002), pp. 1107–1117.

[16] Holger Brueck. "Effects of nitrogen supply on water-use efficiency of higher plants". In: *Journal of Plant Nutrition and Soil Science* 171.2 (2008), pp. 210–219. DOI: https://doi.org/10.1002/jpln.200700080.

URL: https://onlinelibrary.wiley.com/doi/abs/10.1002/jpln.200700080.

[17] Stephen S. O. Burgess et al. "An improved heat pulse method to measure low and reverse rates of sap flow in woody plants." In: *Tree physiology* 21 (2001), pp. 589–98.

[18] J.G. Canadell et al. "Global Carbon and other Biogeochemical Cycles and Feedbacks". In: *Climate Change 2021: The Physical Science Basis. Contribution of Working Group I to the Sixth Assessment Report of the Intergovernmental Panel on Climate Change*. Ed. by V. Masson-Delmotte et al. Cambridge, United Kingdom and New York, NY, USA: Cambridge University Press, 2021. Chap. 5, pp. 673–816. DOI: https://doi.org/10.1017/9781009157896.007.

[19] F. Stuart Chapin et al. "Plant Responses to Multiple Environmental Factors". In: *BioScience* 37.1 (1987), pp. 49–57.

[20] F Stuart Chapin III et al. "Changing feedbacks in the climate–biosphere system". In: *Frontiers in Ecology and the Environment* 6.6 (2008), pp. 313–320. DOI: https://doi.org/10.1890/080005. URL: https://esajournals.onlinelibrary.wiley.com/doi/abs/10.1890/080005.

[21] Pieter De Frenne et al. "Global buffering of temperatures under forest canopies". In: *Nature Ecology & Evolution* 3 (5 2019), pp. 744–749. DOI: 10.1038/s41559-019-0842-1. URL: https://doi.org/10.1038/s41559-019-0842-1.

[22] Pieter De Frenne et al. "Microclimate moderates plant responses to macroclimate warming". In: *Proceedings of the National Academy of Sciences* 110.46 (2013), pp. 18561–18565. ISSN: 0027-8424. DOI: 10.1073/pnas.1311190110. eprint: https://www.pnas.org/content/110/46/18561.full.pdf. URL: https://www.pnas.org/content/110/46/18561.

[23] H. Douville et al. "Water Cycle Changes." In: *Climate Change 2021: The Physical Science Basis. Contribution of Working Group I to the Sixth Assessment Report of the Intergovernmental Panel on Climate Change.* Ed. by V. Masson-Delmotte et al. Cambridge, United Kingdom and New York, NY, USA: Cambridge University Press, 2021. Chap. 8, pp. 1055–1210. DOI: https://doi.org/10.1017/9781009157896.010..

[24] J. A. Duffie and W. A Beckman. *Solar engineering of thermal processes John Wiley & Sons*. John Willey & Sons, 1991.

[25] V. Eyring et al. “Human Influence on the Climate System.” In: *Climate Change 2021: The Physical Science Basis. Contribution of Working Group I to the Sixth Assessment Report of the Intergovernmental Panel on Climate Change*. Ed. by V. Masson-Delmotte et al. Cambridge, United Kingdom and New York, NY, USA: Cambridge University Press, 2021. Chap. 3, pp. 423–552. DOI: https://doi.org/10.1017/9781009157896.005..

[26] Ying Fan et al. “Hydrologic regulation of plant rooting depth”. In: *Proceedings of the National Academy of Sciences* 114.40 (2017), pp. 10572–10577. DOI: 10.1073/pnas.1712381114. URL: https://www.pnas.org/doi/abs/10.1073/pnas.1712381114.

[27] R.A. Feddes, P.J. Kowalik, and H. Zaradny. *Simulation of field water use and crop yield John Wiley and Sons*. New York, NY: John Wiley and Sons, 1978.

[28] Christopher J. Fettig et al. “Tree mortality following drought in the central and southern Sierra Nevada, California, U.S.” In: *Forest Ecology and Management* 432 (2019), pp. 164–178. DOI: https://doi.org/10.1016/j.foreco.2018.09.006.

[29] C. Field, J. Merino, and H.A. Mooney. “Compromises between water-use efficiency and nitrogen-use efficiency in five species of California evergreens”. In: *Oecologia* 60.3 (1983), pp. 384–389.

[30] R. A. Fisher et al. “Taking off the training wheels: the properties of a dynamic vegetation model without climate envelopes, CLM4.5(ED)”. In: *Geoscientific Model Development* 8.11 (2015), pp. 3593–3619. DOI: 10.5194/gmd-8-3593-2015. URL: https://gmd.copernicus.org/articles/8/3593/2015/.

[31] P. Friedlingstein et al. “Global Carbon Budget 2020”. In: *Earth System Science Data* 12.4 (2020), pp. 3269–3340. DOI: 10.5194/essd-12-3269-2020. URL: https://essd.copernicus.org/articles/12/3269/2020/.

[32] B. O. Gimenez et al. "Species-Specific Shifts in Diurnal Sap Velocity Dynamics and Hysteretic Behavior of Ecophysiological Variables During the 2015–2016 El Niño Event in the Amazon Forest". In: *Frontiers in Plant Science* 10 (2019), p. 830. ISSN: 1664-462X. DOI: 10.3389/fpls.2019.00830. URL: https://www.frontiersin.org/article/10.3389/fpls.2019.00830.

[33] N. Gorelick et al. "Google Earth Engine: Planetary-scale geospatial analysis for everyone". In: *Remote Sensing of Environment* (2017). DOI: 10.1016/j.rse.2017.06.031. URL: https://doi.org/10.1016/j.rse.2017.06.031.

[34] A. Granier. "Evaluation of transpiration in a Douglas-fir stand by means of sap flow measurements". In: *Tree physiology* 3.4 (1987), pp. 309–320.

[35] A. Granier. "Une nouvelle méthode pour la mesure du flux de sève brute dans le tronc des arbres". In: *Annales des Sciences forestières*. Vol. 42. 2. EDP Sciences. 1985, pp. 193–200.

[36] C. Grossiord et al. "Plant responses to rising vapor pressure deficit". In: *New Phytologist* 226.6 (2020), pp. 1550–1566.

[37] S.K. Gulev et al. "Changing State of the Climate System". In: *Climate Change 2021: The Physical Science Basis. Contribution of Working Group I to the Sixth Assessment Report of the Intergovernmental Panel on Climate Change*. Ed. by V. Masson-Delmotte et al. Cambridge, United Kingdom and New York, NY, USA: Cambridge University Press, 2021. Chap. 2, pp. 287–422. DOI: https://doi.org/10.1017/9781009157896.004.

[38] J. L. Harrison et al. "Transpiration of Dominant Tree Species Varies in Response to Projected Changes in Climate: Implications for Composition and Water Balance of Temperate Forest Ecosystems". In: *Ecosystems* (2020), pp. 1–16.

[39] S. K. Hassler, M. Weiler, and T. Blume. "Tree-, stand- and site-specific controls on landscape-scale patterns of transpiration". In: *Hydrology and Earth System Sciences* 22.1 (2018), pp. 13–30. DOI: 10.5194/hess-22-13-2018.

[40] M. D. Hoffman and A. Gelman. “The No-U-Turn sampler: adaptively setting path lengths in Hamiltonian Monte Carlo.” In: *Journal of Machine Learning Research* 15.1 (2014), pp. 1593–1623.

[41] P. G. Holland and D. G. Steyn. “Vegetational Responses to Latitudinal Variations in Slope Angle and Aspect”. In: *Journal of Biogeography* 2.3 (1975), pp. 179–183.

[42] Dynamax Inc. *FLGS-TDP Manual*. Houston, TX 77099 USA: Dynamax Inc, 2007.

[43] ICT International. *Heat Ratio Method (HRM) Installation Operation Manual, version 1.0*. Armidale NSW 2350 AUSTRALIA: ICT International Pty Ltd.

[44] P. G. Jarvis. “The Interpretation of the Variations in Leaf Water Potential and Stomatal Conductance Found in Canopies in the Field”. In: *Philosophical Transactions of the Royal Society of London. Series B, Biological Sciences* 273.927 (1976), pp. 593–610. ISSN: 00804622. URL: http://www.jstor.org/stable/2417554.

[45] S. Jasechko et al. “Terrestrial water fluxes dominated by transpiration”. In: *Nature* 496.7445 (2013), pp. 347–350.

[46] Charles D. Keeling. “The Concentration and Isotopic Abundances of Carbon Dioxide in the Atmosphere”. In: *Tellus* 12.2 (1960), pp. 200–203. DOI: https://doi.org/10.1111/j.2153-3490.1960.tb01300.x. URL: https://onlinelibrary.wiley.com/doi/abs/10.1111/j.2153-3490.1960.tb01300.x.

[47] Gyung-Tae Kim et al. “hotomorphogenesis of leaves: shade-avoidance and differentiation of sun and shade leaves”. In: *Photochemical Photobiological Sciences* 4.9 (2005), pp. 770–774. DOI: 10.1039/b418440h. URL: https://doi.org/10.1039/b418440h.

[48] Miko U. F. Kirschbaum. “Direct and indirect climate change effects on photosynthesis and transpiration.” In: *Plant biology* 6 3 (2004), pp. 242–53.

[49] A.K. Knapp and W.K. Smith. “Stomatal and photosynthetic responses during sun/shade transitions in subalpine plants: influence on water use efficiency”. In: *Oecologia* 74.1 (1987), pp. 62–67.

[50] Alan K Knapp and William K Smith. “Stomatal and photosynthetic responses to variable sunlight”. In: *Physiologia Plantarum* 78.1 (1990), pp. 160–165.

[51] Tomo’omi Kumagai et al. “Sap flow estimates of stand transpiration at two slope positions in a Japanese cedar forest watershed”. In: *Tree Physiology* 27.2 (Feb. 2007), pp. 161–168.

[52] W. Larcher. *Physiological Plant Ecology, 3rd edition*. 1995.

[53] Jun-Hak Lee, Gregory S. Biging, and Joshua B. Fisher. “An Individual Tree-Based Automated Registration of Aerial Images to LiDAR Data in a Forested Area”. In: *Photogrammetric Engineering & Remote Sensing* 82.9 (2016), pp. 699–710. ISSN: 0099-1112. DOI: `doi:10.14358/PERS.82.9.699`. URL: `https://www.ingentaconnect.com/content/asprs/pers/2016/00000082/00000009/art00017`.

[54] Léo Lemordant et al. “Critical impact of vegetation physiology on the continental hydrologic cycle in response to increasing CO₂”. In: *Proceedings of the National Academy of Sciences* 115.16 (2018). DOI: `10.1073/pnas.1720712115`. URL: `https://www.pnas.org/doi/abs/10.1073/pnas.1720712115`.

[55] P. Link et al. “Species differences in the seasonality of evergreen tree transpiration in a Mediterranean climate: Analysis of multiyear, half-hourly sap flow observations”. In: *Water Resources Research* 50.3 (2014), pp. 1869–1894.

[56] P. A. Link. “Forests, Water, and the Atmosphere in Northern California: Insights from Sap-Flow Data Analysis and Numerical Atmospheric Model Simulations”. PhD thesis. UC Berkeley, 2015.

[57] T. Lohammar et al. “FAST: Simulation Models of Gaseous Exchange in Scots Pine”. In: *Ecological Bulletins* 32 (1980), pp. 505–523. ISSN: 03466868. URL: `http://www.jstor.org/stable/20112831`.

[58] Xiangzhong Luo and Trevor F. Keenan. “Global evidence for the acclimation of ecosystem photosynthesis to light”. In: *Nature Ecology Evolution* 4.10 (2020), pp. 1351–1357. DOI: 10.1038/s41559-020-1258-7. URL: https://doi.org/10.1038/s41559-020-1258-7.

[59] Yadvinder Malhi et al. “Tropical Forests in the Anthropocene”. In: *Annual Review of Environment and Resources* 39.1 (2014), pp. 125–159. DOI: 10.1146/annurev-environ-030713-155141. URL: https://doi.org/10.1146/annurev-environ-030713-155141.

[60] D. C. Marshall. “Measurement of Sap Flow in Conifers by Heat Transport. 1”. In: *Plant Physiology* 33.6 (Nov. 1958), pp. 385–396. ISSN: 0032-0889. DOI: 10.1104/pp.33.6.385. URL: https://doi.org/10.1104/pp.33.6.385.

[61] Nate McDowell et al. “Mechanisms of plant survival and mortality during drought: why do some plants survive while others succumb to drought?” In: *New Phytologist* 178.4 (2008), pp. 719–739. DOI: https://doi.org/10.1111/j.1469-8137.2008.02436.x. URL: https://nph.onlinelibrary.wiley.com/doi/abs/10.1111/j.1469-8137.2008.02436.x.

[62] BELINDA E. MEDLYN et al. “Reconciling the optimal and empirical approaches to modelling stomatal conductance”. In: *Global Change Biology* 17.6 (2011), pp. 2134–2144. DOI: https://doi.org/10.1111/j.1365-2486.2010.02375.x.

[63] M. Mencuccini, S. Manzoni, and B. Christoffersen. “Modelling water fluxes in plants: from tissues to biosphere”. In: *New Phytologist* 222.3 (2019), pp. 1207–1222.

[64] Daniel Metzen et al. “Spatio-temporal transpiration patterns reflect vegetation structure in complex upland terrain”. In: *Science of The Total Environment* 694 (2019). DOI: https://doi.org/10.1016/j.scitotenv.2019.07.357.

[65] Mirco Migliavacca et al. “The three major axes of terrestrial ecosystem function”. In: *Nature* 598.7881 (2021), pp. 468–472. DOI: 10.1038/s41586-021-03939-9. URL: https://doi.org/10.1038/s41586-021-03939-9.

[66] Kenneth E. Mitchell et al. “The multi-institution North American Land Data Assimilation System (NLDAS): Utilizing multiple GCIP products and partners in a continental distributed hydrological modeling system”. In: *Journal of Geophysical Research: Atmospheres* 109.D7 (2004). DOI: `https://doi.org/10.1029/2003JD003823`.

[67] X. Morin et al. “Long-term response of forest productivity to climate change is mostly driven by change in tree species composition”. In: *Scientific Reports* 8.4 (2018), pp. 3269–3340. DOI: `10.1038/s41598-018-23763-y`. URL: `https://doi.org/10.1038/s41598-018-23763-y`.

[68] J. Oshun. “The isotopic evolution of a raindrop through the critical zone”. PhD thesis. UC Berkeley, 2016.

[69] J. Oshun et al. “Dynamic, structured heterogeneity of water isotopes inside hillslopes”. In: *Water Resources Research* 52.1 (2016), pp. 164–189.

[70] Christoforos Pappas, Simone Fatichi, and Paolo Burlando. “Modeling terrestrial carbon and water dynamics across climatic gradients: does plant trait diversity matter?” In: *New Phytologist* 209.1 (2016), pp. 137–151. DOI: `https://doi.org/10.1111/nph.13590`.

[71] C. Parmesan et al. “Terrestrial and Freshwater Ecosystems and their Services.” In: *Climate Change 2022: Impacts, Adaptation, and Vulnerability. Contribution of Working Group II to the Sixth Assessment Report of the Intergovernmental Panel on Climate Change*. Ed. by H.-O. Pörtner et al. Cambridge, United Kingdom and New York, NY, USA: Cambridge University Press, 2022. Chap. 2, In Press.

[72] R. W. Pearcy. “Acclimation to Sun and Shade”. In: *Photosynthesis: A Comprehensive Treatise*. Ed. by Agepati S. Raghavendra. Cambridge: Cambridge University Press, 1998. Chap. 19, pp. 250–263.

[73] Markus Reichstein et al. “Linking plant and ecosystem functional biogeography”. In: *Proceedings of the National Academy of Sciences* 111.38 (2014), pp. 13697–13702. DOI: `10.1073/pnas.1216065111`. URL: `https://www.pnas.org/doi/abs/10.1073/pnas.1216065111`.

[74] D. M. Rempe and W. E. Dietrich. "Direct observations of rock moisture, a hidden component of the hydrologic cycle". In: *Proceedings of the National Academy of Sciences* 115.11 (2018), pp. 2664–2669.

[75] Daniella M. Rempe and William E. Dietrich. "A bottom-up control on fresh-bedrock topography under landscapes". In: *Proceedings of the National Academy of Sciences* 111.18 (2014), pp. 6576–6581. DOI: `10.1073/pnas.1404763111`. URL: `https://www.pnas.org/doi/abs/10.1073/pnas.1404763111`.

[76] M. Renner et al. "Dominant controls of transpiration along a hillslope transect inferred from ecohydrological measurements and thermodynamic limits". In: *Hydrology and Earth System Sciences* 20.5 (2016), pp. 2063–2083. DOI: `10.5194/hess-20-2063-2016`.

[77] P. Romero-Lankao et al. "North America". In: *Climate Change 2014: Impacts, Adaptation, and Vulnerability. Part B: Regional Aspects.* Ed. by V.R. Barros et al. Cambridge, United Kingdom and New York, NY, USA: Cambridge University Press, 2014. Chap. 26, pp. 1439–1498.

[78] J. Salvatier, T. V. Wiecki, and C. Fonnesbeck. "Probabilistic programming in Python using PyMC3". In: *PeerJ Computer Science* 2 (2016), e55.

[79] A. F. W. Schimper. *Plant-geography upon a physiological basis.* Ed. by P. Groom and I. B. Balfour. Trans. by W. R. Fisher. Oxford, United Kingdom: Oxford Clarendon Press, 1903.

[80] William H. Schlesinger and Scott Jasechko. "Transpiration in the global water cycle". In: *Agricultural and Forest Meteorology* 189-190 (2014), pp. 115–117. ISSN: 0168-1923. DOI: `https://doi.org/10.1016/j.agrformet.2014.01.011`. URL: `https://www.sciencedirect.com/science/article/pii/S0168192314000203`.

[81] B. Stafford. *pysolar*. Version 0.8. Sept. 2018. DOI: `10.5281/zenodo.1461066`. URL: `https://doi.org/10.5281/zenodo.1461066`.

[82] V. J Stokes, M. D. Morecroft, and J. I.L. Morison. "Comparison of leaf water use efficiency of oak and sycamore in the canopy over two growing seasons". In: *Trees* 24.2 (2010), pp. 297–306.

[83] Huizhen Sun, Doug Aubrey, and Robert Teskey. “A simple calibration improved the accuracy of the thermal dissipation technique for sap flow measurements in juvenile trees of six species”. In: *Trees* 26 (Apr. 2011). DOI: 10.1007/s00468-011-0631-1.

[84] KENNETH V. THIMANN. “Chapter I - Phototropism”. In: *Photobiology, Ionizing Radiations*. Ed. by MARCEL FLORKIN and ELMER H. STOTZ. Vol. 27. Comprehensive Biochemistry. Elsevier, 1967, pp. 1–29. DOI: https://doi.org/10.1016/B978-1-4831-9716-6.50009-4. URL: https://www.sciencedirect.com/science/article/pii/B9781483197166500094.

[85] G. C. Topp, J. L. Davis, and A. P. Annan. “Electromagnetic determination of soil water content: Measurements in coaxial transmission lines”. In: *Water Resources Research* 16.3 (1980), pp. 574–582. DOI: https://doi.org/10.1029/WR016i003p00574. URL: https://agupubs.onlinelibrary.wiley.com/doi/abs/10.1029/WR016i003p00574.

[86] USDA. *CALVEG zones and alliances: vegetation descriptions*. Tech. rep. 2008. URL: http://www.fs.usda.gov/Internet/FSE_DOCUMENTS/fsbdev3_046448.pdf.

[87] M. D. Vrettas and I. Y. Fung. “Sensitivity of transpiration to subsurface properties: Exploration with a 1-D model”. In: *Journal of Advances in Modeling Earth Systems* 9.2 (2017), pp. 1030–1045.

[88] Y. Wang et al. “A theoretical and empirical assessment of stomatal optimization modeling”. In: *New Phytologist* (2020).

[89] Eric J Ward et al. “TRACC: an open source software for processing sap flux data from thermal dissipation probes”. In: *Trees* 31.5 (2017), pp. 1737–1742.

[90] R. H. Waring and J. J. Landsberg. “Generalizing plant–water relations to landscapes”. In: *Journal of Plant Ecology* 4.1-2 (Mar. 2011), pp. 101–113. ISSN: 1752-9921. DOI: 10.1093/jpe/rtq041. eprint: https://academic.oup.com/jpe/article-pdf/4/1-2/101/2772464/rtq041.pdf. URL: https://doi.org/10.1093/jpe/rtq041.

[91] D.R. Young and W.K. Smith. "Influence of sunflecks on the temperature and water relations of two subalpine understory congeners". In: *Oecologia* 43.2 (1979), pp. 195–205.

[92] Derek J. N. Young et al. "Long-term climate and competition explain forest mortality patterns under extreme drought". In: *Ecology Letters* 20.1 (2017), pp. 78–86. DOI: `https://doi.org/10.1111/ele.12711`.

[93] C. Zamuda et al. *US energy sector vulnerabilities to climate change and extreme weather*. Tech. rep. Washington DC: Department of Energy, 2013.

[94] Q. Zhang et al. "The hysteretic evapotranspiration—Vapor pressure deficit relation". In: *Journal of Geophysical Research: Biogeosciences* 119.2 (2014), pp. 125–140. DOI: `10.1002/2013JG002484`. eprint: `https://agupubs.onlinelibrary.wiley.com/doi/pdf/10.1002/2013JG002484`. URL: `https://agupubs.onlinelibrary.wiley.com/doi/abs/10.1002/2013JG002484`.